Summer 7-1-2018

Sonomechanical Enhanced Sparging Techniques for Advanced Reactor Applications

Floren V. Rubio
University of New Mexico

Floren Rubio

Candidate

Nuclear Engineering

Department

This dissertation is approved, and it is acceptable in quality and form for publication:

Approved by the Dissertation Committee:

Dr. Anil Prinja , Chairperson

Dr. Edward Blandford

Dr. Leonard Bond

Dr. Sang Han

Dr. Youho Lee

Sonomechanical Enhanced Sparging Techniques for Advanced Reactor Applications

by

Floren Valderrama Rubio

B.S. Nuclear Engineering, University of California, Berkeley, 2011
A.S., Napa Valley College, 2009

DISSERTATION

Submitted in Partial Fulfillment of the
Requirements for the Degree of

Doctor of Philosophy
Engineering

The University of New Mexico

Albuquerque, New Mexico

July, 2018

Dedication

To my late father, Elpidio Rubio, and my mother Conchita Rubio for your support and encouragement; and to my girlfriend Lurline Oritz for standing by me two states away for all this time.

"I'm delirious with joy. It proves that if you confront the universe with good intentions in your heart, it will reflect that and reward your intent. Usually. It just doesn't always do it in the way you expect." – J. Michael Straczynski

Acknowledgments

First and foremost, I would like to thank my advisor Dr. Edward Blandford for his guidance and motivation. He has taught me to see the world differently, and allowed me to see possibilities that I would not have been able to see myself.

Next, I would like to acknowledge my research cohort over these years. Amy Drumm, Bryan Wallace, Nico Milonopolous, Seung-Jun Kim, Amir Ali, Maolong Liu, and Joel Hughes have all supported me through my time at UNM. In addition, I would also like to acknowledge the undergrads Cole Mueller and Gemma Irais "Ira" Strong. They both were indispensable in the lab and have performed above and beyond with any task I have given them. It was my pleasure to mentor them as best I could while they were working for me.

I would like to acknowledge the friends that I have made here at UNM. I have had the pleasure of having Vanessa Goss and Greg Ottino as best neighbors I have had. Bobbi Reidel for allowing me to help mentor her through undergrad. Maolong Liu for being a great friend and work colleague, and helping me with my trip to China. In particular, I would like to thank Joel Hughes. He was the longest office mate I have ever had, and one of my best friends I have made out here. They all have seen me through some pretty tough times, and I am glad they were all there for me.

I would lastly like to thank my Mother, Conchita Rubio, and late Father, Elpidio Rubio. Without their guidance and support I would not who I am today. Finally, my girlfriend, Lurline Ortiz, who has given me unconditional support and love.

Sonomechanical Enhanced Sparging Techniques for Advanced Reactor Applications

by

Floren Valderrama Rubio

B.S. Nuclear Engineering, University of California, Berkeley, 2011
A.S., Napa Valley College, 2009

Doctor of Philosophy
Engineering, University of New Mexico, 2018

Abstract

The fluoride salt cooled high temperature reactor (FHR) is a Generation IV advanced reactor design that has potential to produce efficient, low carbon, and safe energy. But, there are significant engineering challenges that need to be addressed before the deployment of this reactor. One of the key challenges is tritium release mitigation and sequestration. Because the FHR utilizes a eutectic LiF-BeF_2 (flibe) salt as a coolant, the coolant is a significant source of tritium.

High-power ultrasonics have been used in many industrial process streams such as food processing, metal production, chemical production, and pharmaceutical manufacturing. Techniques and concepts from these applications were used in designing the mass transfer experiments. This dissertation supports the effort to address the tritium challenge by investigating inert gas sparging coupled with high-power ultra-

sonics through two scaled mass transfer experiments and a parameter comparison study of the two experiments.

The first experiment reported in this dissertation is the Small Ultrasonic Mass Transfer Experiment (SUMATRA). This experiment had shown proof-of-concept that high power ultrasonics can enhance sparging mass transfer. The second experiment, the Prototype Ultrasonic Mass Transfer (PULST) experiment, was an attempt to scale-up the SUMATRA experiment and to construct a prototype ultrasonically enhanced sparging mass transfer module which was designed based on utilizing commercial-off-the-shelf components. Although the PULST experimental data did not conclusively show an enhancement in the mass transfer rate, a parameter comparison was performed to define the boundaries of the design space in order to provide insight in designing a more optimized mass transfer sparging cell. The implications of the two experiments and parameter study are discussed and suggestions for future work is presented.

Contents

List of Figures

List of Tables

Nomenclature

Greek symbols

α	Thermal diffusion rate (m^2/s)
δ	Boundary layer thickness (m)
ϵ	Turbulence dissipation rate (m^2/s^3)
η	Sheer viscosity (mPa/s)
κ	Polytropic constant $*$
λ	Wavelength (m)
μ	Dynamic viscosity $(mPa\ s)$
ν	Kinematic viscosity $(m^2\ s)$
ω	Period (s)
σ	Surface tension (N/m)
τ	Residence time (s)
ε	holdup $*$

ϱ	Total dampening coefficient $(*)$

Non-dimensional numbers

$Pr = \frac{\nu}{\alpha}$	Prandtl number
$Re = \frac{\rho u L}{\mu}$	Reynolds number
Re_b	Bubble Reynolds
$Sc = \frac{\mu}{\rho \mathscr{D}}$	Schmidt number
$Sh = \frac{k_L \ L}{\mathscr{D}}$	Sherwood number
$We = \frac{\rho \ U^2 \ L}{\sigma}$	Weber number

Roman symbols

$\mathscr{D}$	Diffusivity (m^2/s)
a	Interfacial area (m^2/m^3)
C	Concentration
c	Speed of sound (m/s)
C_d	Drag coefficient
C_m	Glycerol concentration $(wt\%)$
d	Diameter (m)
$dB(SPL)$	Decibel sound power level $*$
DO	Dissolved oxygen (mg/L)
f	Frequency (Hz)

F_d	Drag force
g	Gravitational constant (m/s)
I	Acoustic intensity (W/m^2)
K	Flow consistency index $(Pa\ s^n)$
K_H	Henry's constant
k_L	Mass transfer coefficient (m/s)
k_La	Volumetric mass transfer coefficient $(1/s)$
L	Length (m) or (in)
p	Pressure (Pa)
R	Bubble radius (m)
r	Bubble absorption rate
R_P	Reflection coefficient $*$
S	Renewal frequency $(1/s)$
T	Temperature (C)
t_e	Time exposure (s)
T_P	Transmission coefficient $*$
U	Fluid velocity (m/s)
V	Volume (m^3) or (gal)
Z	Acoustic impedance $(Rayl)$ or $(Pa\ s/m^2)$

Superscripts

$*$	dimensionless

Other subscripts

L	Length m or in

Chapter 1

Introduction

Nuclear energy has been a source of safe and low carbon energy source [1, 2]. Currently in the United States, the fleet of nuclear reactors is aging with out any scheduled replacement for base load power. One solution would be to replace this aging fleet of light water reactors (LWR) with safer and more efficient Generation IV reactors. The Generation IV International Forum (GIF) is an international cooperative research endeavor to carry out research on the feasibility and performance capabilities of the next generation of nuclear reactors [3]. These designs are focused on utilizing the advances in sustainability, economics, safety, reliability, and proliferations resistance [4]. One design under consideration is the fluoride salt high temperature reactor (FHR). The FHR design has some major engineering challenges before it can be made safe and economically viable. One of these challenges is the production and environmental release of tritium. This dissertation will discuss the history of the FHR technology and the technology development process to address the tritium challenge for the FHR.

1.1 History of the FHR

The FHR program has its roots in the nuclear aviation program. This was the first (and only) attempt to power an airplane using nuclear power. This project produced the Aircraft Reactor Experiment (ARE) which employed a molten salt to attain the designed temperatures and power density required for flight. The ARE used a fluoride salt as the fuel salt, specifically NaF/ZrF_4 with dissolved UF_4, and it was moderated by BeO blocks, as shown in Figure 1.1. Reactivity of the reactor was controlled by a combination of control rods and variable fuel concentration (salt enrichment) [5, 6].

The ARE was taken to initial criticality at Oak Ridge National Lab (ORNL) in 1954 [6]. It ran for its designed 100 *MW-hrs* [7]. In doing so, it proved the viability of the molten fuel concept as well and provided a wealth of knowledge on molten salt technology, chemistry, and materials [5].

The program was abandoned in 1961 because it did not convince the administration, at the time, that it was viable as an aircraft engine. Later, in 1960's, the technology was investigated for civilian power generation with the Molten Salt Reactor Experiment (MSRE) at ORNL until the mid 1970's. The molten salt design had demonstrated advantages over the LWR counterpart. A few of these advantages are lower operating pressure, no cladding concerns, no melt down concerns, less prominent xenon poisoning transient, no steam explosions, and good fission product solubility [8]. The MSRE program was soon shutdown three years later in 1973 however, much of the operational knowledge of operating the reactor and flibe have been documented in a series of ORNL reports from these two projects. The MSRE was operated from 1965 (initial criticality) to 1969 where it provided confidence in performance and the practicality of molten salt systems [5]. The molten salt program was fully shutdown in 1976.

Generation IV International Forum had identified MSR's as an advanced reactor design of interest, and this attracted some attention from the nuclear community [9]. This restarted the efforts of the nuclear community to continue research in salt-cooled reactors. The MSR design has been considered as an option for a Generation IV reactor because of its intrinsic safety features which are the large negative temperature coefficient of reactivity, possibility of continuous fission product removal (He sparging or pyrochemical processes), ability to achieve high burnup, and avoidance of fuel fabrication and transport expenses [10]. Branching off of the dissolved fuel

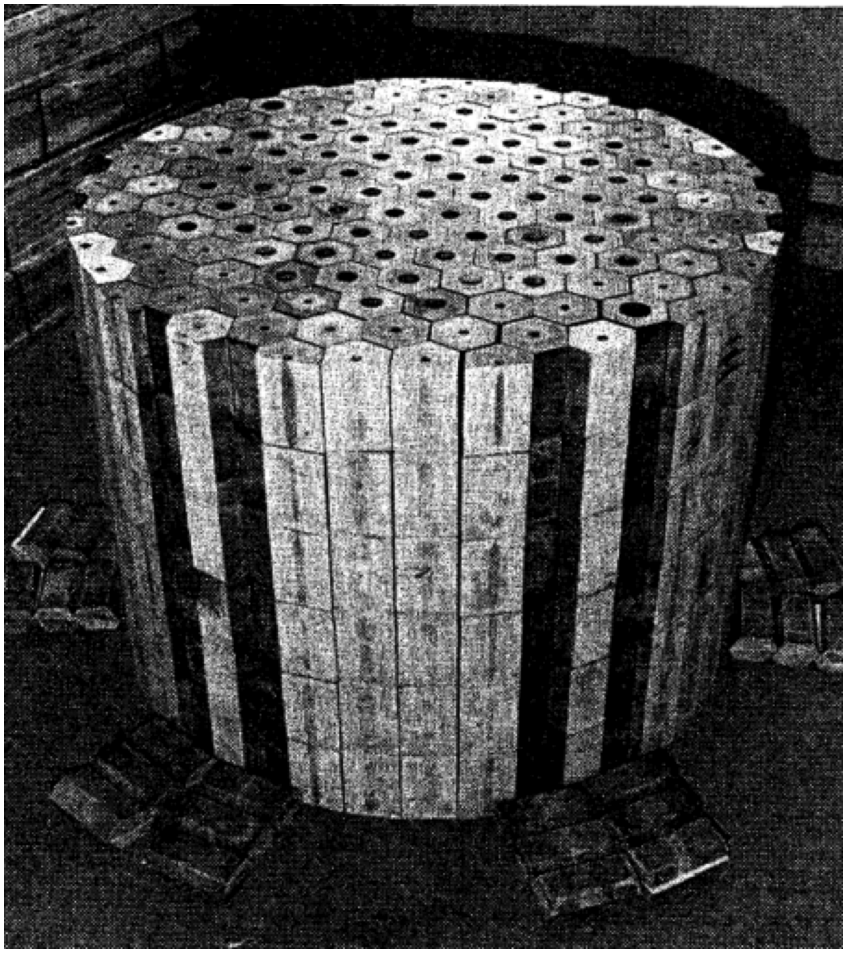

Figure 1.1: *BeO* moderator blocks for the ARE [6]

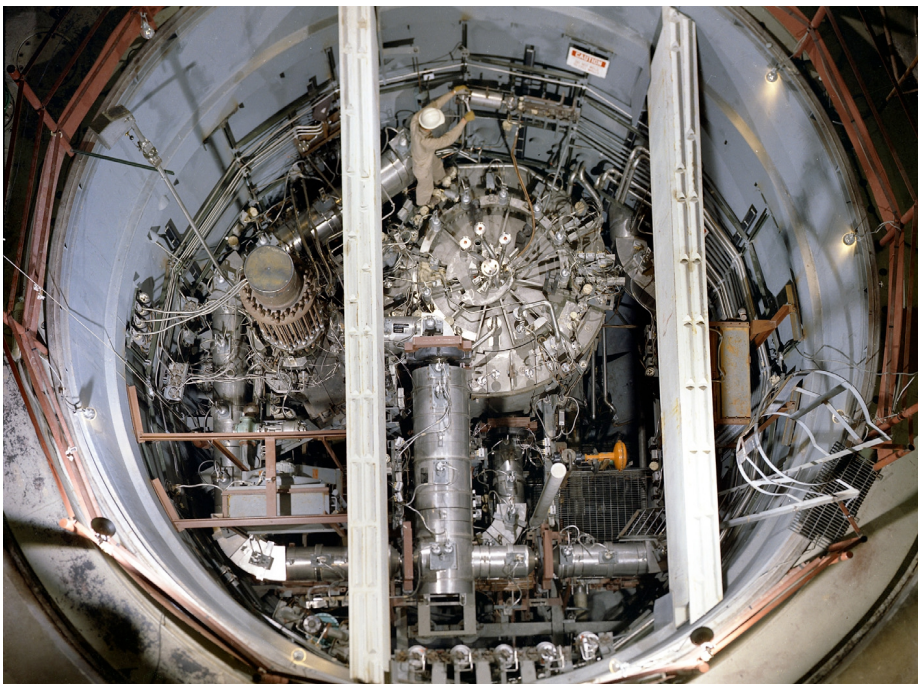

Figure 1.2: Top view of the MSRE core, fuel pump, and heat exchanger in the primary system containment tank. (ORNL Photo 67051-64)

molten salt concept, the FHR designs have been considered due of this new interest. The features of this advanced design are passive safety, higher temperatures, and proliferation resistance. The key contrast between the MSR and FHR designs is the FHR utilized as solid fuel form instead of the dissolved fuel form. The considered fuel forms are plates [11], pins [12], and graphite pebbles [13].

The overarching goal of the FHR is to combine four technologies to provide an economically competitive and passively safe reactor. These technologies are illustrated in Figure 1.3. Although there are other FHR design concepts, this dissertation will focus on the reference Mk-1 PB-FHR design from UC Berkeley [13]. The coolant of choice is flibe, and as described earlier, this allows for high temperature operations with low vapor pressure and is relatively chemically inert. The pool type design allows for passive safety strategies. The reactor core is an annular config-

uration with a bed of graphite pebbles which is designed to accommodate on-line pebble removal and insertion [13]. The graphite pebbles are seeded with a Tristructural Isotropic (TRISO) fuel particle provides a good initial fission product barrier to release. These particles have been shown to retain fission products under accident conditions of $1600°C$ [14]. The final technology implemented for this design is the air-Brayton cycle in order to utilize higher efficiencies than the currently used Rankine cycles [13].

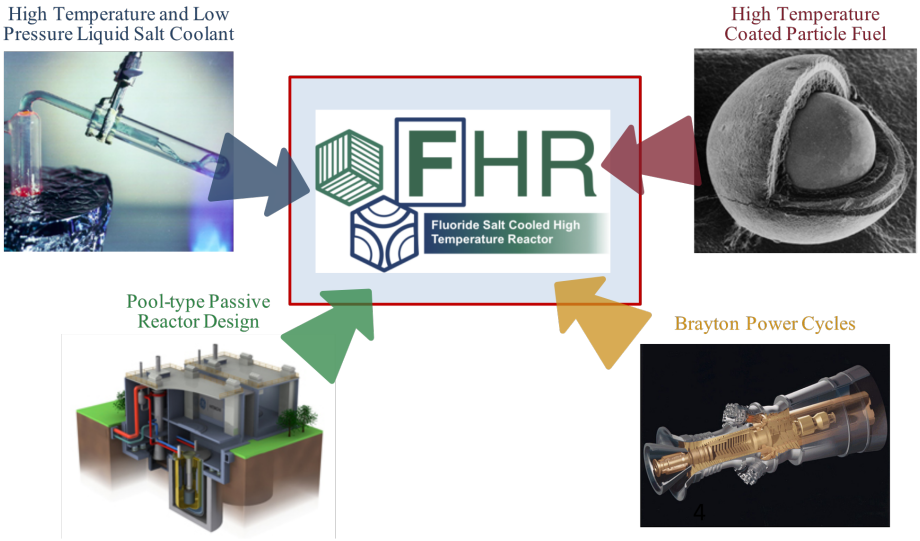

Figure 1.3: Four defining characteristics of the PB-FHR

1.2 Overview of Current FHR Technologies

Due to the recent interest in developing FHR technology, two integrated research projects (IRP) were funded by the DOE. The two IRP's were head by MIT and Ohio State and charged with investigating FHR technology and licensing challenges. The challenges include material compatibility, flibe handling, thermo-hydraulic performance, neutronics, and tritium release mitigation.

The notional diagram of the FHR is shown in Figure 1.4. The primary circuit consists of the annular core, pump, and salt-to-salt intermediate heat exchanger (IHX). During normal operations, the reactor pump will circulate coolant salt as shown by the blue arrows. The secondary loop consists of the IHX, pump and a secondary salt-to-gas heat exchanger. During an emergency on the secondary side where core cooling is compromised, there is a direct auxiliary cooling system (DRACS) which will begin to operate passively by natural convection. The DRACS operates passively with the use of a fluidic diode. During normal operation, the fluidic diode has a very high flow resistance, minimizing parasidic heat loses. During an accident conditions, flow will reverse through the DRACS system due to natural convection providing passive decay heat removal.

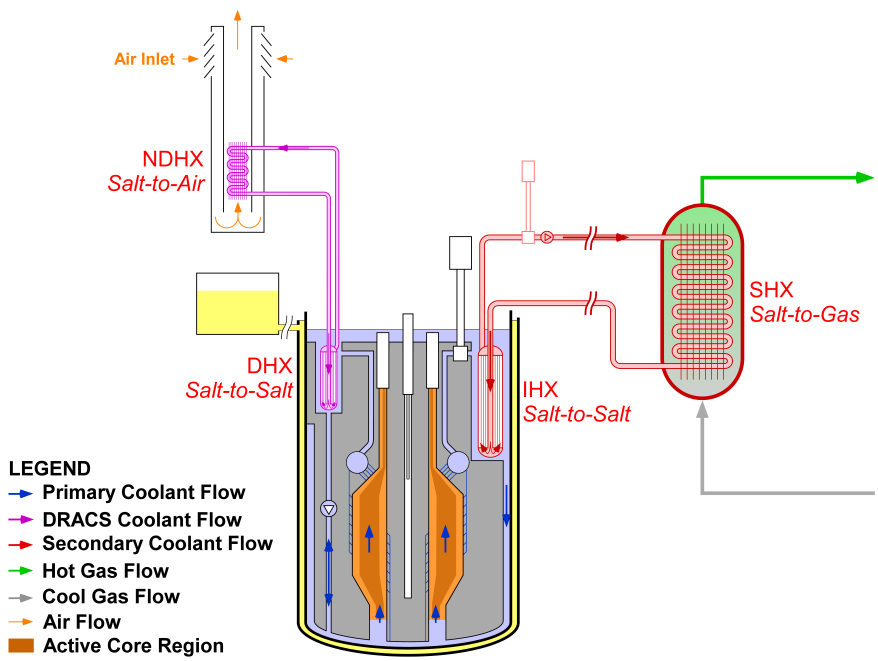

Figure 1.4: Notional FHR primary coolant circuit.

The Mk-1 design is a 236 $MWth$ small modular reactor pebble bed reactor. This

design utilized a nuclear air Brayton combined cycle (NACC) based on the General Electric 7FB gas turbine for power conversion. The notional power plant layout is shown in Figure 1.5.

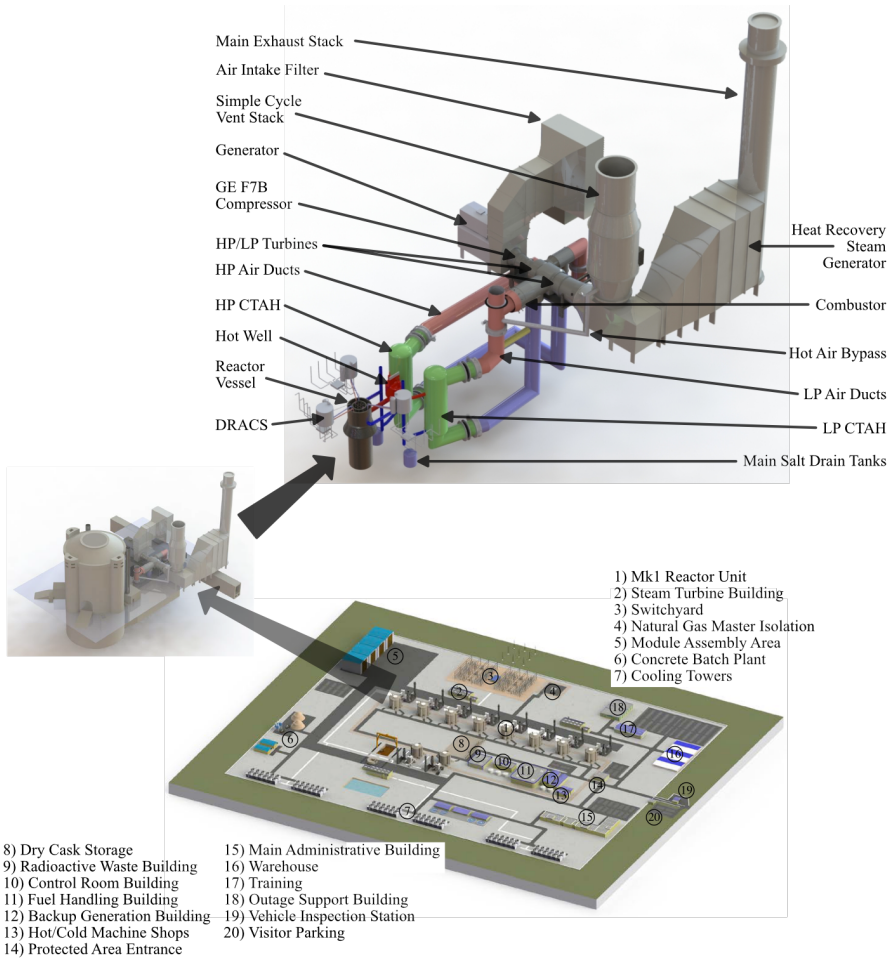

Figure 1.5: Mk-1 Pb-FHR power plant layout, reproduced from ref [13]

A key challenge in approaching this design is the thermodynamic behavior and the material compatibility of the coolant salt. Much of this operational knowledge has been lost since the MSRE/MSBR projects, so the FHR community must re-gain this lost knowledge. This has been done incrementally by focusing on separate effects tests, followed by integrated effects tests [15, 16] and by investigating and

characterizing the flibe coolant itself.

1.3 Tritium Concern in the FHR

Of all the possible candidate salts, flibe was chosen for the FHR for its relatively high thermal conductivity and favorable neutronic performance [17]. However, in a neutron flux, flibe is a significant source of tritium through three production pathways. Two direct pathways are described in equations (1.1) and (1.2); and there is an indirect path through equation (1.3) to equation (1.1) through the production of ${}^{6}_{3}Li$.

$$ {}^{6}_{3}Li + {}^{1}_{0}n \rightarrow {}^{4}_{2}He + {}^{3}_{1}H \tag{1.1} $$

$$ {}^{7}_{3}Li + {}^{1}_{0}n \rightarrow {}^{4}_{2}He + {}^{1}_{0}n + {}^{3}_{1}H \tag{1.2} $$

$$ \begin{aligned} {}^{9}_{4}Be + {}^{1}_{0}n &\rightarrow {}^{4}_{2}He + {}^{6}_{2}He \\ {}^{6}_{2}He &\rightarrow {}^{6}_{3}Li + \beta^{-} + \gamma \end{aligned} \tag{1.3} $$

This results in a much larger projected tritium release from the FHR in comparison to current pressurized water reactors (PWRs). The average PWR can produce 1.99 Ci/day [18], and the FHR would produce 2508 Ci/day [12]. Because tritium behaves very similarly to hydrogen, with respect to material diffusion, this would make a means of tritium sequestration, separation, and capture to prevent environmental tritium release a necessity. As shown in Figure 1.6, tritium escape points are highlighted. These regions are salt-to-gas heat exchangers in the DRACS and the heat

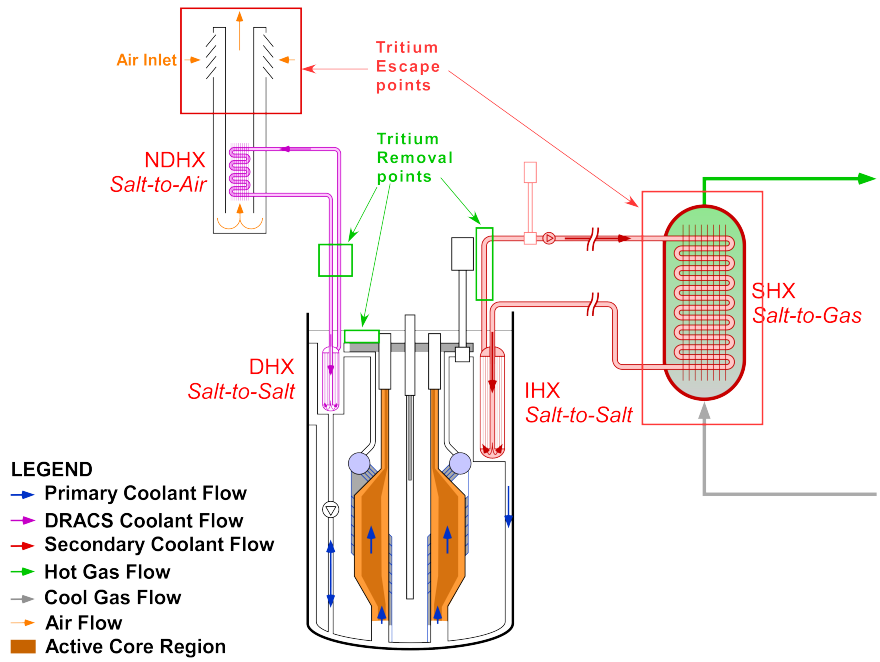

Figure 1.6: Diagram of an FHR. Highlighted are areas areas where tritium has a high potential of release and areas where a tritium removal system can be most beneficial.

exchangers because the thin walled tubes of heat exchangers which provide a path for diffusion of tritium across at high temperatures. Strategies that are currently being investigated investigated include graphite adsorption [19], mass permeators [19], barrier coatings [19], and inert gas sparging [19, 20]. Each strategy has its own set of advantages and disadvantages, but inert gas sparging has the unique potential to not only removing and sequestering tritium through a process stream, but enhance the process through the utilization of high powered ultrasonics.

1.4 Ultrasonic Technologies

Historically, in the nuclear engineering industry, ultrasonics have been dominantly used as a method of non-destructive evaluation and non-destructive testing (NDE/ NDT). These applications are generally in the low power regime. High power ultrasonics have been used in many different industries such as pharmaceutical, chemical production, metal alloy production, textiles, and food production [21, 22, 23, 24]. Given the diversity of the engineering challenges, high power ultrasonics has been used for and some similarities between nuclear and other non nuclear industries and processes, there is potential for the incorporation of high power ultrasonics into the nuclear industry [25, 26].

In this work, high power ultrasonics will be applied to investigate the potential for use in the FHR by enhancing inert gas sparging with ultrasonics. This proposed process is designed to increase the mass transfer rate of fluid degassing by inert gas sparging through mechanical agitation and the increase of interfacial surface area through bubble breakup. The data does show that it is possible with the correct conditions. The contrasting of these conditions does introduce some interesting questions and challenges. This work aims to demonstrate this technology as a viable method for tritium removal and sequestration in the FHR, and just as importantly, a viable tool for other industries to apply to their future challenges.

1.5 Goals and Scope of the Dissertation

The goals of this dissertation are to investigate the use of high powered ultrasonics coupled with inert gas sparging for ultimate deployment in an FHR for tritium removal. In support of this goal, two prototype sonomechanically enhanced sparging mass transfer experiments were performed. Both utilized scaled fluids designed to

match the mass transfer non dimensional numbers for flibe at the operational temperatures of an FHR. Finally, the mass transfer performance was evaluated through model development and validation.

This work implemented an experimental iterative process. An overview of the experimental work and conclusions from this dissertation is illustrated in Figure 1.7. The first of these experiments is documented in Chapter 3. This chapter presents the Small Ultrasonic Mass Transfer (SUMATRA) experiment with the associated informative experiments. The SUMATRA experiment was a benchtop sized mass transfer experiment which required the insight of two exploratory experiments. The SUMATRA experiment showed the proof of concept of sonomechancial enhancement of mass transfer. From this experiment, a Sh correlation was developed using acoustic parameters. A sensitivity analysis of resultant correlations, both ultrasonic and non-ultrasonic, was performed to test the robustness of the correlations.

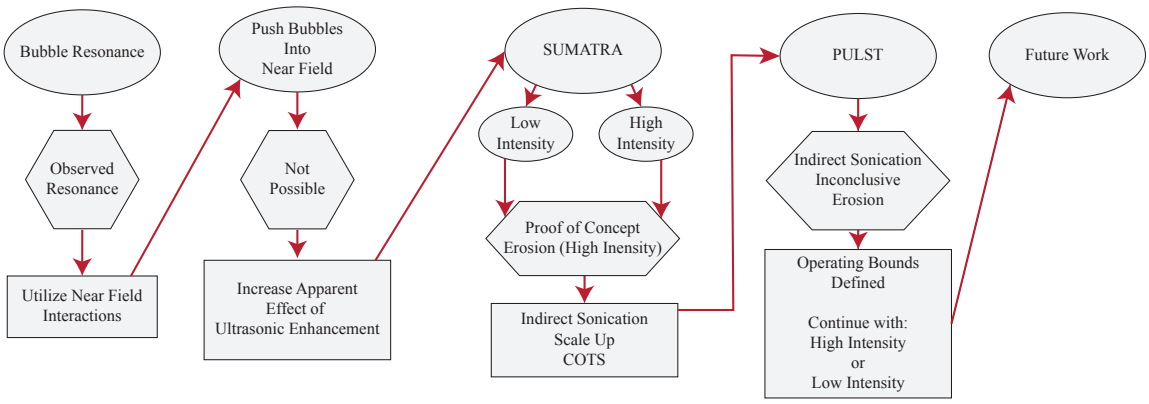

Figure 1.7: Experimental flow path for this dissertation.

Chapter 4 details the Prototype Ultrasonic Mass Transfer (PULST) experiment, which employed insights from the SUMATRA experiment. The PULST experiment attempted to scale up the mass transfer experiment as well as address the horn erosion issue found in the SUMATRA experiment. The results for the mass transfer experiment were not as expected. Despite these results, the operational the data provided important design parameters that can be utilized in a more optimized design.

Chapter 5 compares and contrasts the SUMATRA and PULST experiments. A parameter analysis was performed that compares the experimental data on various parameter spaces in order to successfully identify the reasons the PULST experiment did not show a conclusive result. The result of this analysis provides valuable design parameters, direction, and insights for the construction of an optimized sonomechanical sparging mass transfer cell.

Chapter 2

Theory

This chapter will cover the relevant information for two-phase mass transfer and high power ultrasonics. Fundamental sparging mass transfer and local bubble mass transfer will be summarized. The over view of ultrasonics will be included specifically focusing on sonomechanical effects, cavitation, and acoustic transmission. Finally, background on scaled mass transfer experiments will be discussed.

2.1 Sparging Mass Transfer

Inert gas sparging is the injection of gas into a fluid in order to diffuse dissolved gas into the inert gas bubble, and subsequent removal the inert gas bubble. This section will give an overview of the construction and evolution of two-phase mass transfer models as well as the empirical derivation of mass transfer correlations as it applies to the mechanism of inert gas sparging. In addition, an overview of key mass transfer parameters will be given.

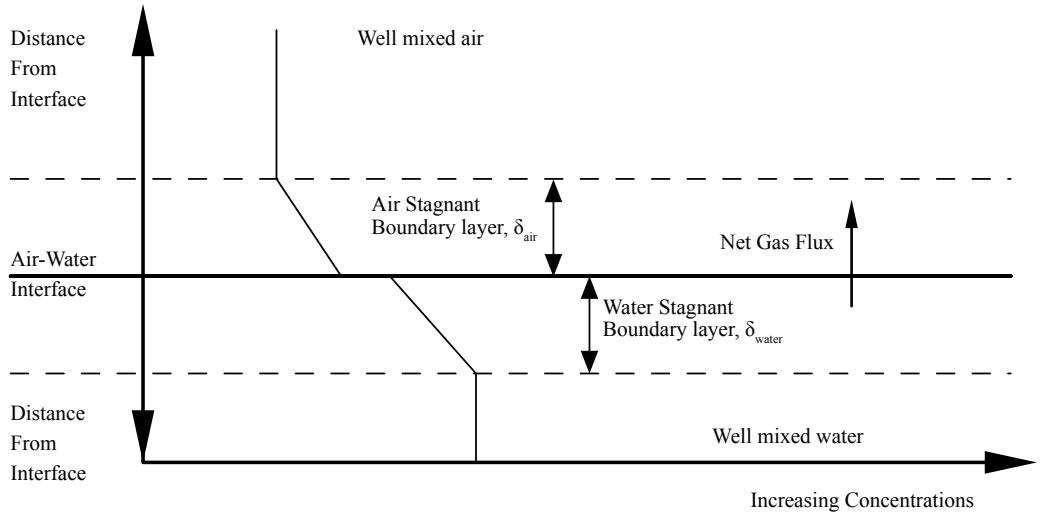

Figure 2.1: Illustration of the two resistance model.

2.1.1 Two Resistance Model

The simplest model of two-phase mass transfer is the Two Resistance Model. This model, as described by Whitman (1923) [27], describes a one dimensional diffusion of species over a fluid/gas interface. Two boundary layers of thickness, δ, at the interface make up two resistance regimes. These boundary layers are stagnant layers of fluid and gas. The fluid outside of the boundary layers, the liquid and gas have uniform species concentration and are considered well mixed. This model is illustrated in 2.1. This shows the diffusion of a species from a liquid (water) to gas (air) illustrated by the species concentration through the regions. From this model of the sum of the two resistances yields the combined resistance coefficient as shown in equation (2.1).

$$\frac{1}{K_L} = \frac{1}{k_L} + \frac{1}{K_H k_A} \tag{2.1}$$

The liquid side mass transfer coefficients are defined for the water side and air side

are defined by equations (2.2) and (2.3).

$$k_L = D_W/\delta_W \tag{2.2}$$

$$k_A = D_A/\delta_A \tag{2.3}$$

This model simply describes an interface between two phases separated by two static resistance layers, one layer of liquid and one layer of gas. Ultimately, what this model overlooks is any variation in the interface such as a turbulence interaction.

2.1.2 Penetration and Surface Renewal Models

The Penetration Model is the evolution of the Two Resistance Model proposed by Higbie in 1935 [28]. This model describes a fluid and gas interface with a fluid boundary layer, similar to the Two Resistance Model. A volume in the bulk fluid would penetrate the boundary layer. The penetration volume will diffuse mass across the interface more quickly than the bulk fluid, but this effect diminishes the longer the penetrating volume remains in the boundary layer, This behavior is described by equation (2.4), where t_e is the time exposure of the penetrating volume at gas/liquid interface and is inversely proportional to the mass transfer coefficient (k_a).

$$k_L = 2\sqrt{\frac{\mathscr{D}_L}{\pi t_e}} \tag{2.4}$$

The Surface Renewal Model, proposed by Danckwerts (1951) [29], is the next logical evolution of the Penetration Model. The model describes the liquid interface as being renewed periodically by the bulk fluid as illustrated in Figure 2.3. The

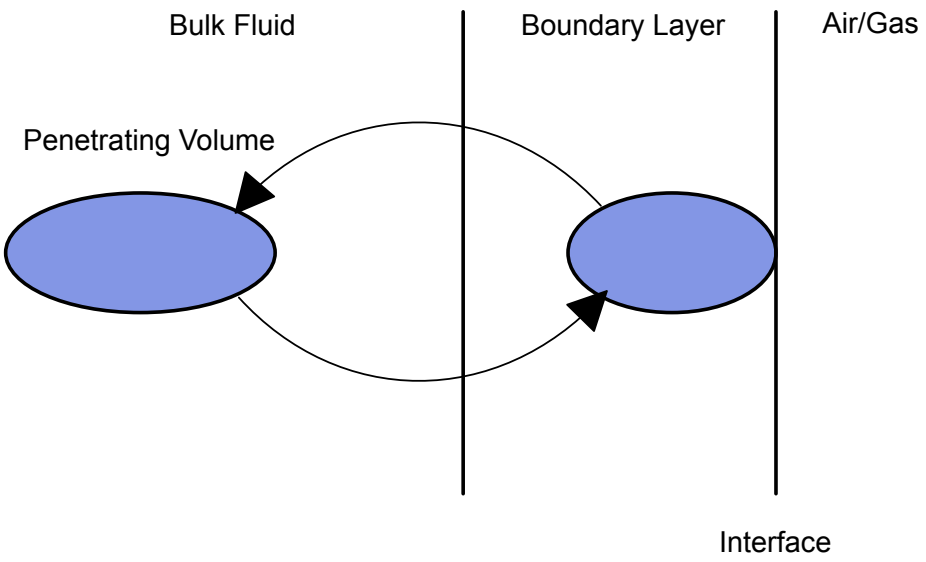

Figure 2.2: Illustration of the Penetration Model.

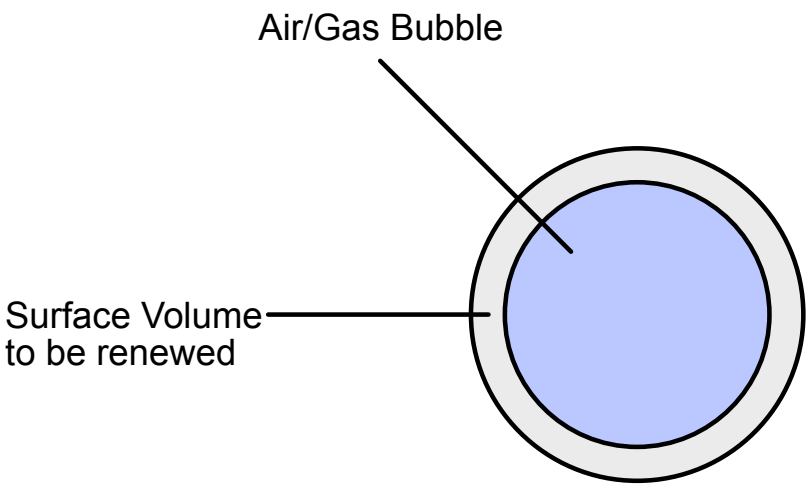

Figure 2.3: Illustration of the Surface Renewal Model.

frequency of the surface volume renewal is proportional to the k_a. This is described by equation (2.5) where the frequency the surface is renewed, S, in units of s^{-1}.

$$k_L = \sqrt{\mathscr{D}_{AB} S} \tag{2.5}$$

2.1.3 Turbulence Interaction Model

This model was developed at ORNL by Kress (1972) [20]. It is based on the theoretical movements of a bubble in turbulent flow. A bubble can be assumed to be moving at its terminal velocity and its relative movement will continue at a steady pace. The drag force F_d and the inertial forces F_i can be balanced. This is illustrated in Figure 2.4. The F_d can be expressed in terms of the drag coefficient in equation (2.6). One important parameter to define is the Reynolds number for a bubble shown in equation (2.7).

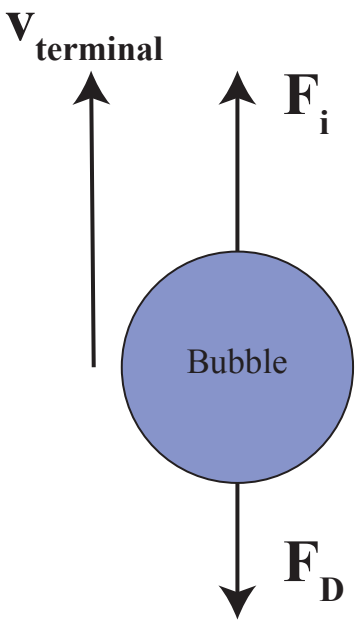

Figure 2.4: Bubble traveling at terminal velocity through a fluid.

$$F_d = \frac{C_d A \rho v_b^2}{2 g_c} = \frac{C_d \pi \mu^2 Re_b^2}{8 g_c \rho} \tag{2.6}$$

$$Re_b \equiv \frac{v_b d \rho}{\mu} \tag{2.7}$$

Plugging in the Reynolds number for a bubble, (2.6), and the area of a circle into (2.6), yields the drag force in the following form.

$$F_d = \frac{C_d \rho}{2g_c} \frac{Re_b^2 \mu^2}{d^2 \rho^2} \frac{\pi d^2}{4}$$
$$F_d = \frac{C_d \pi \mu^2 Re_b^2}{8 g_c \rho}$$

Given the two Re_b regimes, $Re_b \leq 2$ and $2 < Re_b \leq 200$, the drag coefficients C_d are:

For $Re_b \leq 2$

$$C_d = \frac{24}{Re_b} \tag{2.8}$$

For $2 < Re_b \leq 200$

$$C_d = \frac{18.5}{Re_b^{0.6}} \tag{2.9}$$

This yields a drag force of:

For $Re_b \leq 2$

$$F_d = 3\pi\mu^2 \frac{Re_b}{G_c \rho} \tag{2.10}$$

For $2 < Re_b \leq 200$

$$F_d = 18.5\pi\mu^2 \frac{Re_b^{1.4}}{8 g_c \rho} \tag{2.11}$$

The inertial forces in turbulent flow was found to be:

$$F_i \approx \frac{\mu^2}{\rho g_c} \left(\frac{d}{D}\right)^{8/3} Re^{11/6} \tag{2.12}$$

For Regime 1:

$$F_d = F_i$$
$$3\pi\mu^2 \frac{Re_b}{g_c\rho} = \frac{\mu^2}{g_c\rho}\left(\frac{d}{D}\right)^{8/3} Re^{11/6}$$
$$Re_b = \frac{1}{3\pi}\left(\frac{d}{D}\right)^{8/3} Re^{11/6}$$

This leaves the form of the correlation in relation to the Re_b:

$$Re_b \approx \left(\frac{d}{D}\right)^{8/3} Re^{11/6} \tag{2.13}$$

Given the forms for the Frőssling equation:

$$Sh_b \sim Re_b^{1/2} Sc^{1/2} \tag{2.14}$$

$$Sh_b \sim Re_b^{1/2} Sc^{1/3} \tag{2.15}$$

Using the relation for Sherwood number for a bubble $Sh \equiv (D/d)Sh_b$ and equations (2.13) , (2.14), and (2.15) the form yields:

$$Sh \sim Sc^{1/2} Re^{0.92} (d/D)^{1/3} \tag{2.16}$$

$$Sh \sim Sc^{1/3} Re^{0.92} (d/D)^{1/3} \tag{2.17}$$

For Regime 2:

$$F_d = F_i$$

$$18.5\pi\mu^2\frac{Re_b^{1.4}}{8g_c\rho} = \frac{\mu^2}{g_c\rho}\left(\frac{d}{D}\right)^{8/3} Re^{11/6}$$
$$Re_b = \left(\frac{8}{18.5\pi}\right)^{1/1.4}\left(\frac{d}{D}\right)^{8/4.2} Re^{11/8.4}$$

This leaves the form of the correlation in relation to the Re_b:

$$Re_b \approx \left(\frac{d}{D}\right)^{8/4.2} Re^{11/8.4} \tag{2.18}$$

Using the relation for Sherwood number for a bubble $Sh \equiv (D/d)Sh_b$ and equations (2.18) , (2.14), and (2.15) the form yields:

$$Sh \sim Sc^{1/2}Re^{0.66}(d/D)^{-0.2/4.2} \tag{2.19}$$

$$Sh \sim Sc^{1/3}Re^{0.66}(d/D)^{-0.2/4.2} \tag{2.20}$$

From Kress' work [20], using the form of equations (2.19) and (2.20), the empirical correlation was found to be equation (2.21). This result is also in the same form as shown in ref [30] for bubbles in turbulent concurrent flow.

$$Sh = 0.34\ Sc^{1/2}Re^{0.94}\left(\frac{d}{D}\right)^{1.0} \tag{2.21}$$

2.1.4 Mass Transfer in Stirred Bioreactors

Sparging mass transfer is also important in some stirred tank bioreactors. An schematic of a stirred tank bioreactor is shown in Figure 2.5. In some of these types of reactors, turbulent mass transfer is utilized. Garcia-Ochoa (2005) [31] had

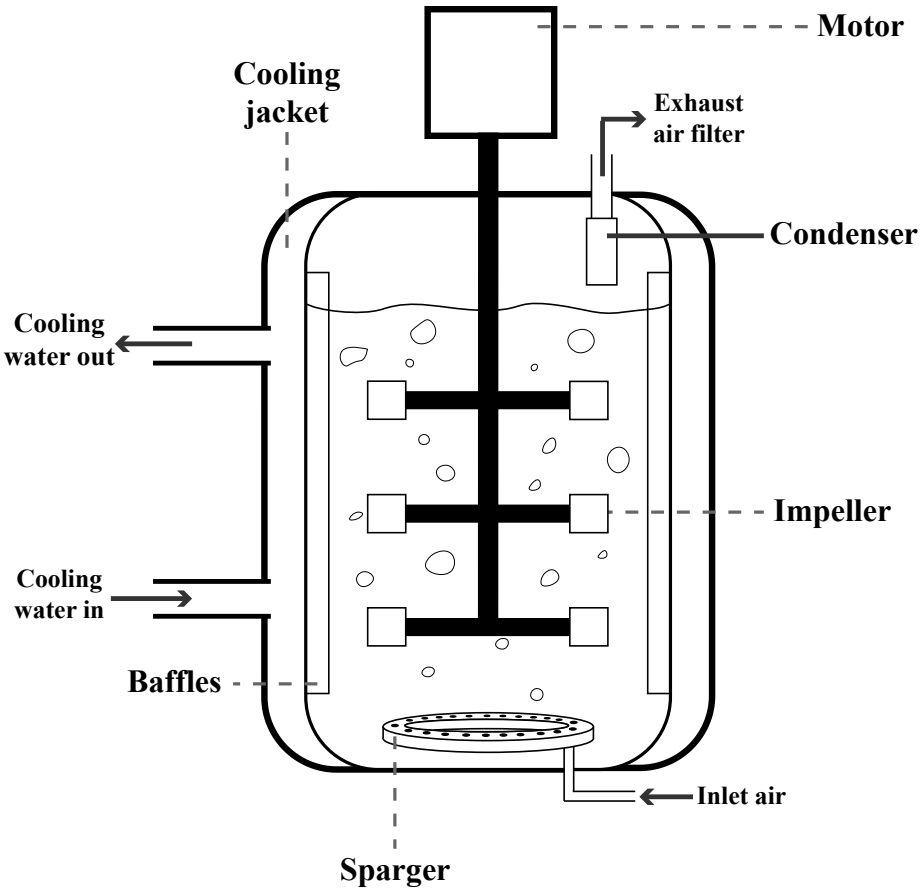

Figure 2.5: Schematic Diagram of a Stirred Tank Bioreactor

utilized the Ostwald-de Waele rheological model for describing non-Newtonian fluids and define t_e as shown in equation(2.22).

$$t_e = \left(\frac{K}{\epsilon\,\rho}\right)^{\frac{1}{(1+n)}} \tag{2.22}$$

The t_e in equation (2.22) can be used in Higbie's surface renewal model, equation

(2.4). This yields a k_L relation in equation (2.24)

$$k_L = 2\sqrt{\frac{\mathscr{D}}{\pi}}\left(\frac{\epsilon\,\rho}{K}\right)^{\frac{1}{2(1+n)}} \tag{2.23}$$

This form describes non-Newtonian fluids where K is the consistency index in the power-law model and n is the flow index in power-law model. When applying this to Newtonian fluids, $K = \mu$ and $n = 1$, equation (2.23) becomes equation (2.24) [32].

$$k_L = 2\sqrt{\frac{\mathscr{D}}{\pi}}\left(\frac{\epsilon\,\rho}{\mu}\right)^{\frac{1}{4}} \tag{2.24}$$

The turbulence energy dissipation term ϵ is calculated using the following relation from Lamont in ref [33]. It relates Re, ν, and bubble diameter to ϵ.

$$\epsilon = 0.16\ Re^{2.75}\frac{\nu^3}{D^4} \tag{2.25}$$

Rewriting kinematic viscosity as $\nu = \frac{\mu}{\rho}$, equation (2.24) can be written as equation (2.26)

$$k_L = 2\sqrt{\frac{\mathscr{D}}{\pi}}\left(\frac{\varepsilon}{\nu}\right)^{\frac{1}{4}} \tag{2.26}$$

2.1.5 Bubble Swarm Mass Transfer

This correlation considers bubble swarms in columns, not solely single bubble mass transfers [34]. This phenomenon is very difficult to quantify and model. The best approximation this behavior is dimensional analysis, and through dimensional analysis

it can be shown that the liquid mass transfer coefficient to a function of:

$$\frac{k_L d_{vs}}{D_L} = f\left(\frac{\nu_L}{D_L}, \frac{g d_{vs}^3}{\nu_L^2}, \frac{g\nu_L^4\rho_L^3}{\gamma^3}, \sigma, \varepsilon_G\right) \tag{2.27}$$

This can also be written in terms of Sc and Ga.

$$\frac{k_L d_{vs}}{D_L} = f\left(Sc, Ga, \frac{g\nu_L^4\rho_L^3}{\gamma^3}, \sigma, \varepsilon_G\right) \tag{2.28}$$

The left hand side is the Sh, and the variables are:

D_L = Liquid phase diffusivity

ρ_L = Density of liquid

ν_L = Kinematic viscosity of liquid

d_{vs} = mean bubble size

ε_G = Gas holdup, fraction of total vulume of aerated liquid, dimensionless

σ = standard deviation of bubble size distribution

γ = surface tension

Bubble velocity is also a factor, but since there is no accurate method of determining the velocity or average velocity of a bubble swarm, the mass transfer coefficient is then approximated by using equation (2.27).

Akita had determined, empirically, that the function for Sh is in the form:

$$Sh = 0.5\left(\frac{\nu_L}{D_L}\right)^{1/2}\left(\frac{g d_{vs}^3}{\nu_L^2}\right)^{1/4}\left(\frac{g\nu_L^2\rho_L}{\gamma}\right)^{3/8} \tag{2.29}$$

this can be rewritten with non-dimensional numbers as:

$$Sh = 0.5 Sc^{1/2} Ga^{1/4} Bo^{3/8} \tag{2.30}$$

Isolating the liquid mass transfer coefficient:

$$k_L = 0.5 g^{5/8} D_L^{1/2} \rho_L^{3/8} \gamma^{-3/8} d_{vs}^{1/2} \tag{2.31}$$

2.1.6 Specific Interfacial Area

The specific interfacial area (a) is the link between the volumetric mass transfer coefficient (k_La) and the liquid-side mass transfer coefficient (k_L) as shown in the relation (2.32). The k_La is relatively easy to gather from data. In this case, it can be easily gathered from the dissolved oxygen (DO) vs time data using equation (2.33). In order to compare the theoretical models to the data, getting the specific interfacial area is necessary.

$$a = \frac{k_L a}{k_L} \tag{2.32}$$

$$\frac{dC}{dt} = k_L a(C_0 - C) \tag{2.33}$$

The a is defined by the ratio of a single bubble surface area, volume, and gas hold up ε_G. This can be reduced to (2.35), simply making it a function of holdup and average bubble diameter (d_b).

$$a = \frac{A}{V_D} = \frac{A\varepsilon_G}{V_G} \tag{2.34}$$

$$a = \frac{6\varepsilon_G}{d_b} \tag{2.35}$$

In a bubble reactor, there are many correlations to calculate this value. For example Deckwer [35] has noted equations (2.36) and (2.37) as viable correlations

for specific interfacial area in a column bubble reactor.

$$a = 34.4\ u_g^{1/4} \varepsilon_G \tag{2.36}$$

$$a = 8.54\ u_g^{-0.12} \varepsilon_G \tag{2.37}$$

The gas holdup calculation is simply the ratio of gas or liquid in a gas in liquid dispersion. In a column bubble reactor it is the percent change in height, equation (2.38). But more generically, it would be the percent change in volume, equation (2.39). There are also quite a number of correlations to calculate ε_G in refs [35, 36, 37].

$$\varepsilon_G = \frac{L_B - L_0}{L_0} \tag{2.38}$$

$$\varepsilon_G = \frac{V_B - V_0}{V_0} \tag{2.39}$$

For this work, all the correlations would not be applicable because they were all assuming a column reactor, whereas the experiments described in this work are concurrent flow experiments. So, in order to calculate an accurate a, all values in equation (2.35) must be measured experimentally.

2.2 Acoustic Intensity and Transmission

The energy range involved in acoustic intensity spans several orders of magnitude. The perceived loudness of sound is the sound intensity, which is defined as the energy

passing perpendicular to an area per unit time. So, a higher intensity would be perceived as a louder sound. Due to the large range of orders of magnitude that are relevant acoustics the decibel, dB, was adopted as a unit of measure. The dB is a unitless and comparative metric. The decibel unit of note is the decibel sound power level, $dB(SPL)$, which can be related to sound pressure, P, or intensity, I, as shown in equation (2.40). The reference point (0 dB) is defined based on the minimum human ear sensitivity at $P_0 = 10\ \mu Pa$ in air and $I_0 = 10^{-12}\ W/m^2$. Additionally, the reference for sound pressure in solids and liquids is $P_0 = 10^{-6}\ Pa$ [38].

$$dB(SPL) = 20\log\left(\frac{P}{P_0}\right) = 10\log\left(\frac{I}{I_0}\right) \tag{2.40}$$

Table 2.1: Decibel to Acoustic Intensity Reference with tangible examples.

$dB(SPL)$	Intensity	Example
140	$10^2\ W/m^2$	Aircraft carrier deck, pain threshold
120	$10^0\ W/m^2$	Thunder clap, police siren, extremely loud
100	$10^{-1}\ W/m^2$	Factory noise, motorcycle, extremely unpleasant
80	$10^{-4}\ W/m^2$	Garbage disposal/machinery, unpleasant
60	$10^{-6}\ W/m^2$	Normal conversation
40	$10^{-8}\ W/m^2$	Library
20	$10^{-10}\ W/m^2$	Whisper, rustling leaves
0	$10^{-12}\ W/m^2$	Threshold of human hearing

The transmission of acoustic energy through various media are affected by acoustic impedance and interfaces. The acoustic impedance is defined in equation (2.41) as the product of the medium density (ρ) and speed of sound in that material (c). Given an infinite plane pressure wave perpendicularly incident onto an infinite interface of two media, the wave has two possibilities, transmission through the interface or reflection as shown in Figure 2.6. The sum of the reflected pressure, P_R, and the transmitted pressure, P_T, will equal the incident pressure P_{total}. The ratio of the incident pressure that is transmitted or reflected are shown in equations (2.42) and

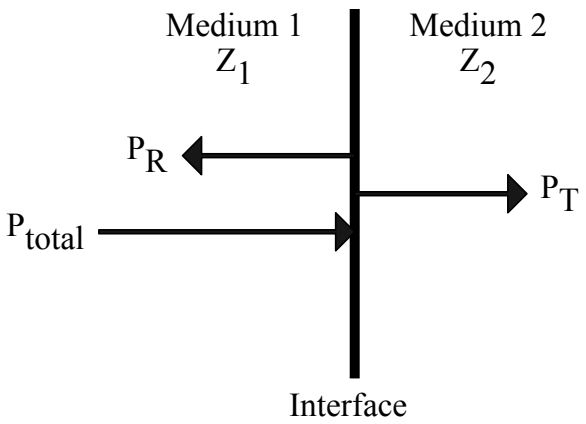

Figure 2.6: Diagram of an infinite plane pressure wave perpendicularly incident on an interface.

(2.43), respectively. Subsequently, to relate the ratio of the transmitted and reflected intensities are shown in equations (2.44) and (2.45) [21, 39, 40]. These equations can also be used for semi-infinite media as well [21].

$$Z = \rho c \tag{2.41}$$

$$T_P = 2\frac{Z_2}{Z_1 + Z_2} \tag{2.42}$$

$$R_P = \frac{Z_2 - Z_1}{Z_1 + Z_2} \tag{2.43}$$

$$\frac{I_T}{I} = \frac{Z_1}{Z_2}|T_P|^2 \tag{2.44}$$

$$\frac{I_R}{I} = |R_P|^2 \tag{2.45}$$

When designing acoustic interfaces, it is important to match impedances as closely as possible to maximize transmission. Transmission of acoustic energy between two media that have significantly different may be necessary. A relevant example to the PULST experiment in Chapter 4 is an aluminum/water interface. In this example of Al ($Z_{Al} = 17.10\ MRayl$) and water ($Z_{water} = 1.483\ MRayl$, the transmission ratio is calculated using equation (2.44) is 29.4%. In order to maximize the transmission from two media that have such different acoustic impedances, an intermediate matching layer can be used. As described by Kino [41], an intermediate layer is a medium with quarter wavelength thickness with a matching acoustic impedance shown in equation (2.46). For the water/aluminum interface example, the transmission with an intermediate layer of variable acoustic impedance is shown in Figure 2.7, which shows a maximum transmission ratio of 49.1% at the matching impedance (Z_m) point.

$$Z_{match} = \sqrt{Z_1\ Z_2} \tag{2.46}$$

Bubbles and bubble layers provide substantial attenuation to acoustic intensity. When acoustic waves encounter a bubble layer in a medium, significant energy loss will occur. This is due to bubbles acting as a source of energy dissipation, through thermal and dispersive mechanisms, and acoustic scattering [40]. This technique of using bubble curtains has been employed in the past for acoustic shielding of Navy destroyers [42], explosive shock wave shielding [42], and acoustic insulation for the protection of sea animals during loud underwater construction [43, 44, 45]. The noise reduction of the bubble curtains is roughly 10 to 20 $dB\ re\ \mu Pa$ [46]. This intensity

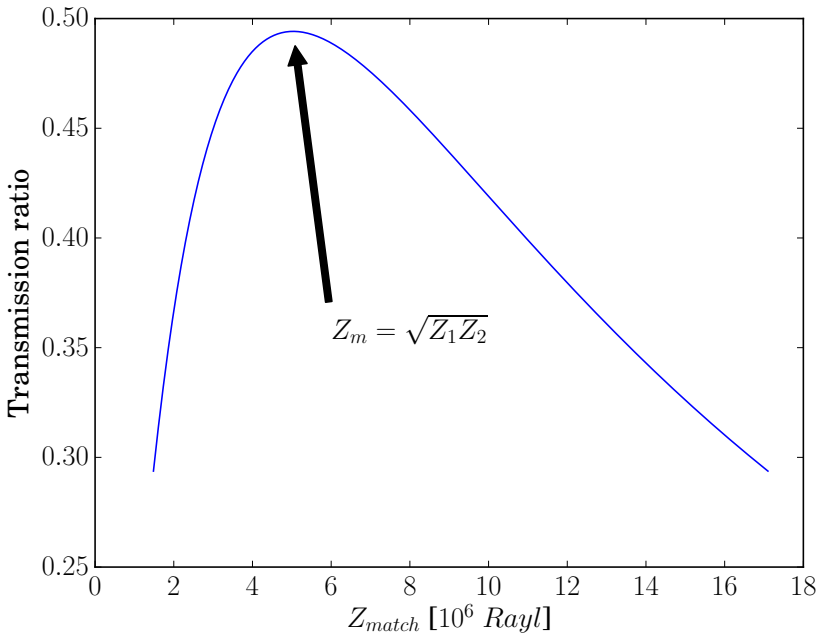

Figure 2.7: Intensity transmission between water ($Z_{water} = 1.483\ MRayl$) and aluminum ($Z_{Al} = 17.10\ MRayl$) for a range of matching layer impedances.

attenuation is described by equation (2.47) where the resultant intensity (I), is a function of the incoming intensity (I_0), bubble density (N_b), extinction cross section (σ_e), and thickness of the bubble layer (z) [40].

$$I = I_0 \exp(-N_b \sigma_e \ z) \tag{2.47}$$

The extinction cross section is generally described by equation (2.48) where R_0 is the resonant radius, ω_{res} is the resonant period, c is the speed of sound, and ϱ is the dampening coefficient [47].

$$\sigma_e = \frac{4\pi R_0^2}{\varrho_{res}/\varrho^2 - 1 + \varrho^2} \frac{\varrho}{\omega R_0/c} \tag{2.48}$$

2.3 Sonomechanical Theory

Most of the demonstrated non-medical applications of sonoprocessing processing with high power ultrasonics take advantage of sonically induced cavitation [21, 48]. The bubble formation and related energy exchange are transient, involve high pressures and temperatures. The behavior is nonlinear by nature and challenging to describe, particularly when multi-phase (slurry or catalytic particles) and multi-bubble phenomena occur [21, 49, 40, 50, 51]. Ultrasonics is in essence a tool that can be used to deliver energy into a medium. This sonic energy can then be manifested in interactions as vibrations and mechanical motion (acoustic streaming), heat (through rapid bubble compression and absorption), and light (sonoluminescence) all through cavitation and the related absorption and dissipation of the sonic energy. There are many factors that affect the sonically induced phenomena within a fluid, including temperature, pressure and fluid thermophysical properties. In order to comprehensively describe this behavior, the whole spectrum of phenomena must be considered ranging from interactions in single-phase fluid with relatively low intensity ultrasound to multi-phase slurry with high ultrasound intensity systems. There is also a further complication due to the spatial variations in the phenomena that occur at varying distances from the sonic source within a reactor, and all the complexities associated with variations caused by properties such a bubble density. The following is a brief discussion of key topics.

2.3.1 Cavitation

Cavitation is the formation of a vapor bubble in a fluid and its subsequent collapse. An acoustic wave is a traveling oscillating compression wave with compression and rarefaction regions. Ultrasonic cavitation occurs when a bubble is formed during the rarefaction period of a acoustic wave where the lowest pressures are induced and the

subsequent collapse during the compression part where the pressures are highest. The collapse event results in very high temperatures and pressure on the order of $5000°C$ and 2000 atm, illustrated in Figure 2.8. This phenomenon has been investigated and documented extensively [21, 40, 50, 51, 49, 52]. The threshold for cavitation is a fundamental boundary in any process application and cavitation thresholds are affected by many factors. The most important factors are the static pressure and temperature (as it controls fluid properties), the presence of dissolved gas and/or particulate matter, fluid viscosity, the frequency of the applied ultrasound, and the wave induced pressure variation [52]. When gas and/or particulates are present in a fluid, these contaminants introduce "weak points" in the fluid, which results in a lowering of the cavitation threshold. Viscosity describes the cohesive forces in a fluid and, in general, the transient acoustic pressure needed to cause cavitation varies directly with viscosity. Considering the effect of temperature, the pressure required for cavitation is inversely proportional to temperature. When the applied ultrasonic fields are considered, the intensity at which cavitation occurs is dependent on the frequency, and at higher frequencies it takes greater plane wave intensities to induce cavitation [21, 52, 53], see Figure 2.9.

The nature of ultrasonic cavitation can be considered in two categories, stable and transient cavitation. In stable cavitation, a bubble will oscillate with the sound field for several cycles or more of the applied wave field. During this time, the bubble may grow due to rectified diffusion. Rectified diffusion is the growth of a gas bubble driven into oscillation by an appropriate acoustic field [54]. Once the bubble reaches its critical radius, it will collapse. In transient cavitation, an oscillating bubble can collapse in one or at most only a few acoustic cycles. However, the distinction between stable and transient cavitation has historically varied between authors, which has caused some confusion. There have been attempts to reconcile these different descriptions, but the basic distinctions have been the bubble life in relation to the period of the applied field and the time it has taken before bubble

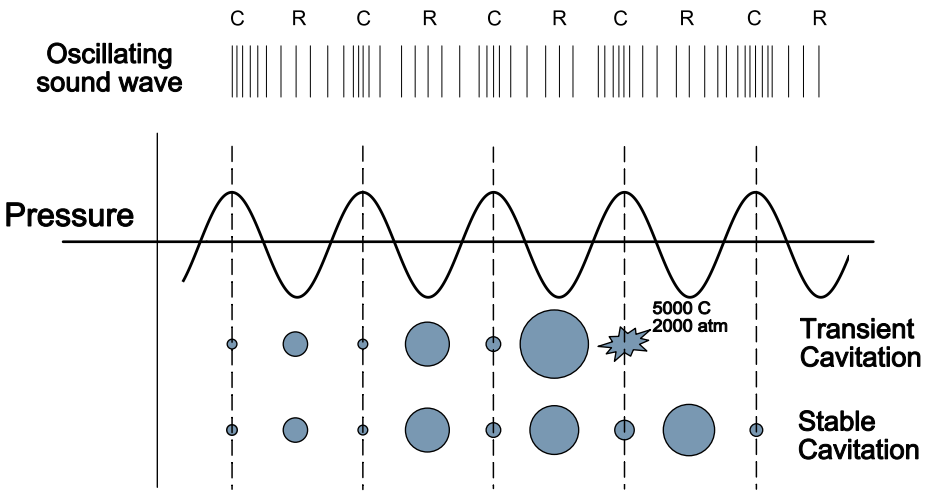

Figure 2.8: Illustration of stable cavitation bubbles and the lifetime of transient cavitation bubbles in relation to an oscillating sound wave represented visually as compression (C) and rarefaction cycles (R). [26]

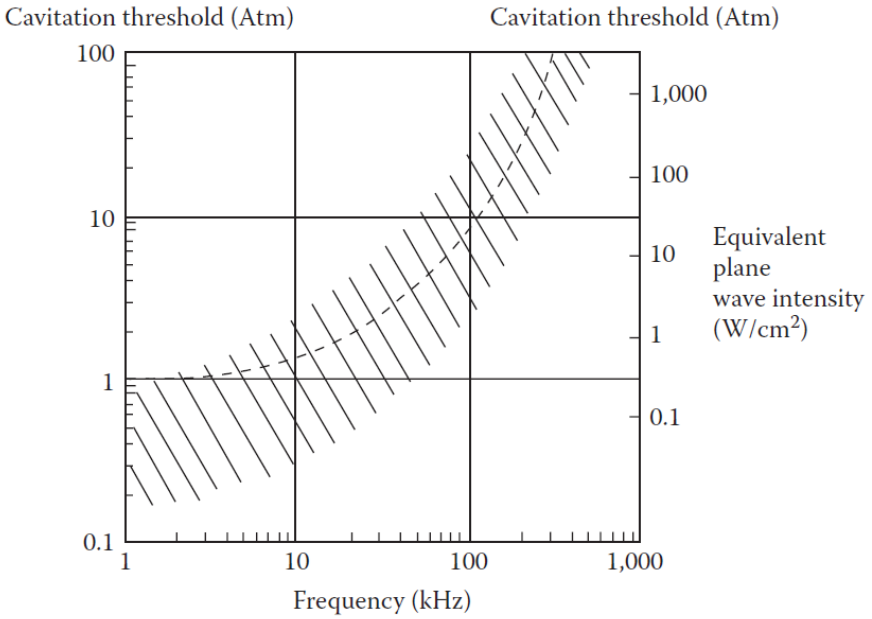

Figure 2.9: Frequency dependence for the cavitation threshold with continuous wave applied to fresh water at atmospheric pressure. [21, 53]

collapse or the violence of the collapse [40, 50, 52]. In general transient cavitation has tended to cause higher peak pressures and temperatures in the collapsing bubbles. These two phenomena are illustrated in Figure 2.8 in relation to the compression and rarefaction of an oscillating sound wave.

2.3.2 Rayleigh-Plesset

The Rayleigh-Plesset equation, as shown in equation (2.49), describes the simple motion of a pulsing spherical bubble [40, 52, 55]. This equation was developed from the work of many authors, but it is now simply referred to as the "Rayleigh-Plesset Equation" [40]. It explains the time relation of a bubble radius (R) in an oscillating pressure field with a source at some distance away. The important pressures of note are the static pressure on the fluid (p_0) as well as the oscillating pressure ($p(t)$). Other factors that affect the behavior of the forced bubble are fluid properties, namely, density (ρ), surface tension (σ), sheer viscosity (η), the polytropic constant (κ), and the vapor pressure (p_v).

$$R\ddot{R} + \frac{3}{2}\dot{R}^2 = \frac{1}{\rho}\left[\left(p_0 + \frac{2\sigma}{R_0} - p_v\right)\left(\frac{R_0}{R}\right)^{3\kappa} + p_v - \frac{2\sigma}{R} - \frac{4\eta\dot{R}}{R} - p_0 - p(t)\right] \quad (2.49)$$

The solutions to this equation can describe both stable and transient cavitation. The Rayleigh-Plesset is very non-linear and asymmetric in terms of compression and expansion [40]. A solution, adapted from [56], is shown for water at 101 kPa, 20°C, and $f = 20\ kHz$ in Figure 2.10 for intensities of 275 W/cm^2 and 0.085 W/cm^2, which correspond to the SUMATRA and PULST conditions. The figure shows the time evolution of a bubble at the resonance radius with respect to the driving acoustic pressure.

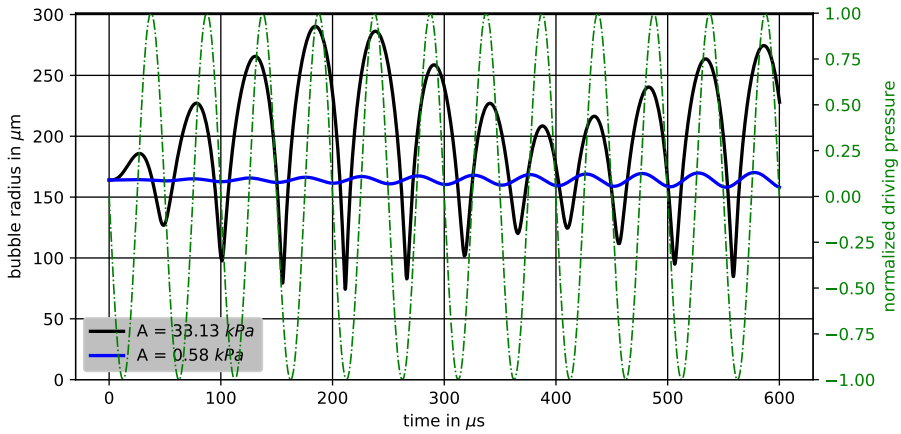

Figure 2.10: Solution to the Rayleigh-Plesset equation for PULST (blue) and SUMATRA (black) experimental conditions.

2.3.3 Resonance Radius

The most simple resonant situation is a single freely oscillating bubble in an infinite fluid volume with the assumption that the effects of surface tension and viscous attenuation are negligible. This simplified system is documented as the Minnaert resonance and describe by equation (2.50). The Minnaert resonance relates the frequency (f) to the polytropic coefficient (κ), ambient pressure (p_0), and fluid density (ρ).

$$f = \frac{1}{2\pi R_0}\left(\frac{3\kappa p_0}{\rho}\right)^{1/2} \tag{2.50}$$

The Rayleigh-Plesset equation (2.49) describes the forced bubble. The forced bubble given a small applied wave field amplitude assumption yields a resonance frequency of:

$$\omega_0^2 = \frac{1}{\rho R_0^2}\left[3\kappa\left(p_0 + \frac{2\sigma}{R_0}\right) - \frac{2\sigma}{R_0}\right] \tag{2.51}$$

When surface tension is negligible, equation (2.51) reduces to equation (2.50) [40, 52].

Given the assumptions and conditions of an ideal gas ($\kappa \approx 1.4$) and the fluid is $20°C$ water, the solution between the frequencies of 10 kHz and 10 MHz are shown in Figure 2.11. This result is compared to the local conditions of Albuquerque, New Mexico ($P_a = 84.2\ kPa$). It can be seen that the change in atmospheric pressure is significant to the resonance diameter.

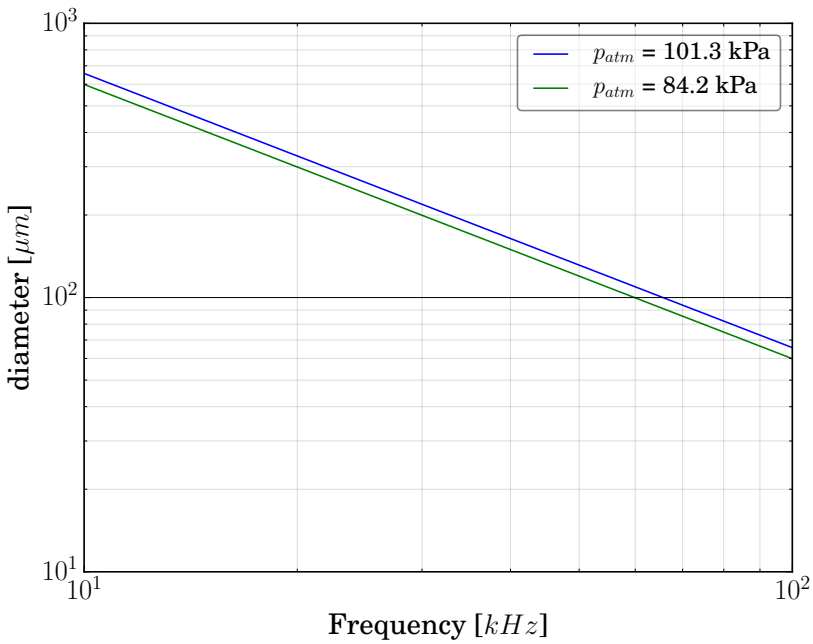

Figure 2.11: Minnaert Resonance diameters calculated for standard conditions at $p_{atm} = 101.3\ kPa$ and local conditions (Albuquerque, NM $p_{atm} = 84.2\ kPa$)

2.3.4 Fields and Interaction Zones

When ultrasonics is applied to a fluid, three interaction regions emerge. These are near horn, streaming zone, and far-field. The near-horn region, typically within one wavelength from the source is subjected to the highest intensities. Multiple bubbles can be observed forming and collapsing. The streaming zone, typically starting at

about one wavelength from the horn, extends out several wavelengths, and it is subjected to lower intensities, commonly below the cavitation threshold. Its major feature is the streaming field of bubbles, which move out from the near-horn region. The far-field is at some distance where major acoustic streaming has ceased. It is characterized by the lack of macro-streaming effects and energy is mostly dissipated through heating [21, 51]. These regions are illustrated in Figure 2.12.

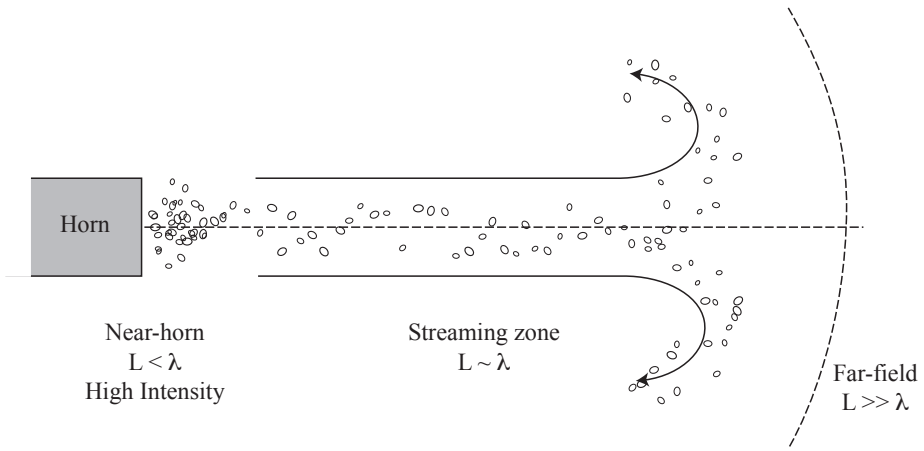

Figure 2.12: Ultrasonic interaction zones adapted from Ensminger, 2011 [21].

The utilization of high power ultrasonics has three fundamental arrangements. The first has the horn placed on or very near (within one wavelength) of the surface. The second arrangement is where the horn is at or around one wavelength from the surface, or reflector, which produces a standing wave that can be utilized for separation applications. The third arrangement is where the horn is submerged in a large (effectively a semi-infinite) container where the container surface is far from the horn [21]. These arrangements are illustrated in Figure 2.13.

All acoustic waves in a fluid have an associated radiative force exerted into a fluid. These forces originate from the acoustic source, like a transducer or horn. These forces that are due to the source are classified as primary forces or primary Bjerknes forces. Any reflection or re-emission or acoustic waves also have associated radiative

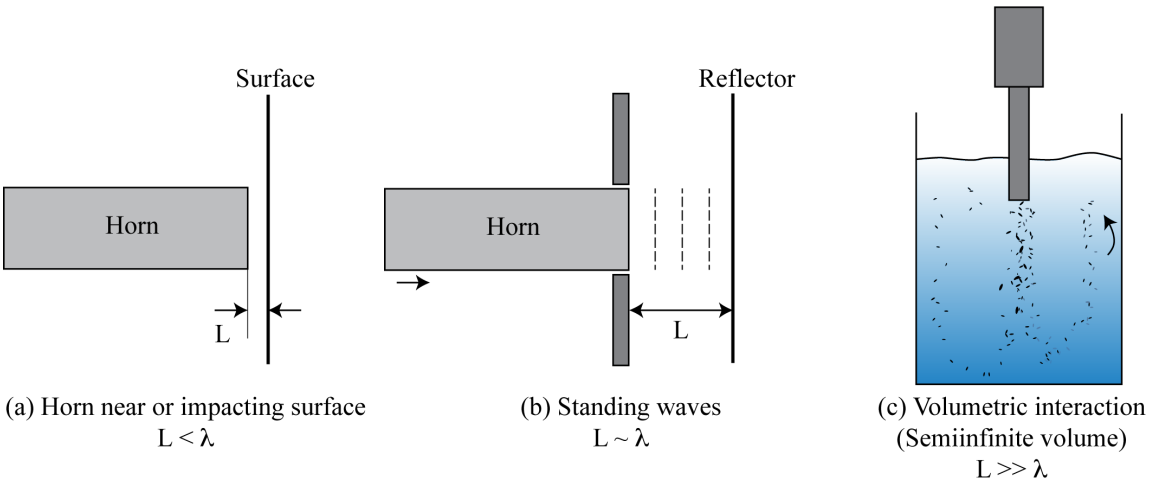

Figure 2.13: Interaction arrangements with various horn/surface separations, adapted from Ensminger, 2011 [21].

forces. For instance, a bubble in an acoustic field can act as a re-emitter which can apply a force on any surrounding bubbles, as illustrated in Figure 2.14. The force due to inter-bubble oscillation are classified as mutual or secondary Bjerknes forces. In general, Bjerkens forces attract bubbles or particles at or below the resonance diameter for the sonic field to an anti-pressure node and those larger that resonance diameter will travel away from those nodes [40]. If the ultrasonic intensity is high enough, these forces can even rip apart bubbles that are in the ultrasonic field. These forces are very difficult to predict or approximate because of their highly nonlinear behavior.

Primary Bjerkens forces are easier to predict because they originate from a fixed horn and geometry, but the secondary forces are much more unpredictable. Because the secondary forces come from any reflective surface including entrained particles and oscillating bubbles themselves, they can be quite chaotic. The intensity, location, and spatial dimensions of the forces will vary wildly because the sources vary significantly in terms of bubble size and location [40], which also depend on fluid properties including the vapor pressure.

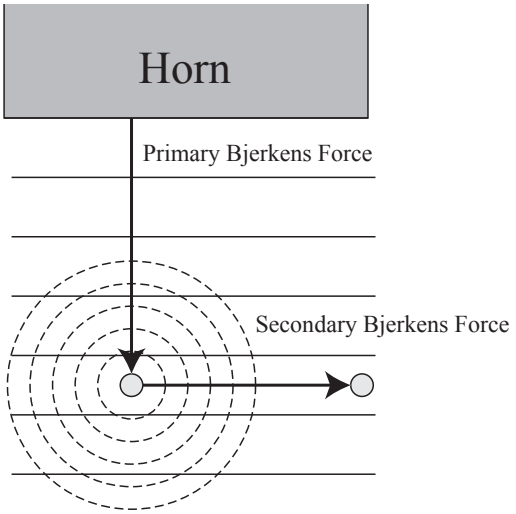

Figure 2.14: Illustration of radiative forces.

2.4 Similitude

To show that the current experimental efforts are commensurate to prototypical conditions, scaling arguments were made through the characteristic non-dimensional numbers for mass transfer. As described by Kline [57], similitude can be established by matching non-dimensional numbers and scaling ratios between the prototype and model systems. Scaled model experiments are attractive because they can provide meaningful data at convenient lab conditions when the prototype conditions are difficult to achieve. This has been done successfully for scaled heat transfer experiments supporting the FHR by using Dowtherm A as a surrogate fluid for flibe [58]. In this, and the subsequent work, the key non-dimensional numbers matched were Re, Pr and Nu. For mass transfer, the key non-dimensional numbers that need to be matched are Re, Sc, and Sh. One more non-dimensional number, the Weber number (We) is required to fully describe the behavior, because of the importance of the surface tension forces. The surrogate for mass transfer to match a flibe/tritium system is a mixture of water and glycerol and the liquid and oxygen as the gas [20,

59].

The non-dimensional numbers and parameters will be designated as model (m) and prototype (p). The model will denote that that parameter is for the scaled down glycerol/water mixture and the prototype will denote the FHR conditions for flibe at operating temperature. Note that L is a characteristic length corresponding to D (duct diameter) in equation (2.21).

$$Re_m = Re_p \rightarrow \frac{U_m L_m}{U_p L_p} = \frac{\nu_m}{\nu_p} = \frac{\mu_m \rho_p}{\mu_p \rho_m} \tag{2.52}$$

$$Sc_m = Sc_p \rightarrow \frac{\mu_m}{\mu_p}\frac{\rho_p}{\rho_m} = \frac{\mathscr{D}_m}{\mathscr{D}_p} \tag{2.53}$$

$$We_m = We_p \rightarrow \frac{U_m^2 L_m}{U_p^2 L_p} = \frac{\sigma_m \rho_p}{\sigma_p \rho_m} \tag{2.54}$$

$$\frac{d_m}{L_m} = \frac{d_p}{L_p} \rightarrow \frac{d_m}{d_p} = \frac{L_p}{L_m} \tag{2.55}$$

The relations in equations (2.52), (2.53), (2.54), and (2.55) can be rearranged to find the length and flow velocity relation as shown in equations (2.56) and (2.57).

$$\frac{L_p}{L_m} = \frac{\sigma_p \rho_m}{\sigma_m \rho_p} \left(\frac{\mathscr{D}_m}{\mathscr{D}_p} \right)^2 \tag{2.56}$$

$$\frac{U_m}{U_p} = \left(\frac{L_p \ \sigma_m \ \rho_p}{L_m \ \sigma_p \ \rho_m} \right)^{1/2} \tag{2.57}$$

The length and flow velocity ratios are shown in figures 2.15 and 2.16. Over the range of the FHR operating range, the scaling factor for the length and velocity are about 0.6 and 0.94. This shows that the scaling factor for these experiments are viable models for the prototype FHR conditions.

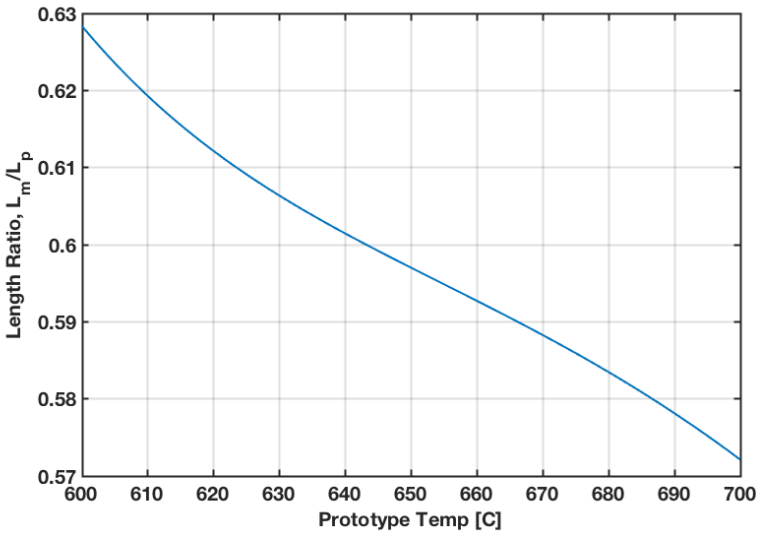

Figure 2.15: Model to prototype length ratio for the model water/glycerol model with respect to the prototype operating range of the FHR conditions.

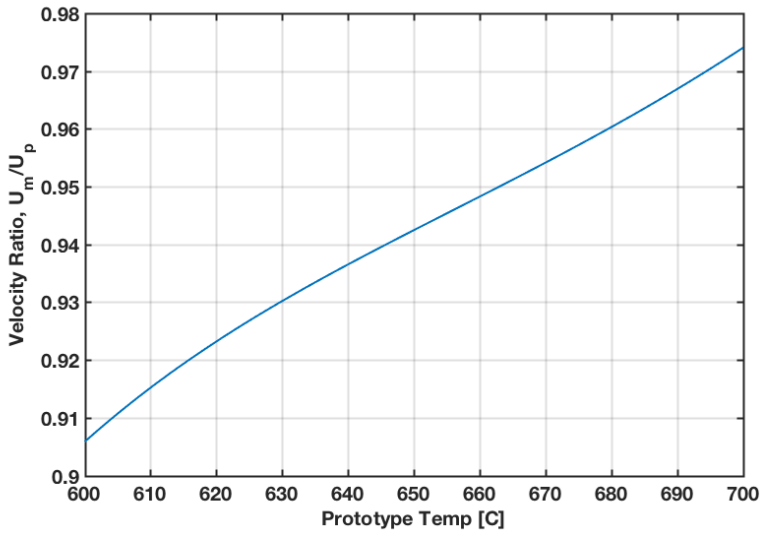

Figure 2.16: Model to prototype flow velocity ratio for the model water/glycerol model with respect to the prototype operating range of the FHR conditions.

The acoustic contribution to mass transfer can be captured by dimensional analysis, even though the specific contributions of each parameter is unknown. The formal method of development of an acoustic non-dimensional number is the Buckingham Pi theorem [60]. This theorem state that given some physically meaningful statement with k variables with the same units as shown in equation (2.58).

$$u_1 = f(u_2, u_3, ..., u_k) \tag{2.58}$$

$$\Pi_1 = \phi(\Pi_2, Pi_3, ..., Pi_{k-r}) \tag{2.59}$$

It shows that equation (2.58) can be rewritten as a set of dimensionless products or "Π terms" as shown in equation (2.59) where k is the number of variables, r is the minimum number of reference dimensions, $k - r$ is the required number of Π terms, and $\phi(\Pi_2, Pi_3, ..., Pi_{k-r})$ is some function of Π_2 through Π_{k-r}. This method is used

in development of an acoustic term for the SUMATRA experiment and is detailed in Chapter 3.4.

Chapter 3

SUMATRA Experiment

The first experiment detailed in this dissertation is the Scaled Ultrasonic Mass Transfer (SUMATRA) experiment. The goal of the SUMATRA experiment was to build and evaluate a scaled prototype for an ultrasonic sparging cell, which was submitted for archival publication [59]. This investigation began with two exploratory studies. These studies demonstrated applying acoustic energy can tune bubble size and acoustic pulsing is required to ensure bubbles get into the near field. The insights from the exploratory studies were employed in the SUMATRA experiment which had demonstrated initial proof-of-concept of sonomechanically enhanced mass transfer.

3.1 Exploratory Studies

This section reports the process used for the exploratory experiments and the insights produced from data given by the experiments. The general strategy of this work is to iteratively perform a series of experiments of increasing complexity. In total, there were two experiments that were the precursors to the SUMATRA experiment detailed in the sections 3.1.1 and 3.1.2 of this chapter.

The first experiment was designed to provide operational knowledge and expertise in using ultrasonics coupled with sparging, as well as to understand the behavior of ultrasonics and bubbles in a static flow setting. The second experiment was a first attempt at making a laboratory scale mass transfer loop with ultrasound. Subsequently, the SUMATRA experiment was designed and developed.

3.1.1 Ultrasonic Bubble Resonance Study

The purpose of the resonance studies was to investigate the behavior of injected bubbles. The bubbles in an ultrasonic field were expected to maintain a predictable bubble radius [40, 61]. Furthermore, this study is to develop the capabilities needed to produce and visualize bubbles of the appropriate diameter and subject them to an ultrasonic field.

The design of this experiment was very simple. It uses a clear acrylic tube surrounded with a visualization box and an ultrasonic horn imparting the ultrasonic energy. The ultrasonic generator was a Sonics and Materials VCX 750 with two probes, a 12.7 mm (0.5 in) and a 47.6 mm (1.875 in) diameter face. The maximum output of the generator is 750 W and the system auto tunes the output to a frequency of 20 kHz. The bubbles were injected through a capillary tube through the bottom as seen in Figure 3.1. The capillary tube that was selected, after a series of trials, was a teflon coated 25 μm ID tube. The bubble videos and images were taken with a Fastec IL13043001 model IL3100SM4 camera.

The operational setup used the high speed camera focused on the bubble stream in the acrylic tube as illustrated in Figure 3.1 and 3.2. The probe was placed 1 wavelength, what was calculated to be 74 mm for water at 20 kHz, above the bottom of the test section. This configuration gives an acoustic standing wave between the horn and the bottom of the test section, as illustrated in Figure 3.1a.

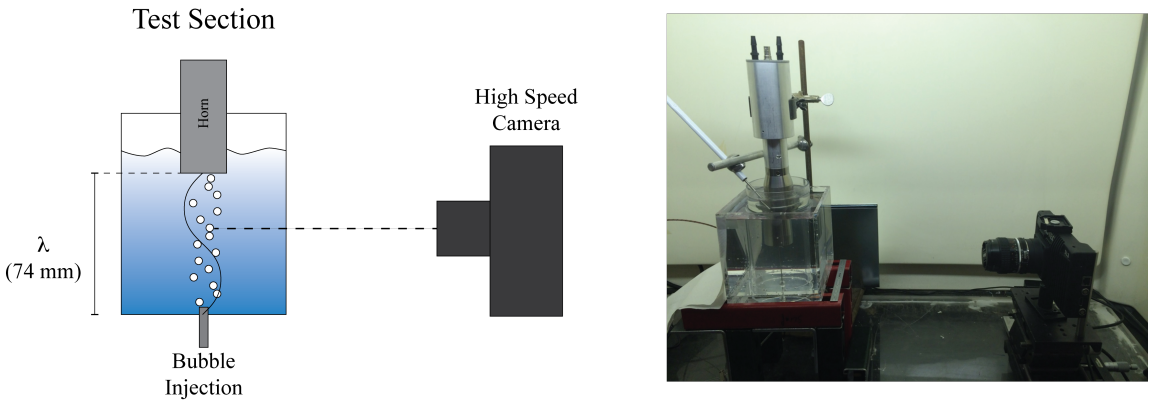

Figure 3.1: Bubble Resonance Experiment: a) Experiment cross section view. b) Side view of the bubble resonance experiment.

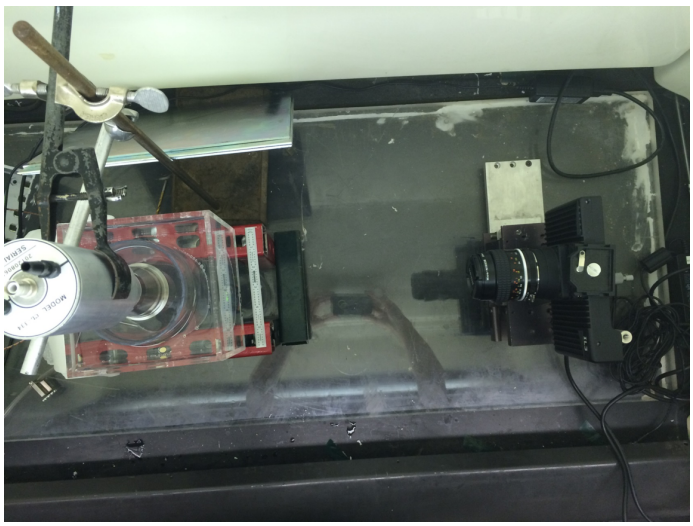

Figure 3.2: Top View of the bubble resonance experiment.

The experience was that the bubbles tried to maintain a resonant radius when acoustic energy was applied as shown by Figure 3.3. The sonicated bubbles were oscillating between an estimated 400 μm and 600 μm, which are larger than the cal-

culated resonant diameter of 200 μm. This is understandable because the high speed camera will only record the maximum diameter due to the frame rate restrictions. The camera was only able to reach 5600 fps, much slower than the 20 kHz applied. The key conclusion is that the bubbles will tend to a specific size. This is evident in Figure 3.3 because of the behavior of the bubbles coalescing and breaking apart around an observed diameter.

There were some other key observations made. There was indeed a streaming effect that pushed bubbles out of the near-field, which confirms observation reported in the current literature [21, 40, 39, 49, 51, 62] about the ultrasonic fields. In order to obtain bubbles in the near-field, the ultrasonics had to be pulsed. The ultrasonic generator had a pulsing function that would pulse on for 1 second and off for 1 second. In an attempt to get bubbles in the near-field, a small pump was installed. The pumping was found to be unsuccessful in forcing bubbles into the near-field without pulsing. The radiative forces emanating from the horn would push bubbles away from the near-field, and the pumping could not overcome these radiative forces to push the bubbles into the near-field. This is evident in Figure 3.4 frames C, D, E, and F. These frames show the bubbles are unable to be pumped into the near-field. During the pulsing, the bubbles traveled to nodes which confirms the behavior where a standing waves are able to sort and stratify particles and bubbles as shown in frames D, E, and F of Figure 3.4.

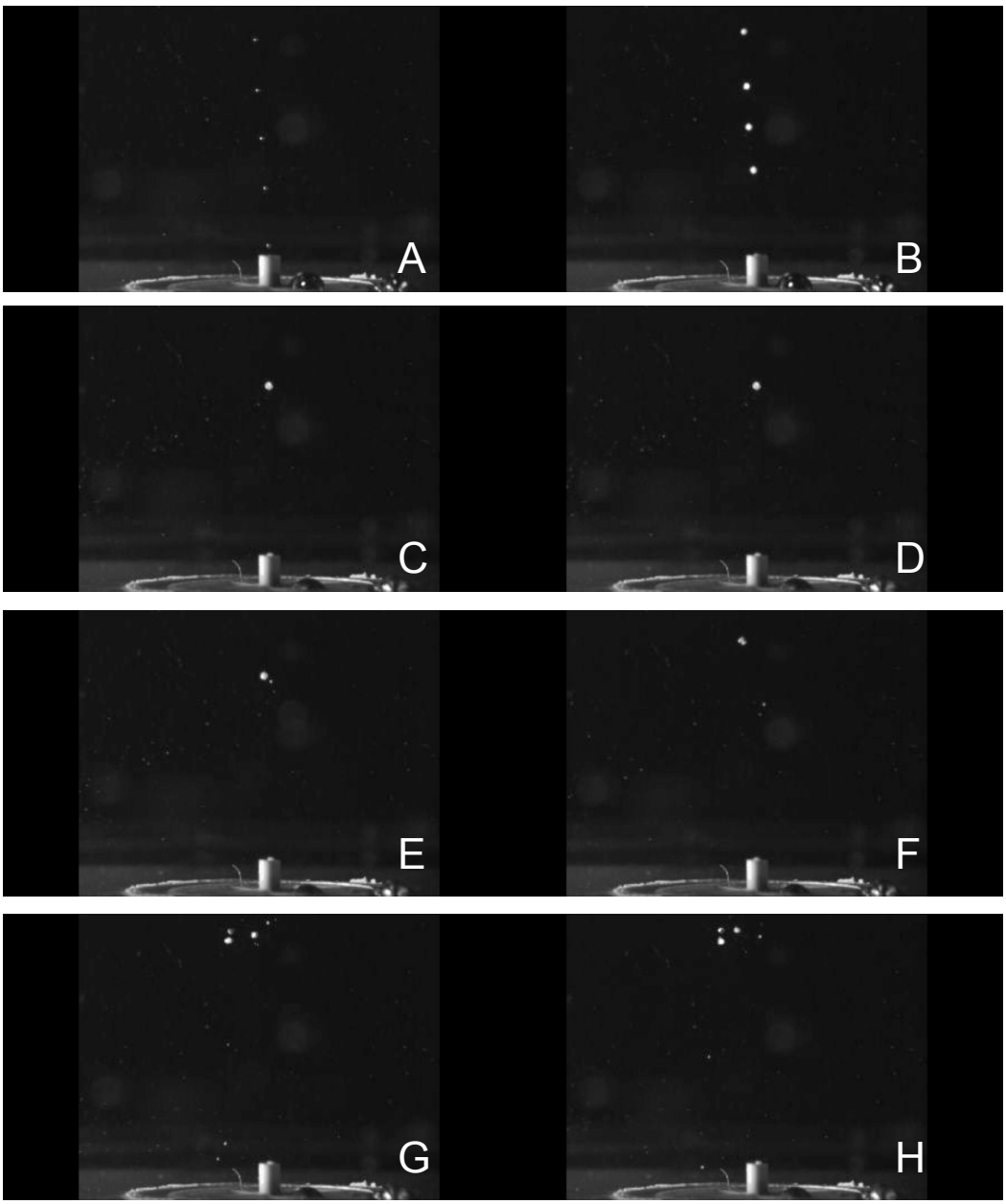

Figure 3.3: The 12.7 *mm* (1/2 *in*) horn is placed 1 wavelength (74 *mm*) above the bottom of the test section. Frame A shows 4 bubbles before pulsing. Frame B shows the start of the pulse. Frame C shows the bottom three bubbles combine due to acoustic forces and continues to grow through frames F. Frames G and H show bubbles hovering, breaking apart, and re-coalescing.

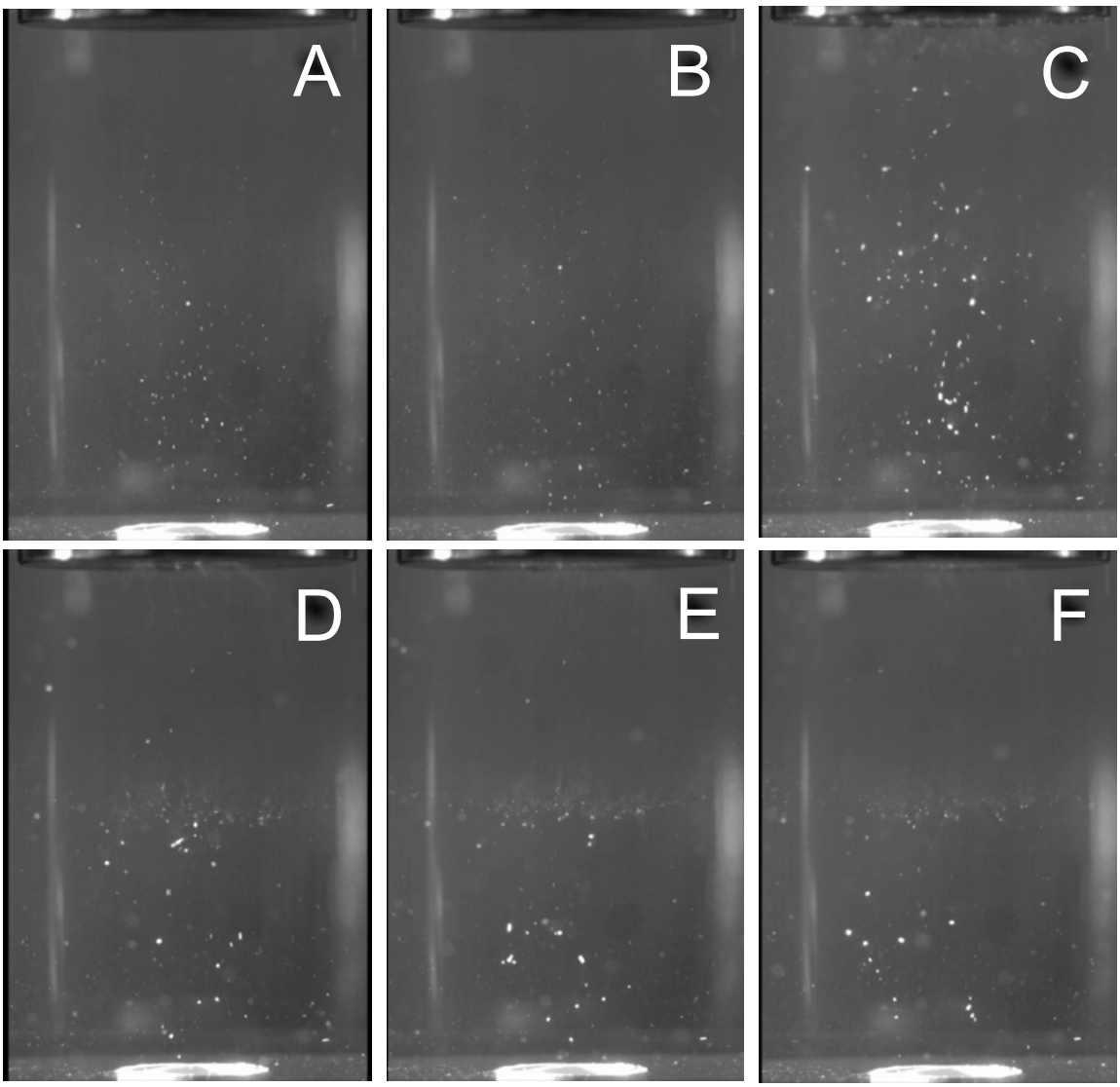

Figure 3.4: The 47.6 *mm* (1.875 *in*) horn is situated 1 wavelength (74 *mm*) above the bottom of the test section with bubbly flow being pumped up towards the horn. Frame A and B show bubbly flow before the ultrasonic pulse. Frame C shows the start of the pulse. Frame D through F show the streaming region under the horn to half the wavelength. At half the wavelength, there is a node where small bubbles congregate. At 3/4 wavelength, there is an anti-node where bubbles oscillate around.

The next logical step would be to apply ultrasonics to an increase flow rate from the bubble resonance experiment and examine the effect of the gas sparging and ultrasonics have on the dissolved gas concentration. The observations from this experiment have informed the next iteration of the experiment. It is apparent that bubbles will avoid the near-field, where the ultrasonics would have the strongest effect for enhancing mass transfer. In the next iteration, this was addressed by forcing the bubbles into the near-field and pulsing the drive to the ultrasonic horn to ensure that bubbles are inside the near-field.

3.1.2 Flowing Fluid Studies

The flowing fluid study was designed to gain insight into the relationships between ultrasonic energy, two-phase flow, and DO concentration. This experiment was designed to have a significant increase in pumping power and fluid volume. The loop consisted of a venturi bubble injector, ultrasonic test section, cyclone separator, variable frequency pump, cooler, thermocouples, and dissolved oxygen (DO) probe, as shown in Figure 3.5. The concern of not being able to get bubbles into the near-field of ultrasonics was addressed by putting the horn into the inlet piping, where the horn covers most of the pipe area, as shown in Figure 3.6.

The operation of this loop was to first cool the fluid to $5°C$ in order to saturate the water with as much oxygen as possible, then strip the DO with an inert gas, Ar. The liquid flow rate range of the experiment was 18.9 LPM to 26.5 LPM (5 GPM to 7 GPM), and the gas injection rate was 0.24 LPM (0.5 $SFCM$). The experiment did not produce the desired effects. While watching the bubble flow interact with the ultrasonic near-field, it was apparent that the bubbles were not being pushed into the near-field. Figure 3.7 shows the preferred flow path of bubbles, which bypasses the near-field. The horn that was used was the 47.6 mm diameter horn. The estimated

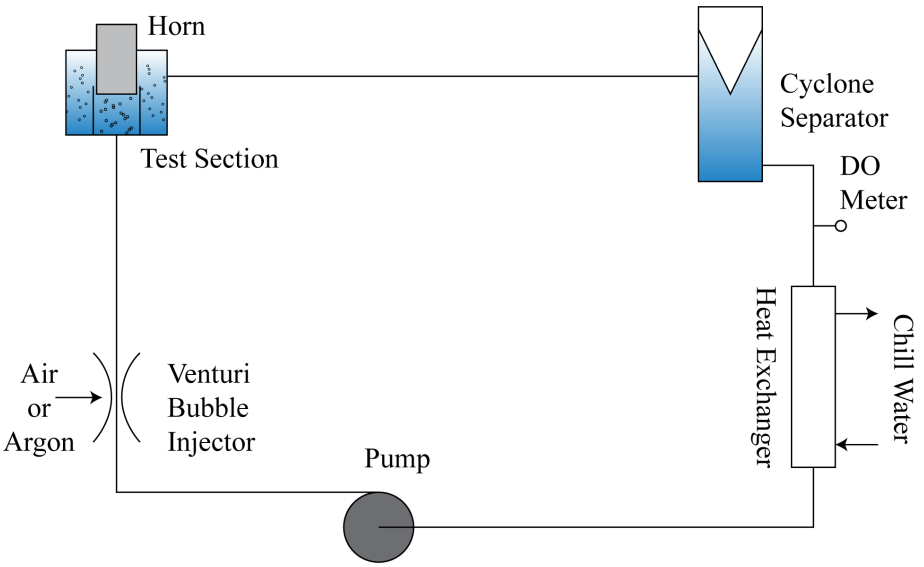

Figure 3.5: Schematic of the Flowing Fluid Study loop.

Figure 3.6: Flowing fluid study test section with no bubbles. It is possible to see how the flow must pass by the ultrasonic horn and how small the flow cross section is past the horn

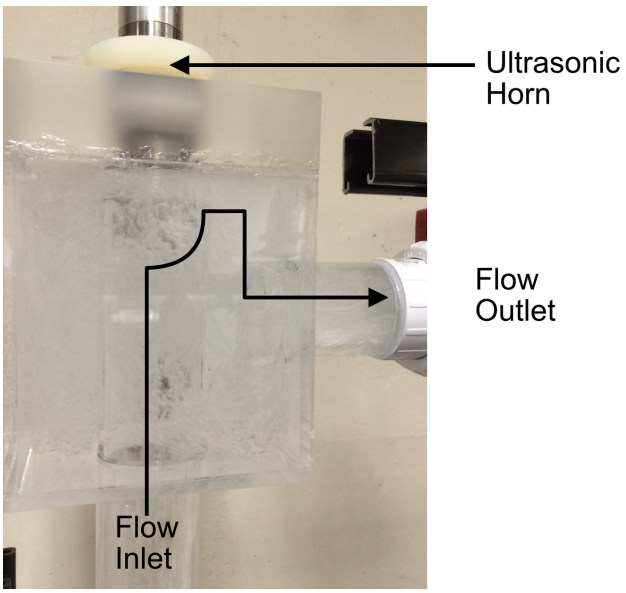

Figure 3.7: Rev 2 with bubbly flow. Flow direction is highlighted.

intensity of this horn was 0.085 W/cm^2 which is defined as the power supplied to the horn from the drive divided by the area of the horn face. The results from this experiment is shown in Figure 3.8. All runs comparing the DO vs time with and without ultrasonics overlapped within the error of the DO meter (0.4 mg/ml).

Although these results were not the desired outcomes, these observations were key to the design of next iteration of this study. It was observed that bubbles would not enter the ultrasonic near-field. Due to the higher flow rates, the convective contribution to mass transfer would have been so large that any contribution of ultrasonics were being masked. These conclusions pointed to the need for a smaller experiment that would minimize the contribution of convective mass transfer and isolate the contribution of sonomechanically enhanced mass transfer.

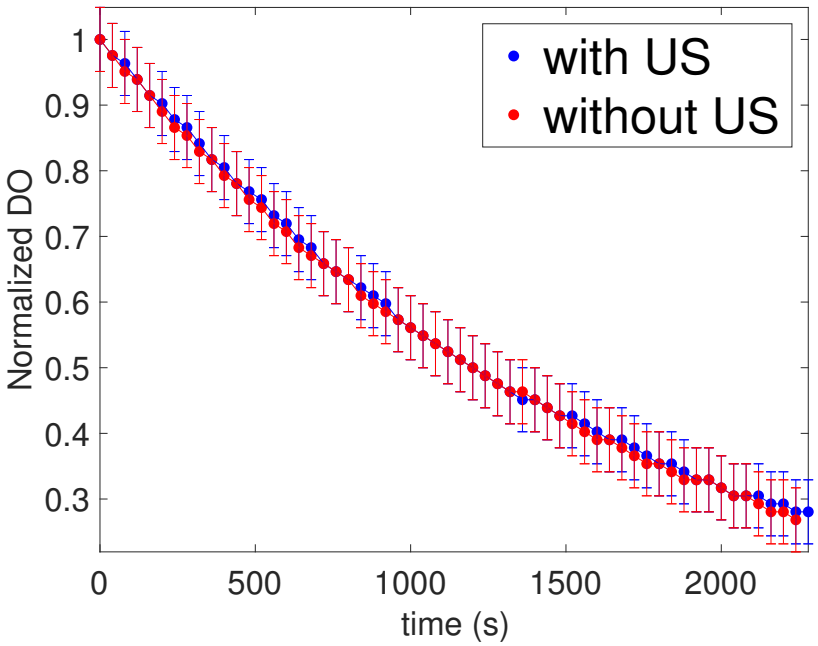

Figure 3.8: Typical results from the flowing fluid study. The control and ultrasonic runs overlap consistently.

3.2 Experimental Setup

The iteration following flowing fluid study was the Small Ultrasonic Mass Transfer (SUMATRA) experiment. This design iteration leveraged the insights of the observations so far. Namely, maximize the contribution of convective mass transfer, use a small and easy to modify bench top test platform, and to use pulsing low power ultrasonics to enhance stripping gas.

The configuration of the SUMATRA loop was similar to the flowing fluid studies loop. The flow loop consisted of a pump, capillary tubes for bubble injection, thermocouples, a DO sensor, cyclone separator, a heat exchanger, and a flow meter. It also operated by cooling and oxygen saturating the fluid, then strip the DO with and

without ultrasonics. A schematic of the experiment reflecting both the low intensity and high intensity experiments is shown in Figure 3.9a and 3.10b, respectively.

As noted earlier, there were two test sections constructed. The first test section was a low intensity cell modeled after the flowing fluid study test section where the large horn was used and the bubbly flow was directed into the face of the horn, Figure 3.9b. The second test section was a high intensity cell constructed with delrin reflectors and the smaller 11.7 *mm* probe. The high intensity test section is shown in Figure 3.10b, and the SUMATRA experiment with the high intensity test section is shown in Figure 3.12. The hold up for the SUMATRA experiment was 1.1 %, which places vertical bubbly flow in the dispersed bubble regime as illustrated in Figure 3.11.

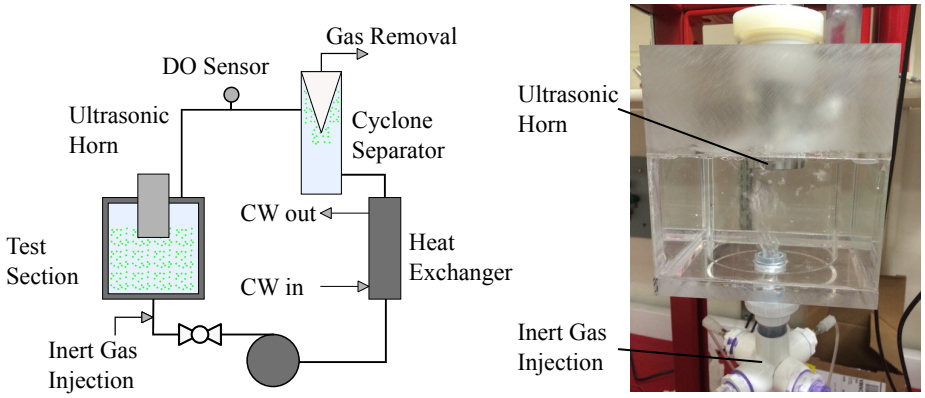

Figure 3.9: a) Schematic of the SUMATRA experiment with low intensity test section. b) SUMATRA test section with low intensity horn (47 *mm* diameter).

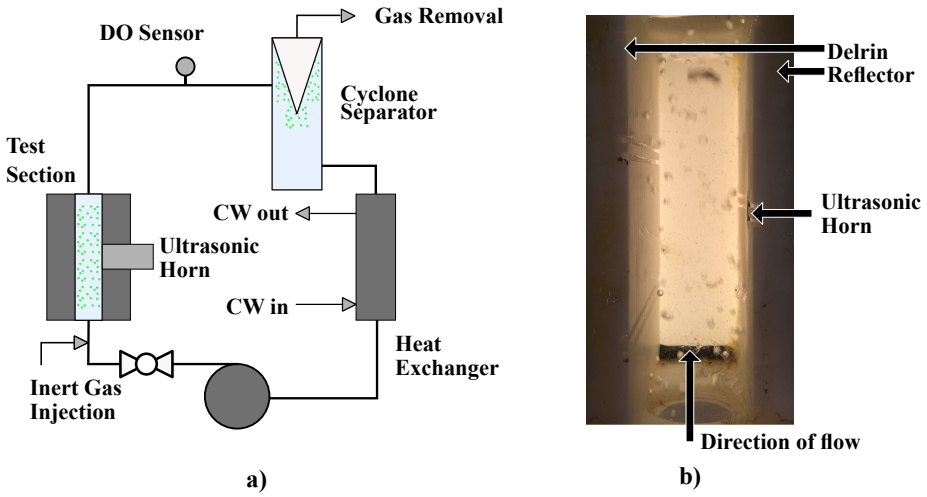

Figure 3.10: a) Schematic of the SUMATRA experiment with high intensity test section. b) SUMATRA test section with high intensity horn (12.7 mm diameter). Dimensions: Height = 116 mm, Width = 28 mm, Depth = 83 mm.

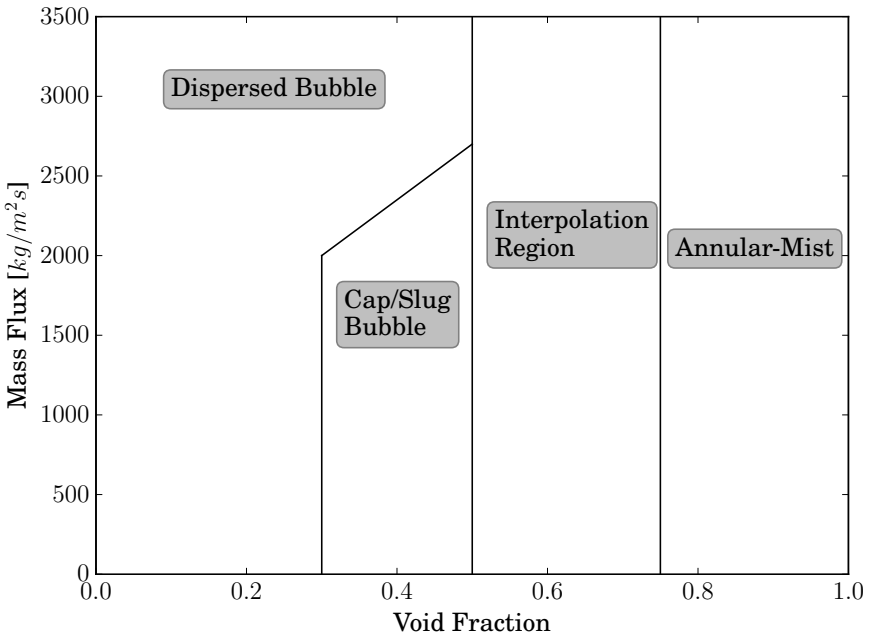

Figure 3.11: Two phase regime map for vertical gas and liquid flow [63].

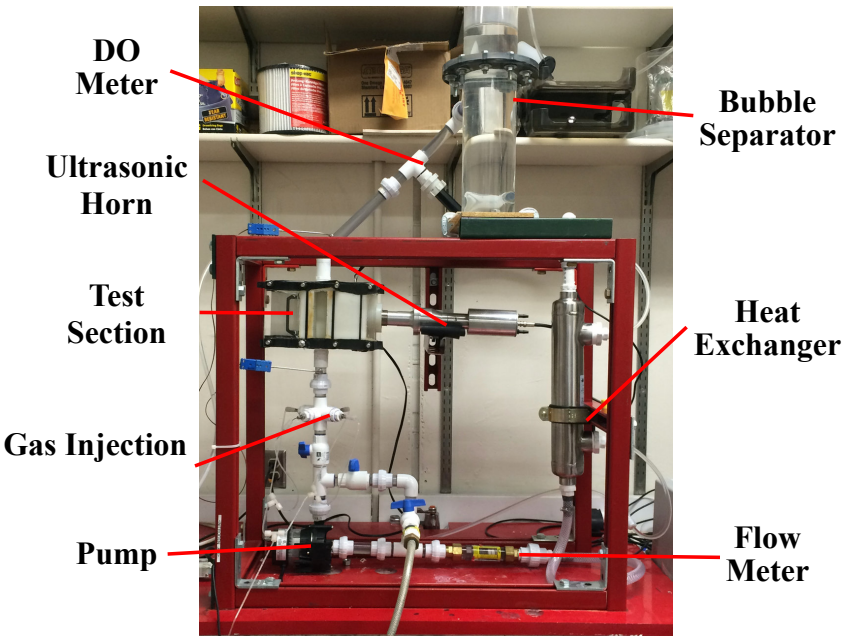

Figure 3.12: SUMATRA experiment with high intensity test section.

3.2.1 Equipment

The ultrasonic horn and amplifier used was a Sonics and Materials VCX-750, which has a nominal operating frequency of 20 kHz. It was equipped with a 4.76 cm (1.875 in) diameter low intensity horn and a 1.27 cm (0.5 in) high intensity horn with attached amplitude booster. The DO meter and probe used was a General Tools probe and meter, which was an electrochemical type dissolved oxygen meter. The bubble injectors were capillary tubes with a teflon coated ID of 25 μm oriented perpendicular to the flow. These capillary tubes were found to be able to produce the smallest bubbles consistency. A high speed camera used to take the visual data, and this was a Fastec IL13043001 model IL3100SM4, which was capable of 500 to 700 fps for the resolutions required by the SUMATRA experiment.

3.2.2 Experimental Procedure

The experimental procedure consisted of saturating the fluid with oxygen and subsequently stripping the DO to achieve a predetermined DO concentration. This process was performed both with and without ultrasonics applied. The fluid was water or a water glycerol mixture designed to encompass the Sc range for FHR flibe temperatures. These concentrations are 0 $wt\%$, 12.5 $wt\%$, 25 $wt\%$, 37.5 $wt\%$, and 50 $wt\%$, and they were adopted from Kress (1972) [20]. The DO and temperature data was measured using the built-in logging feature in the DO meter. The data was then used in the calculation of the volumetric mass transfer coefficient, k_La. The selected start and stop concentrations were related to the DO saturation limit of the fluid. The DO saturation concentration reduces as the glycerol concentration increases. For lower glycerol concentrations the start DO and stop DO concentrations were fixed at 8.0 mg/L and 3.0 mg/L. The DO saturation for 50 $wt\%$ is found to be lower than 8.0 mg/L. In order to accommodate this and to maximize the stripping range,

the concentration range for these runs used the range 5.0 mg/L to 2.0 mg/L. The experiments were first performed with water in order to ensure the results were as desired before expanding the testing to glycerol mixtures.

During the ultrasonic runs, care was taken to minimize the potential contribution of the temperature rise to degasification due to the input of acoustic energy. This was achieved by determining the equilibrium temperature for the ultrasonic runs and then performing control runs at the same temperature. The equilibrium temperatures were observed to be in the range $8°C$ to $12°C$. This equilibrium temperature was then used as the starting temperature for the ultrasonic runs to minimize the effects of temperature variations.

Visual data was taken using the high speed camera during both control and ultrasonic runs. Unfortunately, the camera was limited in frame rate and was unable to resolve the bubble vibrations at 20 kHz. In spite of this limitation the high speed videos were able to be used for bubble counting, bubble size measurement, and to visualize bulk ultrasonic effects. These techniques are explained in more detail in Appendix D.1.

3.2.3 Low Intensity Operation

The intensity at the horn tip of the 47 mm horn was estimated at 0.085 W/cm^2. This estimation was calculated from the power output indication on the VCX-750 driver divided by the area of the horn face. A pre-determined matrix of runs was performed in order to determine the optimal volumetric flow rate. The volumetric flow rate that yielded the best results, in terms of time reduction, was 4.73 LPM (1.25 GPM). The test section fluid velocity and residence time was 4.31 cm/s (1.71 in/s) and 1.66 s, respectively. As noted in the exploratory studies, pulsing was utilized to allow the sparging bubbles into the near-field. The ultrasonic driver

was set to pulse for 1 second on and 1 second off. Data for low ultrasonic intensity showed only a marginal increase in mass transfer, as detailed in Section 3.3.1, tests were only performed using water.

3.2.4 High Intensity Operation

In contrast to the low intensity test, the ultrasonics was able to run continuously. As reported by Jagannathan (2011) [64], bubbles were able to enter the near-field of a high intensity acoustic fields of 300 W/cm^2. This allowed bubbles to be captured in the near-field while ultrasonic energy was being applied. The acoustic intensity at the horn tip was estimated to be 275 W/cm^2 and bubble were observed to enter the near-field. The intensity was calculated from the power indication from the VCX-750 driver over area of the probe face. The flow rate that yielded the best performance was experimentally determined to be 15.14 LPM (4 GPM). The test section fluid velocity and residence time was 4.16 cm/s (10.58 in/s) and 1.09 s, respectively. In contrast to the low intensity test, the performance for high intensity tests in terms of DO stripping was much more pronounced as reported in Section 3.3.2. The DO results show a consistent improvement over a set range of glycerol concentrations. The runs were performed for the scaled concentrations of glycerol, 0%, 12.5%, 25%, 37.5%, and 50% by weight glycerol.

3.3 Results

The results split for the two tests performed on this platform. The low intensity test is presented in Section 3.3.1, and the high intensity test is presented in Section 3.3.2.

3.3.1 Low Intensity Test

The DO stripping results are shown in Figure 3.13. These results are the raw, normalized average data 9 runs, and only demonstrate a marginal increase in performance of an approximately 20% reduction in degassing time. Because, as noted earlier, bubbles could not be pumped into the near field, ultrasonic pulsing was utilized. The visual data that bubbles were in the near field due to the pulsing. The bubbles that were in the near field remained inside the near field and demonstrated a "wicking" behavior. An example of the visual data is shown in Figure 3.14.

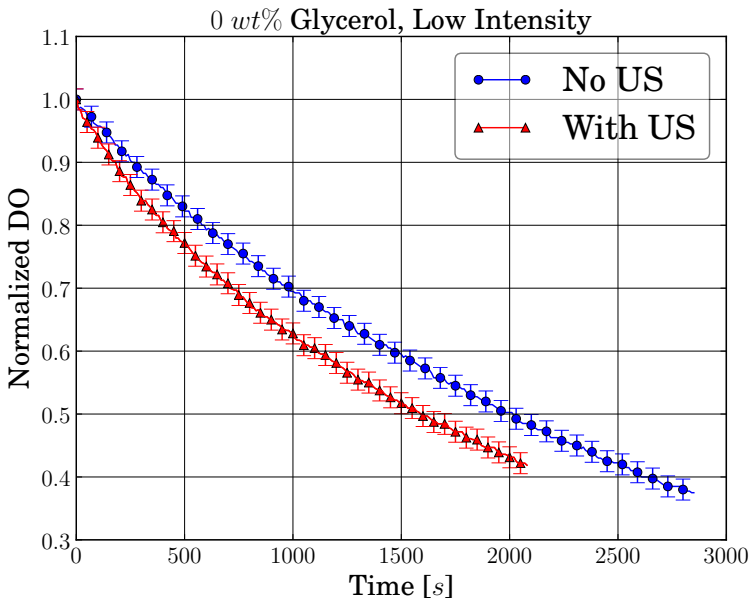

Figure 3.13: Results of the low intensity testing.

3.3.2 High Intensity Test

As mentioned before, these were first performed with water, and because the results were favorable, the experiment was continued with water and glycerol mixtures which

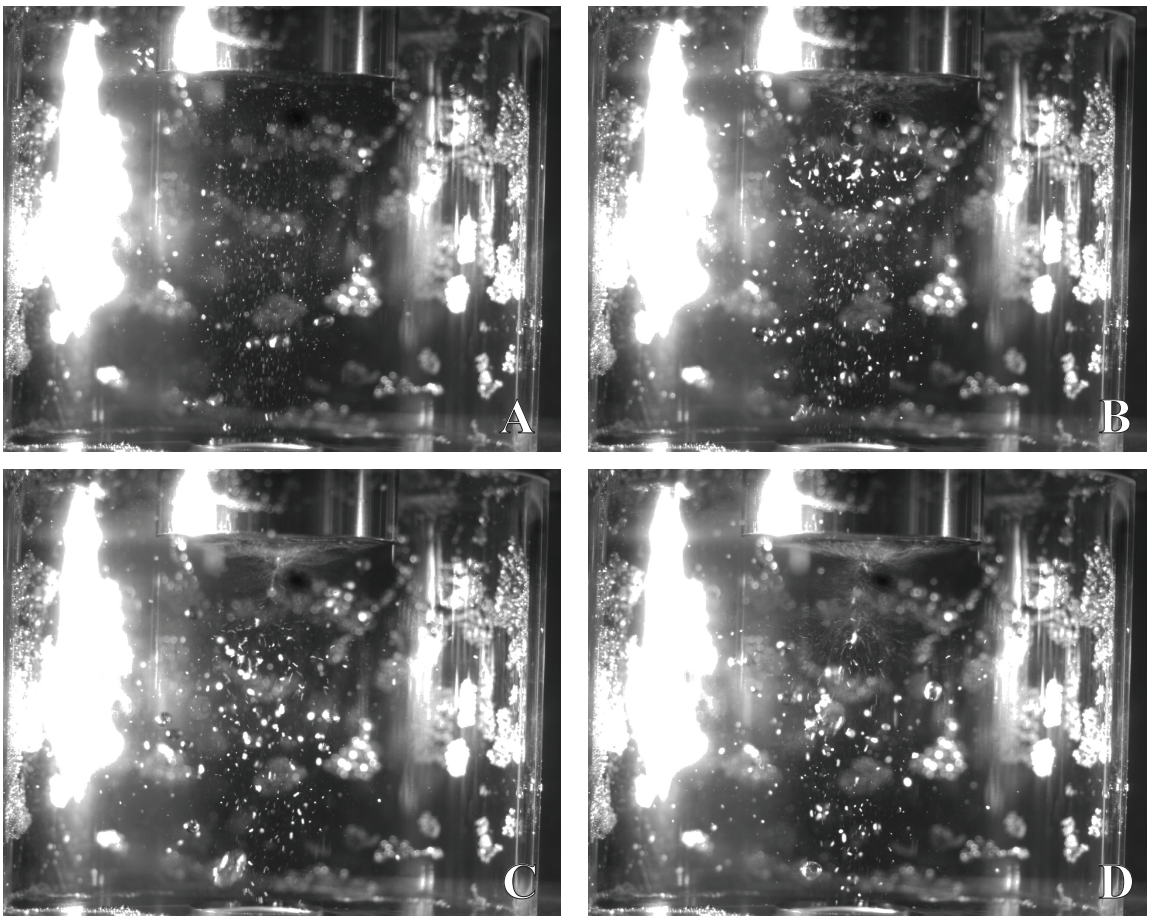

Figure 3.14: Visual results from the low intensity SUMATRA experiment. Frame A shows bubbles in the test section without ultrasonics applied. Frame B shows the instant the ultrasonics pulses on with bubbles trapped into the near field. Frame C shows the beginning of the wicking behavior near the horn face. Frame D shows the lasting structure of the wicking filaments and the attracting of bubbles and gases into the filament.

encompass the Sc of flibe at normal operating temperatures for the FHR. From the normalized DO data from each of the runs, the volumetric mass transfer coefficient, k_La, can be calculated. The basic model of changes in concentration is equation (3.1). The solution for k_La is the slope of equation (3.2). The DO results are shown in Figure 3.15. From these data k_La can be obtained by using equation (3.2), and these data are shown in relation to glycerol concentration in Figure 3.16. To evaluate

of mass transfer performance, the experimental Sh and mass transfer coefficient (k_L) will be determined, and a Sh correlation will be developed. The experimental Sh function is shown in equation (3.3).

$$\frac{dC}{dt} = k_L a(C^* - C) \tag{3.1}$$

$$-\ln\left(\frac{C_1}{C_2}\right) = k_L a(t_2 - t_1) \tag{3.2}$$

$$Sh = \frac{k_L a}{a}\,\frac{D}{\mathscr{D}} \tag{3.3}$$

Visual results show a much different behavior in terms of bubbles interacting with the near-field of the ultrasonics. Figure 3.17 shows an example of the visual data taken for each glycerol concentration without ultrasonics, and Figure 3.18 shows an example of what is seen when ultrasonics is applied. Although it is difficult to see through pictures, the high speed camera footage in Figure 3.18 shows, that bubbles do get swept into the near-field and do not avoid the ultrasonics. Also, the footage shows that the bubbles that do get entrained into the near-field do get broken up into smaller bubbles. Another observation was that was made was there was more circulation and movement compared to the low intensity standing wave design.

In order to calculate the k_L from the $k_L a$, the interfacial area (a) must be determined [35]. Classically, interfacial area is found by using equation (3.4). This was attempted, but due to the equipment limitations in terms of optical resolution, the individual bubble diameters were not able to be directly measured. This attempt to measure bubble diameters directly was performed by using a combination of image

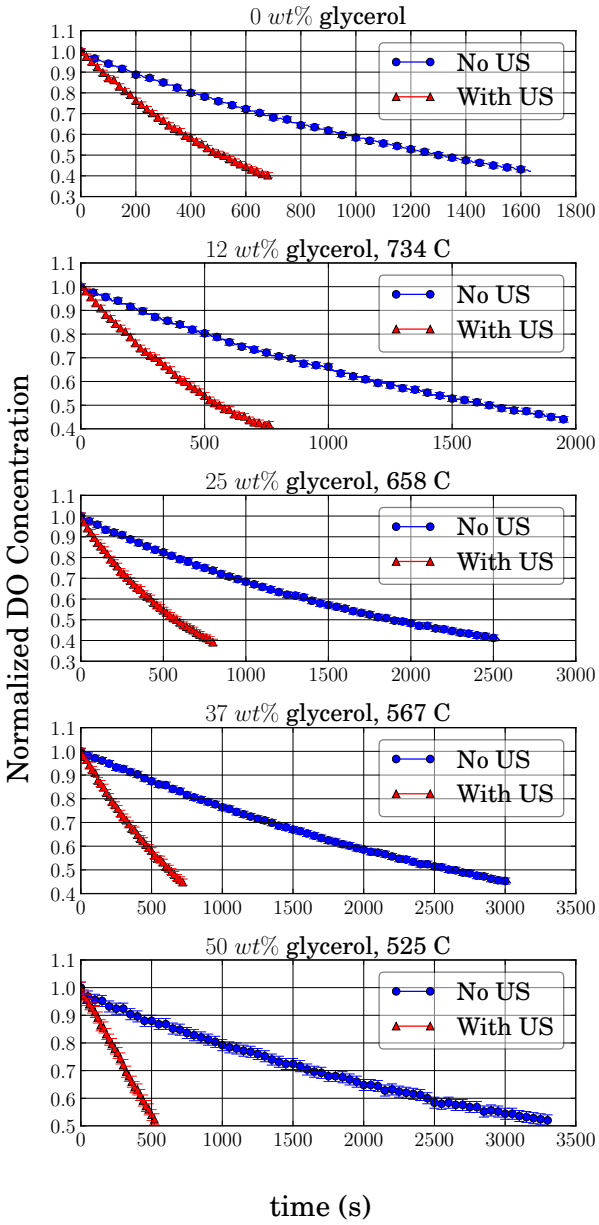

Figure 3.15: DO data for the SUMATRA experiment. Glycerol concentrations are matched with the corresponding flibe temperatures. The 0 $wt\%$ has no corresponding flibe temperature.

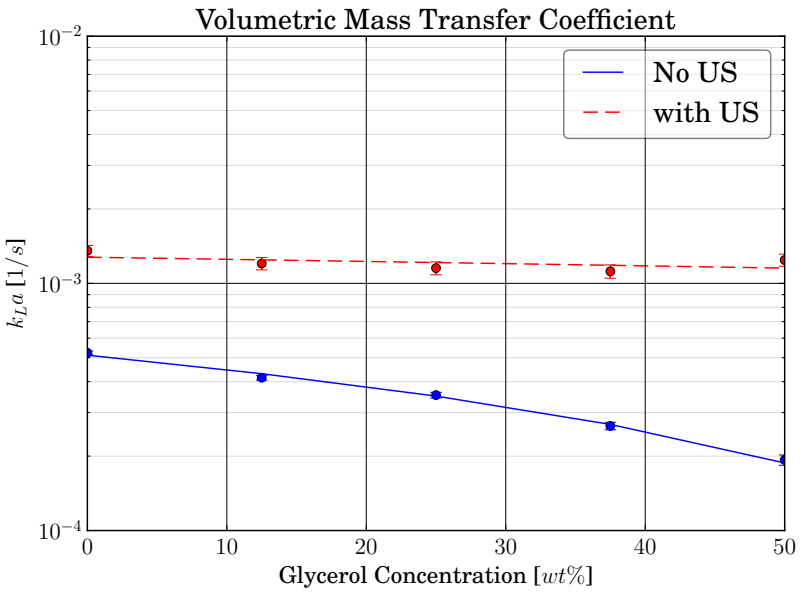

Figure 3.16: Volumetric mass transfer coefficient comparison.

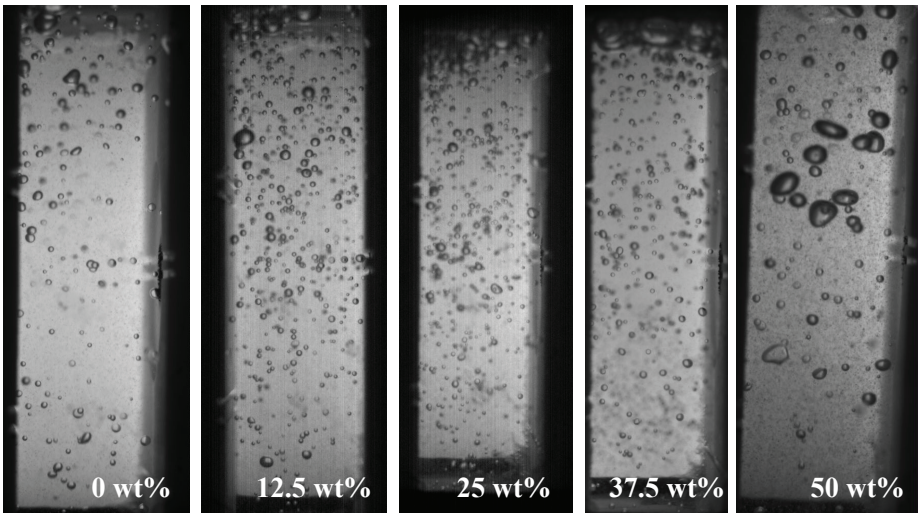

Figure 3.17: SUMATRA high intensity test section with no ultrasonics. This is an example of the visual data used for bubble measurements and counting.

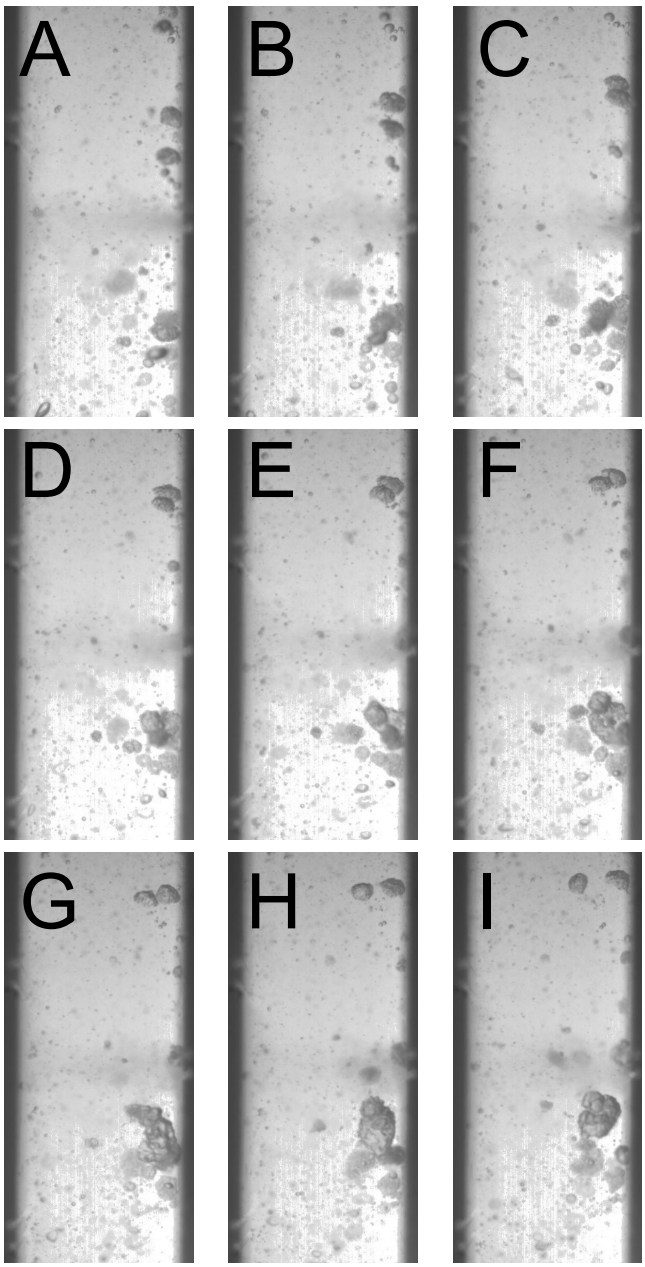

Figure 3.18: SUMATRA high intensity test section during enhanced DO stripping. It shows increased convection and bubble breakup, which was not seen in the low intensity test section for each glycerol concentration.

processing software (Affinity Photo) and imageJ [65]. The analysis of the visual data concluded that the resolution on the high speed camera was not sharp enough to give the bubble sizes accurately. The limit of the visual resolution was on the order of 100 $\mu m/pixel$. Another way of inferring interfacial area was found in the work by Kress [20] where the interfacial area can be determined through the holdup (ε) and the bubble number density (N) as shown in equation (3.5). Although the direct measurement of bubble diameter was impractical, the bubbles were still able to be counted visually, making use of this relationship a viable method to determine interfacial area given the limitations of the laboratory equipment. This method is discussed in more detail in Appendix D. The results of direct diameter measurement and the diameter inference analysis are included in the results of interfacial areas. The average bubble diameters can also be determined by the relationship given in equation (3.6). These data are also included for reference. For the sonomechanically enhanced runs, equation (3.4) can be used to determine interfacial area under the assumption that the resonance radius is the average bubble diameter. In this case, the resonance radius [40, 61] is calculated using equation (3.7). The interfacial areas can be compared and these data are given in Figure 3.20. This shows that the measured ultrasonic interfacial area and the expected interfacial area agree within an order of magnitude.

$$a_{classic} = \frac{6\varepsilon}{d_{avg}} \tag{3.4}$$

$$a_{inferred} = \frac{3}{2}\left(\frac{6\pi}{4}\right)^{2/3} N^{1/3}\varepsilon^{2/3} \tag{3.5}$$

$$d_{avg} = 2\sqrt{\frac{\sigma}{g\Delta\rho}} \tag{3.6}$$

$$d_{res} = \frac{1}{\pi f}\sqrt{\frac{3\kappa p_0}{\rho}} \tag{3.7}$$

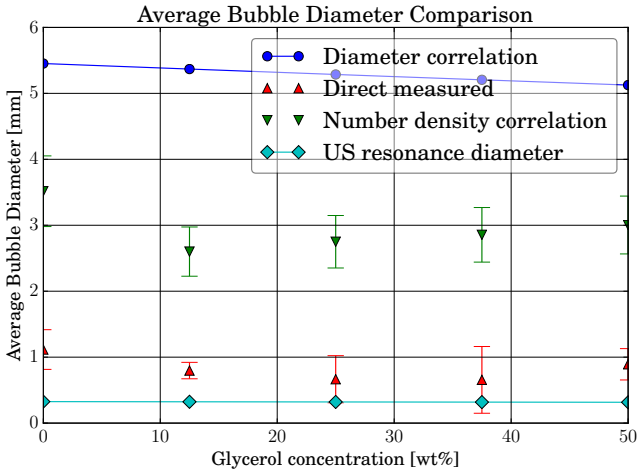

Figure 3.19: Comparison between correlated, directly measured, inferred, and ultrasonic resonance diameters

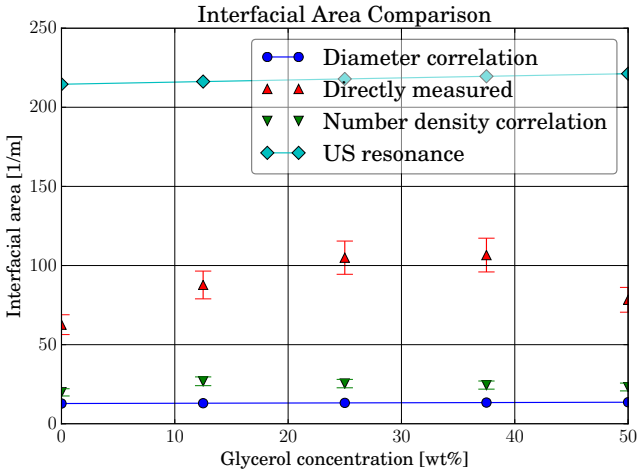

Figure 3.20: Comparison of correlated, directly measured, inferred, and ultrasonic interfacial areas

The experimentally determined Sh numbers are shown and compared with to the established correlation reported in the literature and the data are given in Figures 3.21 and 3.22. The experimental k_L results are shown in Figures 3.23 and 3.24. The results suggest that the lower the Sh, the better the performance. This was counter to the initial hypothesis because the introduction of ultrasonics was expected to increase the convective mass transfer component. The comparison with the experimental data and the established correlation from equation (2.21), shows a closeness in the form of the relationship and it would appear that the correlation can be scaled to match the SUMATRA experimental conditions.

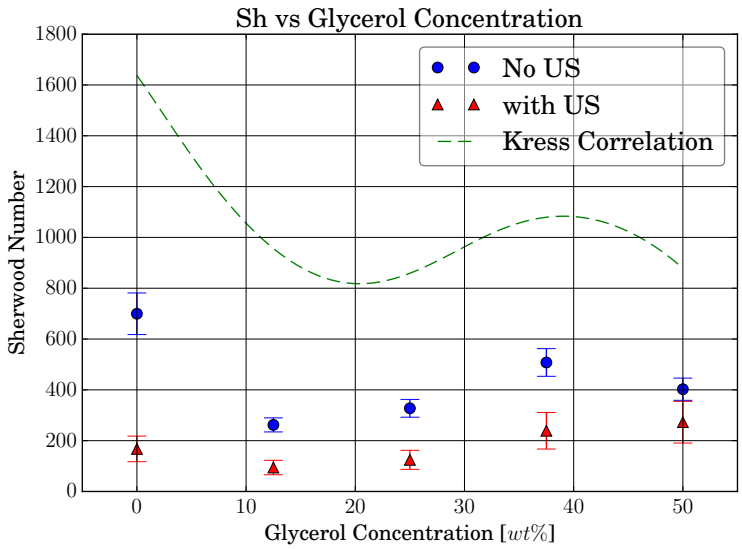

Figure 3.21: Sherwood number comparison to equation (2.21) correlation.

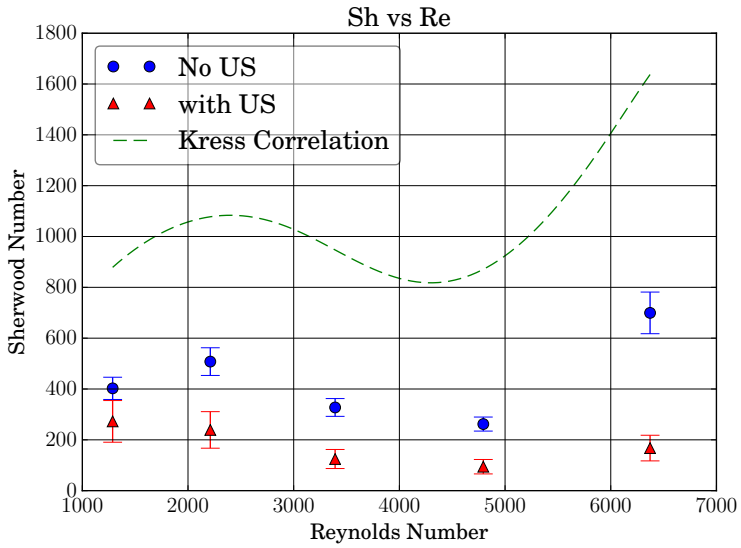

Figure 3.22: Sherwood number comparison to equation (2.21) correlation.

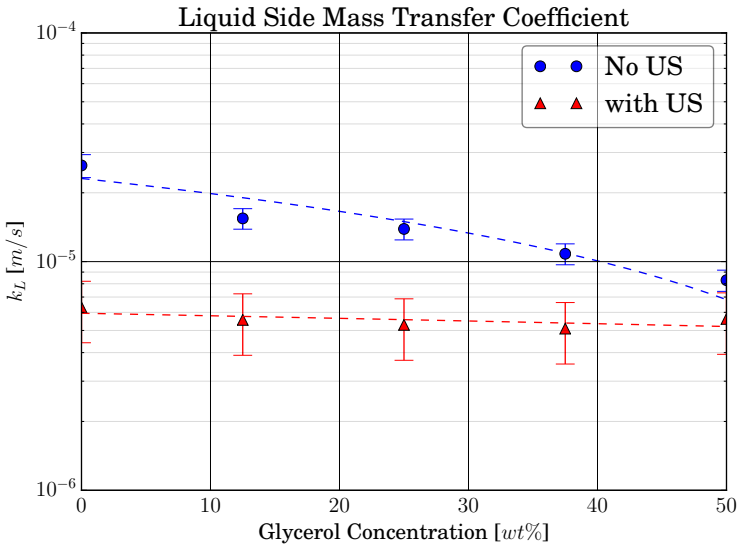

]

Figure 3.23: Liquid side mass transfer coefficient vs glycerol concentration.

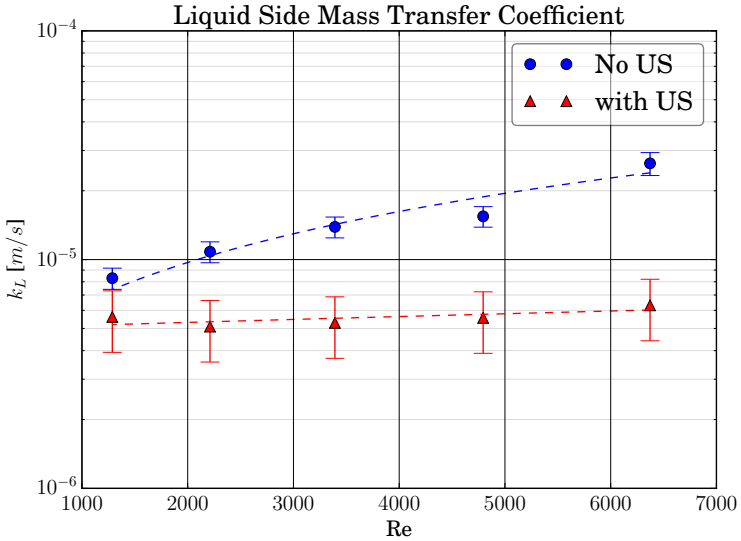

Figure 3.24: Liquid side mass transfer coefficient vs Re number.

In Perry's Engineer's handbook [66], the Sh correlation for sparging concurrent to flow is in the form of equation (3.8), and the constants and exponents were previously found to be (2.21). In order to fit the correlation to the SUMATRA data, a least squares optimization was performed using the leading coefficient (C) and Re exponent (x) as variables. This yielded equation (3.9). In an attempt to predict the Sh for ultrasonic enhancement to a first approximation, the resonance diameter was used in equation (3.9). This result gives a measure of the predicted ultrasonic enhancement. These results are shown in Figures 3.25 and 3.26. Looking at the ultrasonic predicted results do not accurately follow the experimental data. This suggests that an acoustic term must be developed to capture the ultrasonic contribution.

$$Sh = C\ Re^{x} Sc^{y} \left(\frac{d}{D}\right)^{z} \tag{3.8}$$

$$Sh = 0.28\ Re^{0.86} Sc^{1/2} \left(\frac{d}{D}\right)^{1.0} \tag{3.9}$$

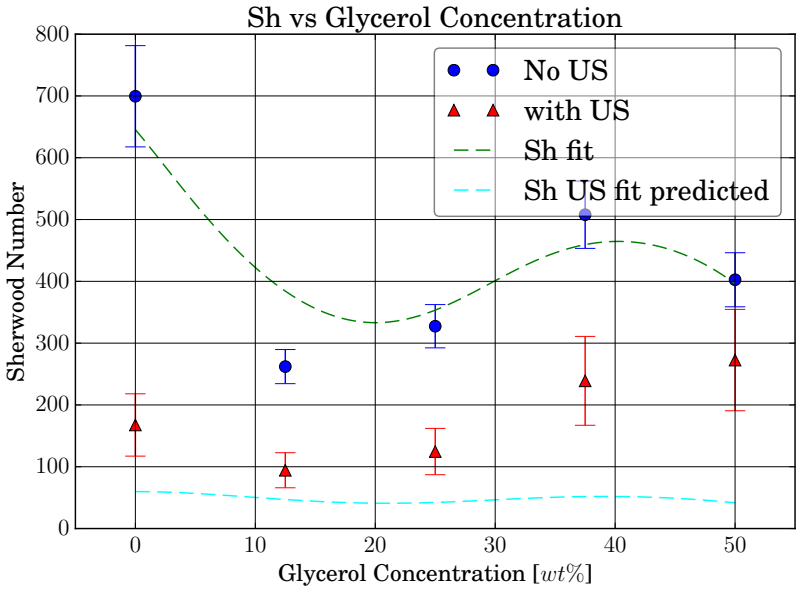

Figure 3.25: Sherwood number vs glycerol concentration

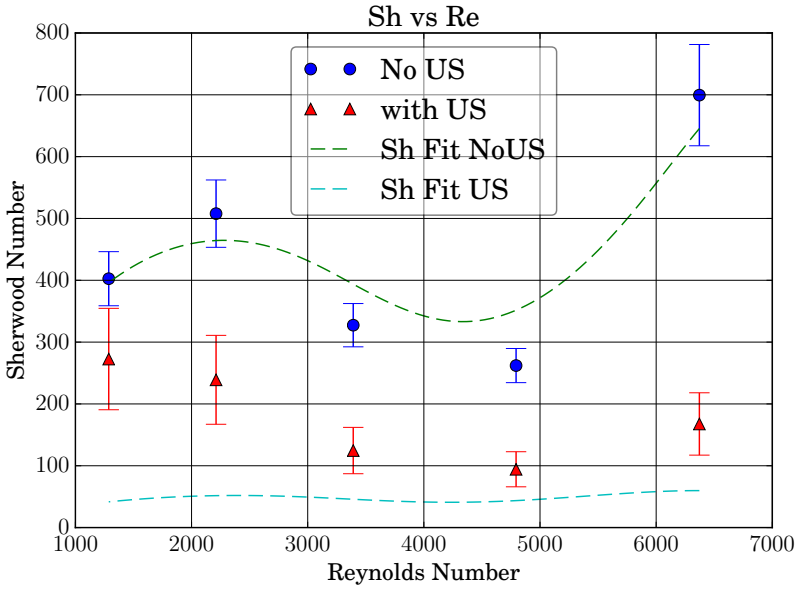

Figure 3.26: Sherwood number vs Re number

3.4 Acoustic Correlation

The construction of the ultrasonic portion of the Sh correlation utilized the Buckingham Pi theorem. The first step was to identify important acoustic parameters that would have an effect on the mass transfer. These parameters are listed in Table 3.1. These terms were selected because of its importance to the acoustic interaction. Intensity was selected because of the direct relation of energy to the mass transfer

Table 3.1: Selected Acoustic Parameters

Parameter	Term	Units
Intensity applied	I	W/m^2
Frequency	f	Hz
Horn acoustic impedance	Z_1	$Pa\ s/m^3$
Liquid acoustic impedance	Z_2	$Pa\ s/m^3$
Residence time in ultrasonic volume	τ	s
Number density of bubbles	N	$1/m^3$

enhancement. Specifically applied intensity was chosen because this parameter is known. Horn impedances were selected to take into account the transmission phenomenology. The residence time takes into account the interaction time. Finally, the number density and frequency take into account the physical dimensions of the bubbles in the two-phase flow. Also, the presence of the bubbly flow will add some additional acoustic impedance, which can be superficially captured. The dimensional analysis of these parameters yields the following Pi terms in equations (3.10), (3.11), and (3.12).

$$\Pi_1 = \frac{\tau\ I^{1/2}\ N^{1/3}}{Z_2^{1/2}} \tag{3.10}$$

$$\Pi_2 = \frac{Z_1}{Z_2} \tag{3.11}$$

$$\Pi_3 = \frac{f\ Z_2^{1/2}}{I^{1/2}\ N^{1/3}} \tag{3.12}$$

The Π_1 term was selected as a function of Π_2 and Π_3, shown in equation (3.13). The acoustic term was shown as the relation in equation (3.14). This would finally yield a correlation in the form shown in (3.15).

$$\Pi_1 = \Phi(\Pi_2, \Pi_3) \tag{3.13}$$

$$\frac{f}{I^{1/2}\ N^{1/3}} \frac{Z_1}{Z_2^{1/2}} \tag{3.14}$$

$$Sh = C\ Re^w Sc^x \left(\frac{d}{D}\right)^y \left(\frac{f}{I^{1/2}\ N^{1/3}} \frac{Z_1}{Z_2^{1/2}}\right)^z \tag{3.15}$$

The leading coefficient and the exponents for Re and the acoustic term was derived for this correlation by using the least squares optimization method with the experimental data. A sensitivity study was performed on the exponents of Sc and bubble-to-duct diameter ratio, and this study confirmed that 0.5 and 1, respectively were the appropriate values.

$$Sh = 1.62 \times 10^{-6}\ Re^{0.31} Sc^{0.5} \left(\frac{d}{D}\right)^1 \left(\frac{f}{I^{1/2}\ N^{1/3}} \frac{Z_1}{Z_2^{1/2}}\right)^{1.47} \tag{3.16}$$

The correlation fits the experimental data well within the experimental error as seen in Figure 3.27. In order to test the mechanistic performance a sensitivity study was performed by perturbing the key acoustic parameters. The parameters perturbed were frequency, intensity, and acoustic impedance ratio. This study is reported in the following section.

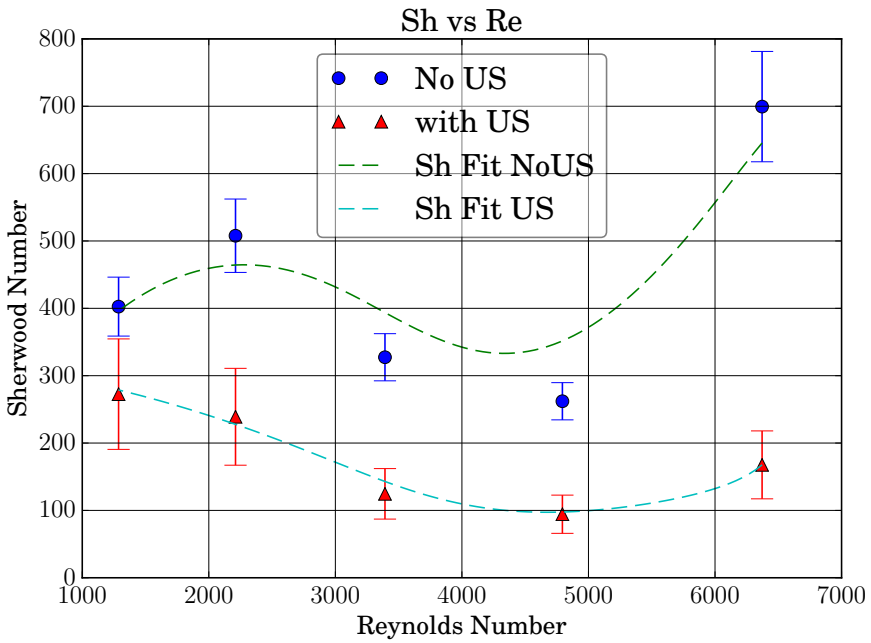

Figure 3.27: Experimental *Sh* for both ultrasonic and non-ultrasonic SUMATRA conditions with the developed ultrasonic and non-ultrasonic correlations.

3.5 Sensitivity Studies

A sensitivity study was performed on the developed acoustic *Sh* correlation, equation (3.16). This was tested in two sets of parameters, fluid and acoustic. The fluid parameter study, shown in Figure 3.28, shows that the average bubble diameter and the hydraulic diameter are the most sensitive, and the Sc and Re are less sensitive. Note the bubble density was not used in the calculation of the average bubble diameter. The average bubble diameter is a function of frequency and ambient pressure and assumed to be the resonant diameter of the applied ultrasonic field, which are ultimately acoustic parameters.

The acoustic parameter study is shown in Figure 3.29. Physically, the perturbations of the parameters behave as expected. The Sherwood number value decreases

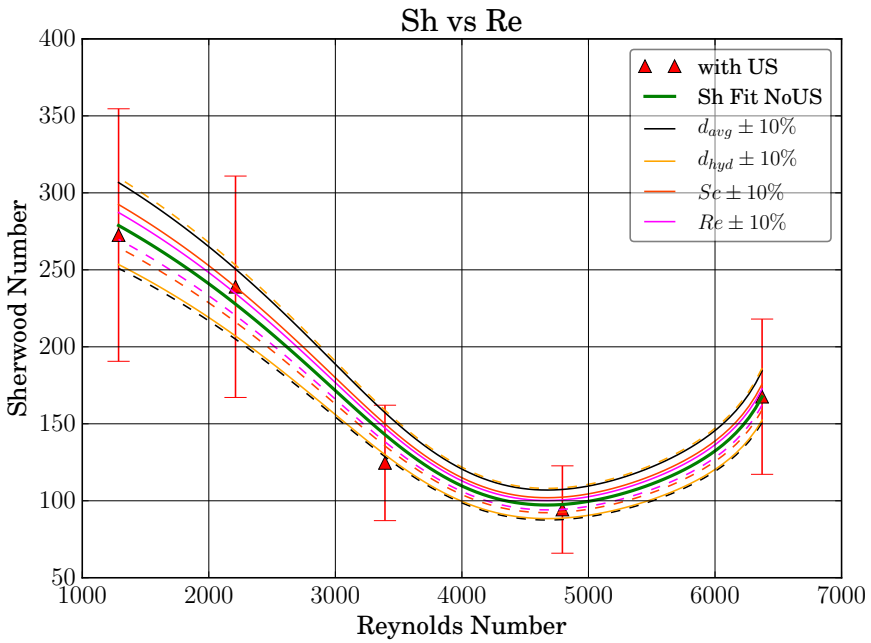

Figure 3.28: Sensitivity study of the fluid properties effects on the ultrasonic correlation. Solid lines correspond to +10% and dashed lines correspond to −10%.

due to an intensity increase. A higher intensity was shown to promote higher mass transfer through the diffusive process. The variance in acoustic area was calculated by assuming the standard intensity was 275 W/cm^2 with a horn face area of 1.26 cm^2, and the face area was varied by ±10% with the same power input. The effect on Sh is an inversely proportional relationship. The atmospheric pressure (p_0) affects Sh proportionally though the ambient pressure relationship to the resonance diameter shown in equation (3.7), which is assumed to be the average bubble diameter. Conversely, the frequency inversely effects Sh through the same relation. The number density effects Sh inversely proportional, as anticipated, by increasing the interfacial area.

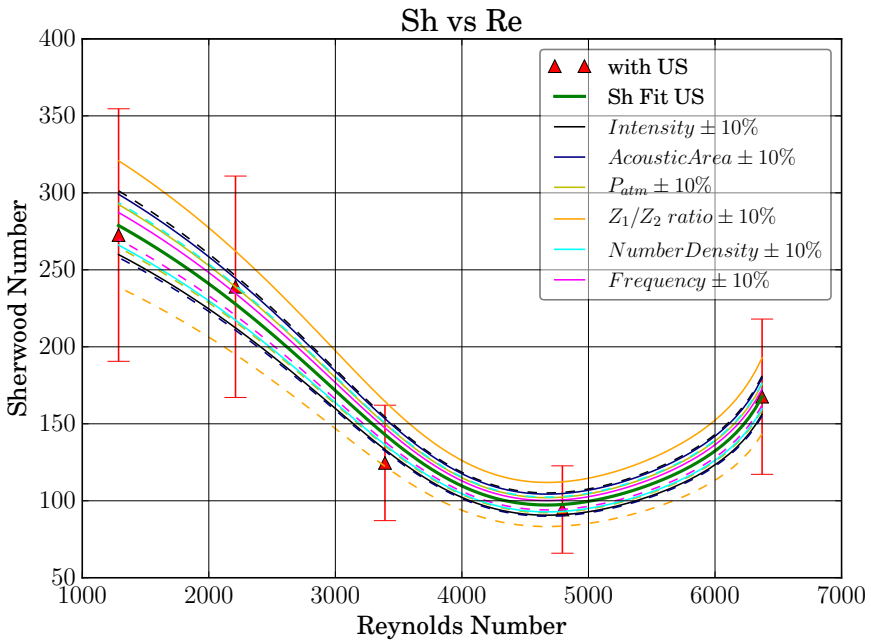

Figure 3.29: Sensitivity study of the acoustic properties on the ultrasonic correlation. Solid lines correspond to +10% and dashed lines correspond to −10%.

3.5.1 Limitation of the Ultrasonic Correlation

To further look into the performance of this correlation, the impedance ratio was tested with an impedance layer. The ideal acoustic impedance matching for the maximum transmission of acoustic energy at an interface between the two media is shown in equation (2.46).

A matching layer was modeled in the correlation and evaluated by the expected response. Ideally, the addition of a matching layer will increase mass transfer by transmitting the maximum acoustic energy, lowering Sh. This study is shown in Figure 3.30. The figure shows that introducing an impedance matching layer, Sh decreases which corresponds to the enhanced mass transfer performance, as expected. As the matching layer impedance value is increased, Sh continues to decrease. This

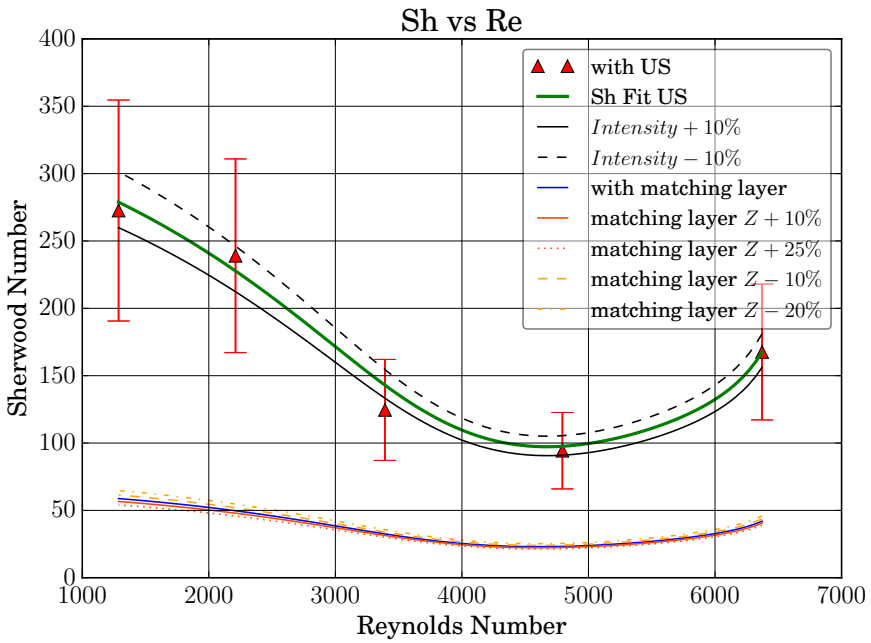

Figure 3.30: Acoustic Correlation with a modeled matching layer.

result is not physical because the matching layer should provide the largest mass transfer enhancement, and therefore shows an impedance ratio limit with respect to the ideal matching layer.

The acoustic correlation, shown in equation (3.16), shows an agreement with the experimental data from the SUMATRA experiment. The sensitivity study performed on the correlation identifies the most and least sensitive parameters and the anticipated effect on Sh with respect to a positive and negative perturbation. The limitation of the developed correlation is the impedance ratio that corresponds to the matching layer impedance.

3.6 Discussion

Using the same Sh correlation form, a new correlation was developed based on an empirical fit. With this correlation, equation (3.9), a first prediction of the ultrasonic Sh relationship was made. This predicted a lower Sh than that which was experimentally determined. This indicates, as expected, that the current model in the literature does not completely account for the effects of the addition of the ultrasonics on the mass transfer mechanism. Also, the experimental conditions for the higher glycerol concentrations (37.5 $wt\%$ and 50 $wt\%$) were in a transition flow regime between turbulent and laminar. Although being in a transition Re regime is not optimal for using a correlation to predict a Sh, although this was by design. By keeping the volumetric flow rate as low as possible, this would also minimize the effect of turbulence on mass transfer and accentuate the contribution of the sonomechanical enhancement.

It was expected that the ultrasonic Sh would be larger, indicating an increase in the convective component of mass transfer. However, according to k_L results, it suggests that the diffusive forces dominate Sh, but to a lesser extent in the control runs. The major factor in lowering the ultrasonic Sh is the size of the sparging bubbles. They were more uniformly smaller when compared to those in the control runs. This would drive the value of the k_L down because the interfacial area was much larger during the ultrasonic runs. This mechanism would suggest that the sparging bubbles were broken up into many smaller bubbles which would be expected to become saturated more quickly.

The equipment deficiencies that were identified with this work were mostly those due to the photography frame rate limits for the necessary resolution and the effectiveness of bubble removal. In order to capture good quality visual footage for analysis, more uniformly intense and diffuse lighting, higher optical magnification,

and a higher frame rate camera are necessary. The recorded optical images were limited to approximately 500 fps, which is lower than that necessary to resolve ultrasonic movement at 20 kHz. The bubble removal at high glycerol concentrations was not complete because bubbles tended to be smaller and more difficult to remove. The cyclone separator used was found to allow for some bubbles to get through. This issue can be addressed in future experiments by using different and more efficient bubble separation technique.

3.7 Conclusion

This experiment demonstrated the proof-of-concept that high power ultrasonics can sonomechanically enhance sparging mass transfer over a range of Sc that encompass the operation temperatures of the FHR. However, there are some challenges that should be addressed while in the scaled experiment level of this investigation. Due to the high intensity of the ultrasonics, excessive wear occurred on the horn tip. The supplied horn from Sonics and Materials was a titanium alloy (Ti-6Al-4V). To illustrate this, Figure 3.31 shows a comparison of a new horn and the horn used in the SUMATRA experiment. With the erosion of such a hard alloy, alternative techniques of imparting ultrasonic energy was investigated in the following experiment. Also, this experiment only investigated the mass transfer phenomena in one dimension, through glycerol concentration. In the next experiment, the investigation will include Re variations with glycerol concentration variations.

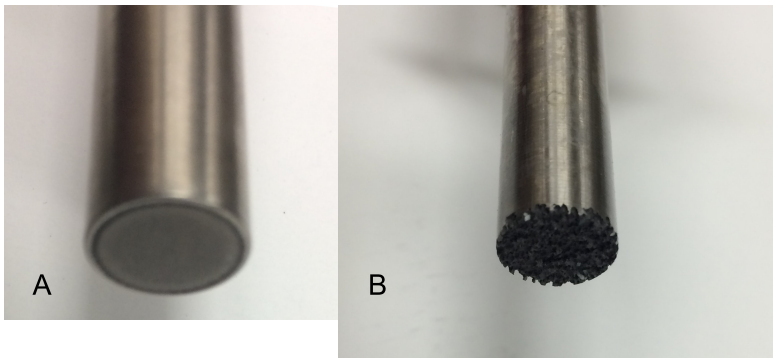

Figure 3.31: Comparison ultrasonic horn tips. Tip A was only used in low power applications and is relatively pristine. Tip B was used for the high power SUMATRA experiments and is very visibly eroded.

Chapter 4

PULST Experiment

The Prototype Ultrasonic Mass Transfer (PULST) Experiment was designed to be a scaled-up version of the SUMATRA experiment which would investigate techniques that would make sonomechanical enhancement of sparging an attractive option to manage tritium removal from FHR salt. The main objective of this experiment was to address the horn erosion that SUMATRA had demonstrated. The key question that this experiment was designed to answer was: is it viable to use indirect sonication with a lower applied acoustic intensities to increase sparging mass transfer? Other considerations that would be explored are the scale up effects from a bench top experiment to a larger facility and the variation of test section geometry.

This iteration of the sonomechanically enhanced mass transfer experiment utilized the basic SUMATRA loop configuration and the continuous application of ultrasonics for the ultrasonic runs. The things that were improved upon are the bubble separation method, flow control, manually tuned ultrasonic generator, a relatively large portion of pipe length to allow for modularity of test sections, and an significantly increased liquid volume.

4.1 Test Equipment

The notional diagram PULST loop is shown in Figure 4.1 and the loop is shown in Figure 4.2. It is of similar design as the SUMATRA loop and is constructed using clear and white 1″ schedule 40 PVC. The operation, similar to the SUMATRA loop, was to saturate the volume with oxygen and subsequently strip the DO with argon with and without sonomechanical enhancement. The individual components employed to achieve this is discussed in more detail in the following sections.

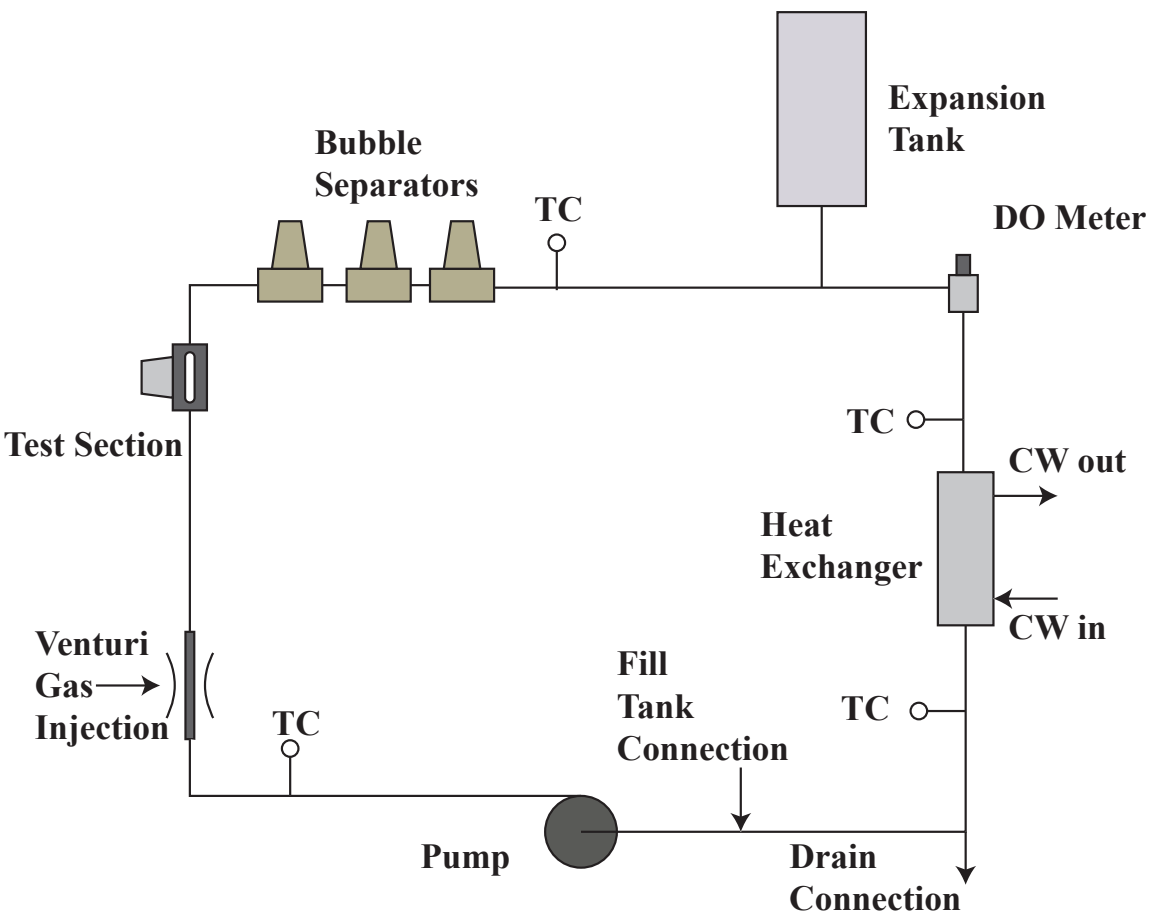

Figure 4.1: PULST Loop Schematic.

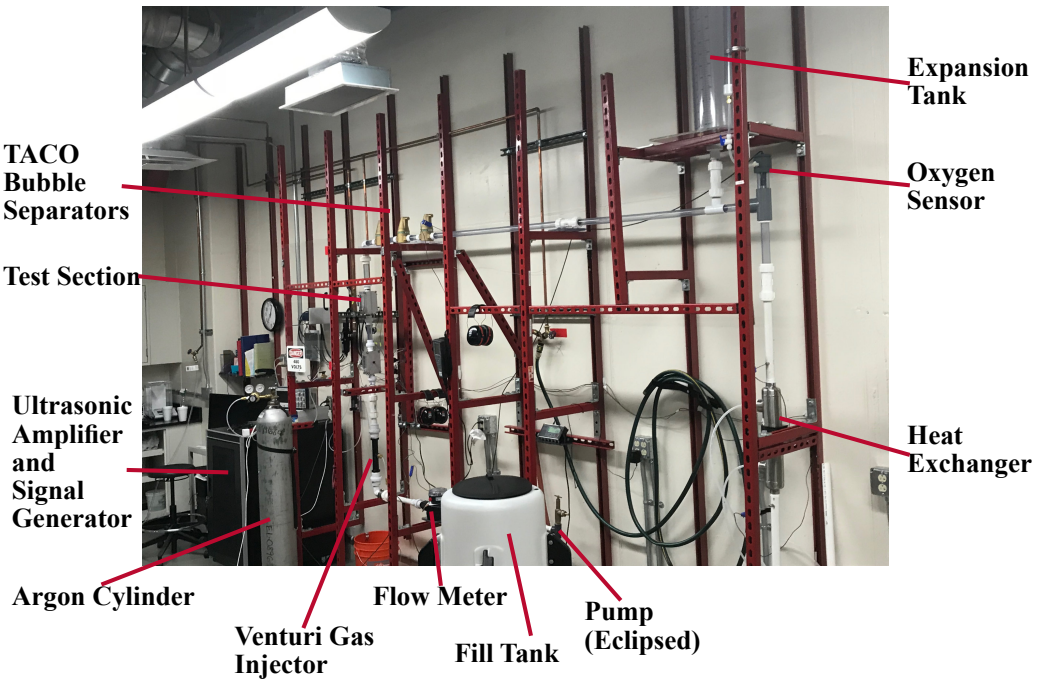

Figure 4.2: PULST Loop.

4.1.1 Ultrasonic Generator

The ultrasonic generator and amplifier is a Tektrinonx signal generator with at ± 20 Vpp variable wave output. The signal generator fed into a Model KC N15-1 ultrasonic amplifier from Kinetic Ceramics. The amplifier was modified by the vendor to provide an output of 10 kHz to 100 kHz for a rated output power of 1.5 kW. The output was used to drive the selected STEMiNC 120 W and 1 kW transducers. The amplifier also provided an output voltage indication. The amplifier was installed into a Precision Enclosure Systems rack equipped with a 15 amp capacity breaker. In order to achieve good transmission of acoustic power, petroleum jelly was used as a couplant due to its ease to acquire and use. The transducers will be discussed in more detail with the test sections. To measure the output signal of the amplifier, an oscilloscope was attached to the amplifier's voltage indication output.

This provided applied voltage and frequency data. The wiring schematic is shown in Figure 4.3. The current applied was measured with a clamp-on type ammeter. This type of ammeter was necessary because the current applied was anywhere between 2 *amp* to 15 *amp*.

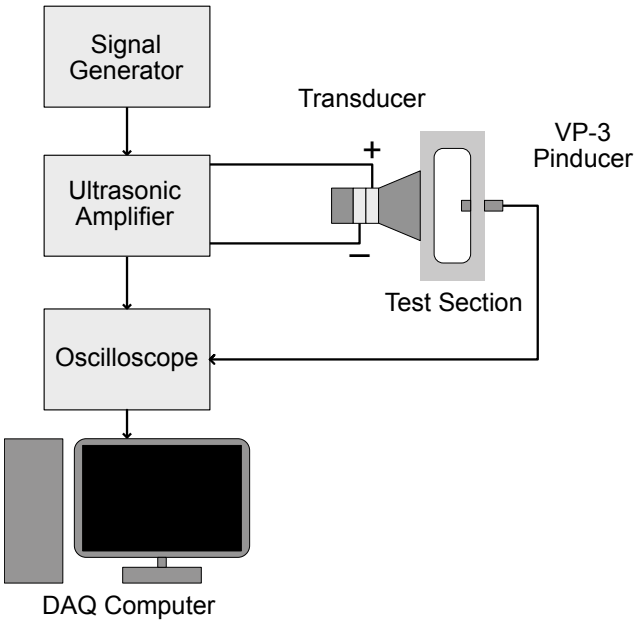

Figure 4.3: Schematic of the ultrasonic production components and acoustic intensity measurement.

4.1.2 Bubble Injection and Removal

The bubble injector is a venturi style injector from Mazzei as shown in Figure 4.4. It is attached to the building air supply for oxygen saturation and the inert gas supply for oxygen stripping via a three way valve. The bubble sizes produced from the generator were dependent on the flow rate through the venturi and glycerol concentration. Higher flow and higher glycerol concentrations corresponded with smaller bubbles. To keep bubbles small, a micro mesh was installed just down stream of the injectors.

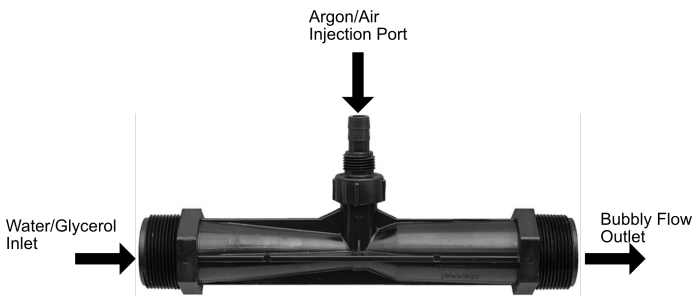

Figure 4.4: Diagram of the Mazzei venturi gas injector used in the PULST Facility.

The bubble removal solution implemented was a TACO 4900 series air separator. The air separator is rated by the vendor to separate bubbles as small as 20 μm for water and glycol. Because they were rated with glycol, it was anticipated that they would also work well with glycerol/water mixtures. This model of separator uses pall rings to coalesce smaller bubbles into larger bubbles that would be separated. The documented maximum effective velocity for the separators was 1.52 m/s (5 ft/s) which corresponds to 51.1 LPM (13.5 GPM) for 1$''$ Schedule 40 piping (ID 2.66 cm). The loop was designed with three of these separators in series in order to ensure that all bubbles have been removed. The configuration of separators is illustrated in Figure 4.5. During shakedown testing, the performance was tested with water and the volumetric flow limit was found to be around 37.8 LPM (10 GPM). Unfortunately, during the glycerol/water runs the bubbles produced were very small, and the separators were not as effective and would allow some bubbles to pass through.

4.1.3 Data Acquisition System

The data acquisition system is a combination of a LabView vi and DO probe with instrumentation. The LabView program was designed to take and display flow and temperature information. Thermocouples (T-type) were placed at various positions around the loop, specifically upstream and downstream of the test section and up-

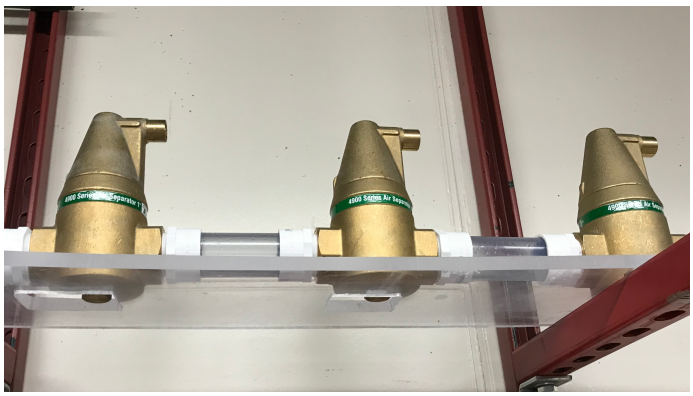

Figure 4.5: The set of TACO 4900 bubble separators installed in series.

stream and down stream of the heat exchanger as noted in the system schematic in Figure 4.1. The flow information is provided to the DAQ by a positive displacement volumetric flow meter. The flow meter used was a Badger Meter Record All (RCDL) nutating disc flow meter with equipped with a 4 to 20 *ma* signal output. A positive displacement flow meter was specifically chosen due to the change of viscosities and densities due to the varying concentrations of glycerol. Because the flow meter was calibrated in total flow (totalizer), the variance of the flow signal was very large, but it was cyclical and predictable. To address this, the signal was averaged in the DAQ vi. The last key feature of the vi was real time *Re* display. The vi used the temperature at the test section, which was approximated as the average of the temperatures downstream and upstream of the test section, and the volumetric flow. The viscosity and density calculations used in the *Re* calculation are discussed in Appendix A. The interface vi is shown in Figure 4.6.

The DO measurement were taken with a Xylem ProODO Optical DO and Temperature instrument. The proprietary software provided by Xylem was capable of reading and logging DO and local probe temperature in set intervals. Care was taken in the probe placement to ensure that the probe would be representative of the bulk DO concentration because of its placement in the loop. During construc-

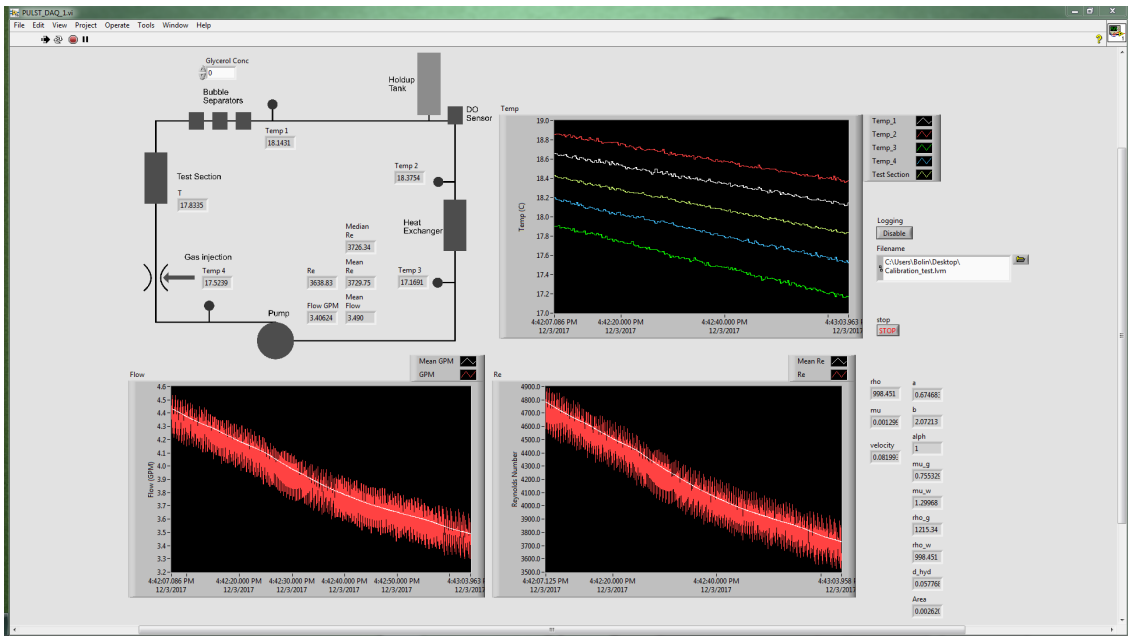

Figure 4.6: PULST data acquisition vi.

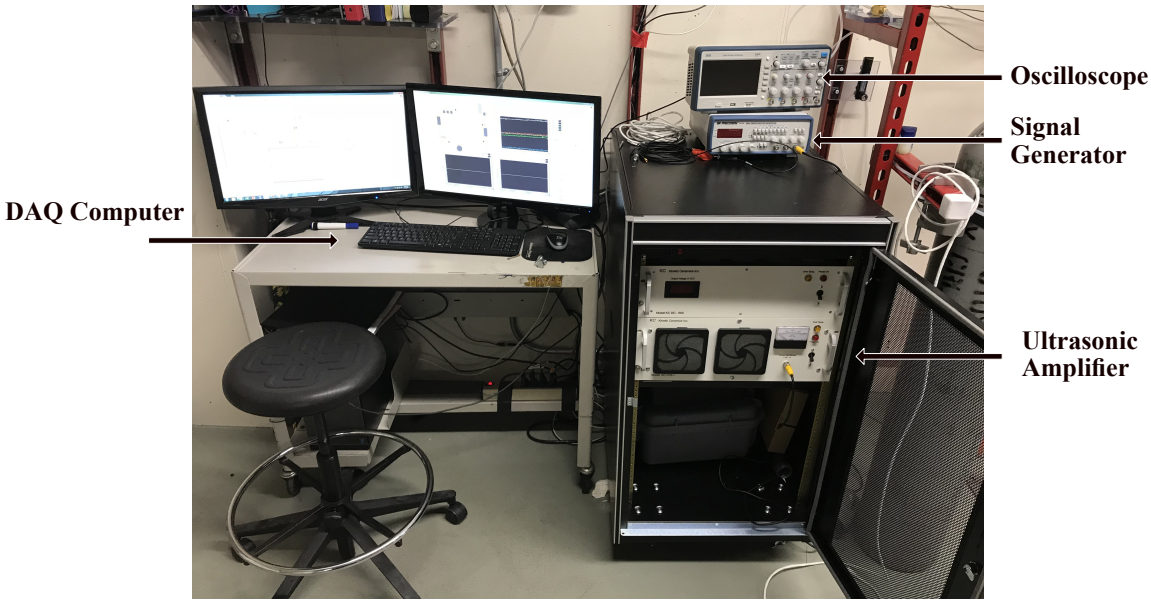

Figure 4.7: PULST data acquisition and ultrasonic amplifier station.

tion, the active sensor of the probe was verified to be in line with the centerline of the approaching flow.

To measure the acoustic intensity applied to the test section, a Vapley Fisher Pinducer (VP-3) from CTSCorp was used. This was instrumented into the test section across from the ultrasonic horn, as described in Section 4.2. It was read with the oscilloscope. The oscilloscope's FFT function was used to measure the voltage decibel (dBVrms), which can be used to calculate the acoustic intensity applied to the fluid. This is explained in more detail in Appendix E.

4.2 Test Section Design

The test section design had three design iterations. The design criteria of these test sections were to provide a chamber for bubbly flow to be able to be visualized and sonicated. The test section was also designed in such a way to be easily modified in order to accommodate a number of off-the-shelf transducers. The drawings for each of these test sections are included in appendix B.

The first iteration was designed to match the hydraulic area of 1″ Schedule 40 pipe (5.56 cm^2/0.864 in^2) and to allow for flow to fully develop by the sonication region. The early CAD rendering of this test section is shown in Figure 4.8. This test section was constructed with an aluminum top, aluminum bottom, delrin backing, and clear acrylic front shown in Figure 4.9. This design accommodated the mounting of two 120 W STEMiNC transducers while allowing for good visualization of the sonicated two-phase flow as shown in Figure 4.10.

The second iteration of the test section was designed, but not fabricated. It was designed with a thinner top plate and a wider flow channel to accommodate the entire diameter of the 120 W transducer. The goal was to increase the transmission

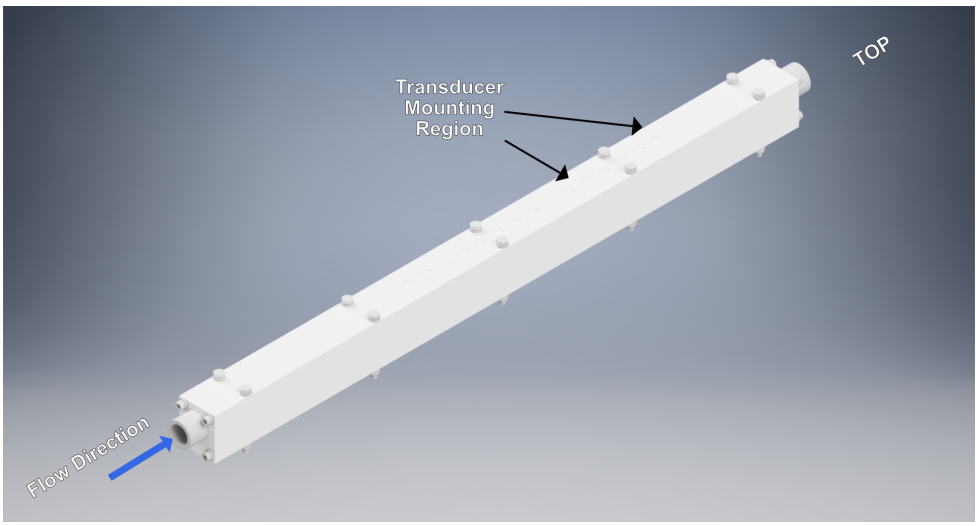

Figure 4.8: Notional CAD rendering of the PULST Rev 1 test section.

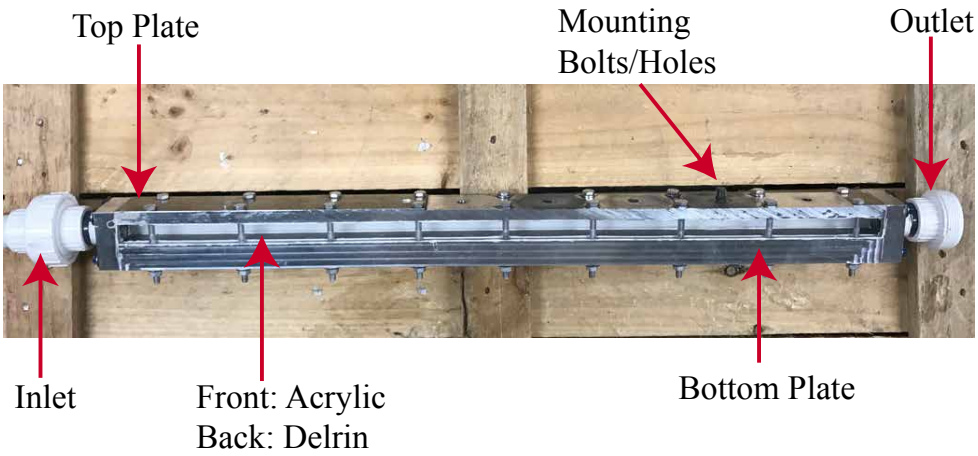

Figure 4.9: PULST Rev 1 test section.

of acoustic intensity by making the top plate thinner while being able to fully accommodate three transducers. From the performance of the first test section, the requirement for entrance length to ensure fully developed flow was discarded. The rendering of this test section is shown in Figure 4.11. To save time and construction costs, this design was used as the inspiration for the third iteration of the test section.

Figure 4.10: Revision 1 of the PULST test section installed.

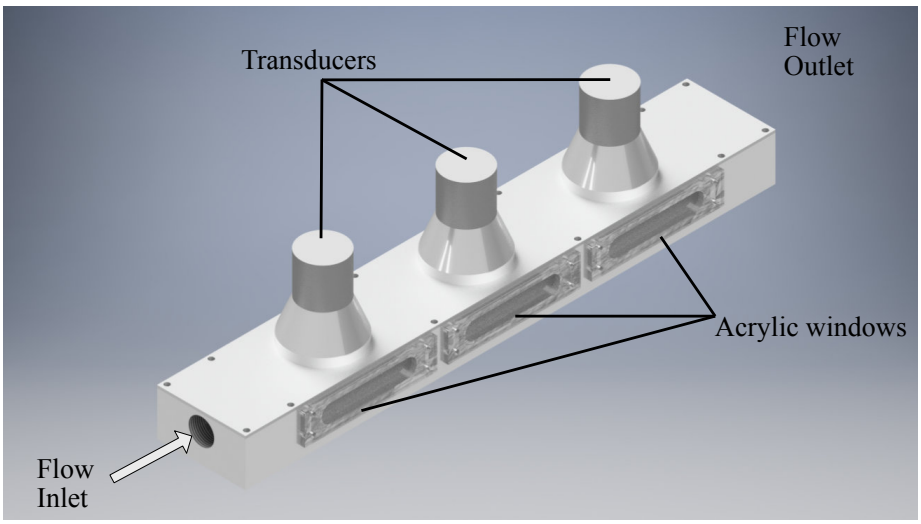

Figure 4.11: Revision 2 of the PULST test section.

The third iteration evolved from the second iteration by making the transducer sections more modular. Sections contained the transducer, piping connections, and windows. When two transducers were to be used, two test section modules were used. These are shown in the Figures 4.12 and 4.13. This design was able to incorporate the larger 1 kW STEMiNC transducer. To support acoustic intensity measurement, one of the test section bodies was modified to accommodate the VP-3 pinducer. The pinducer was placed in the center of the body just across the transducer as shown in Figure 4.14.

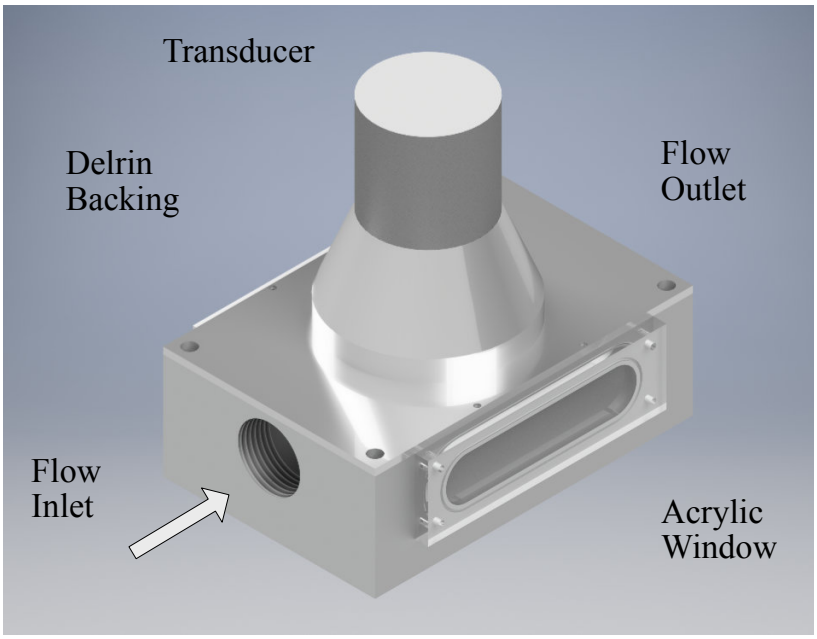

Figure 4.12: Third design of the PULST test section.

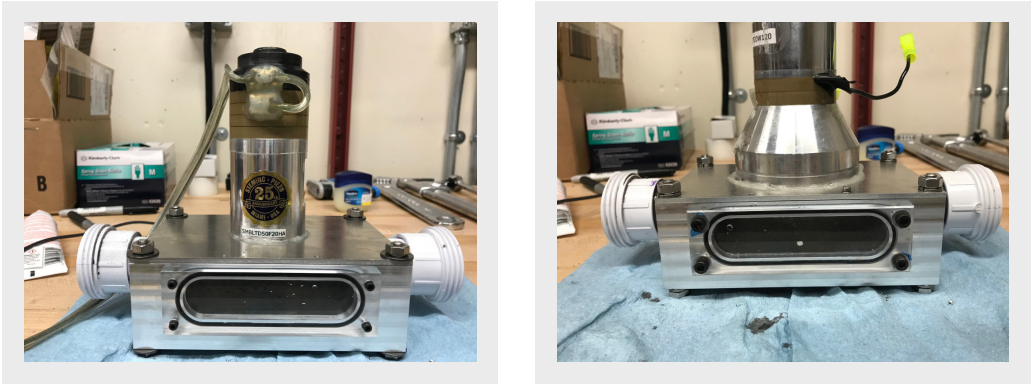

Figure 4.13: Modular test sections fitted with 1 kW and 120 W transducers.

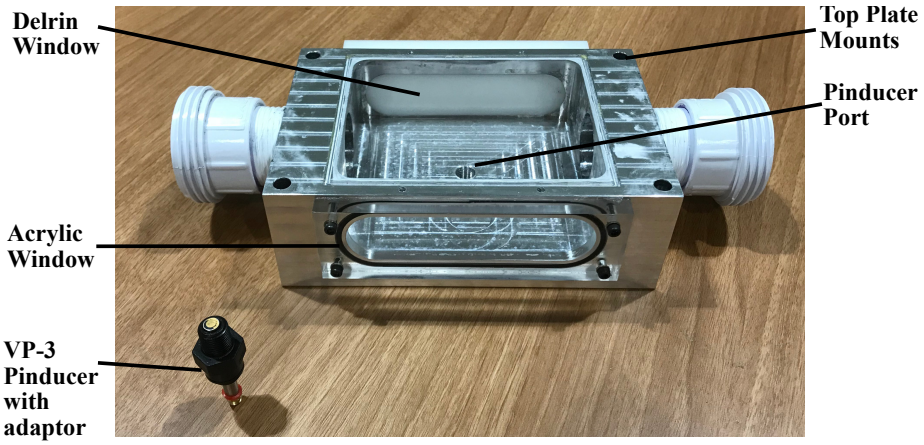

Figure 4.14: PULST test section body modified for VP-3 Pinducer.

4.3 Experimental Methods

The operation of the loop is to inject air until the fluid is saturated with oxygen, then switch the injection to argon to strip DO in accordance with the procedures in Appendix C. This is performed in over a test matrix that would cover a standard range of applicable glycerol concentrations and Re as shown in Table 4.1. In contrast to the SUMATRA experiment where Re was determined by glycerol concentration, Re is specifically targeted by flow rate for each glycerol concentration.

Table 4.1: Standard Test Matrix for the PULST experiment

		Re			
Glycerol $wt\%$	Corresponding flibe temp (C)	3500	4000	4500	5000
17.4	700				
24.7	650				
33.4	600				

Although the expansion tank had graduations, they were too coarse to make an accurate hold up measurement. In order to take this measurement, the expansion tank was replaced with a clear $1''$ schedule 40 pipe so that the difference in level can be measured and accurately correlated to a difference in volume.

The number density also required another modification. The test sections used for the DO stripping runs were too wide for the depth of field of the high speed camera, so the first revision of the test section was used. The width of the first test section was 2.54 cm $(1'')$ where the third revision test section width was 8.26 cm $(3.25'')$. This modification accommodated the camera's depth of field.

4.4 Results

The figures of merit from this investigation of mass transfer were the $k_L a$ and Sh. These results were gathered and analyzed similarly to the SUMATRA data. They are paired with the applied acoustic intensity for each run. Combination of these data shows the effect of the applied ultrasonics on the mass transfer and the effectiveness of the transmission of ultrasonics to the two-phase flow. In a similar manner to the SUMATRA experiment, interfacial areas and average diameters would have to be determined from high speed camera data.

4.4.1 Shakedown Testing

The first revision test section design was the only test section used during the shakedown testing phase of the PULST investigation. The shakedown testing was per-

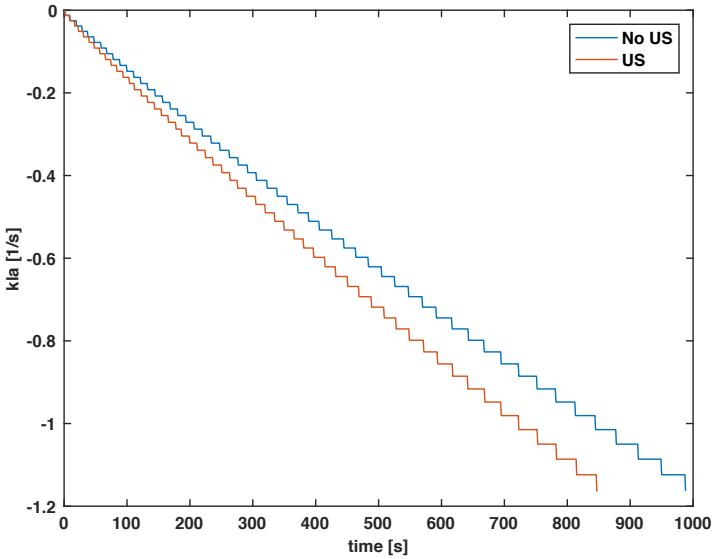

Figure 4.15: Typical PULST shakedown testing results for tap water with the first test section.

formed using the saturation/stripping procedure as detailed in section 4.3. This procedure was repeatedly preformed using tap water to learn the general behavior and performance of the test section. The k_La enhancement was generally between $0\ /s$ and $2 \times 10^{-4}\ /s$. These results were independent of the flow rate and number of transducers. The raw typical shakedown testing results are shown in Figure 4.15. The bubbles can be seen to be pushed away from the ultrasonic source as shown in Figure 4.16. Due to the visual observations and k_La performance, this test section was abandoned for the more modular third design that addressed the issues with acoustic intensity transmission and bubble interaction with the acoustic near-field.

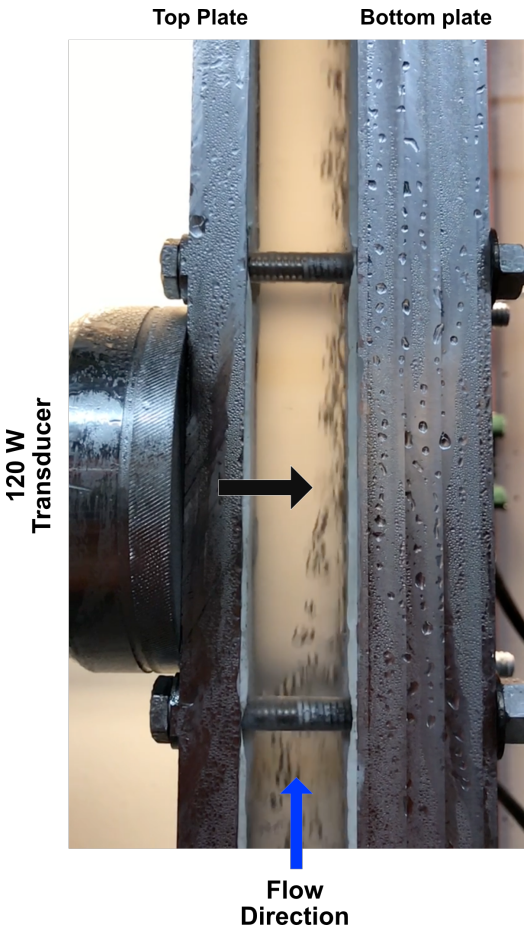

Figure 4.16: Bubble behavior during PULST shakedown testing for tap water with the first test section.

4.4.2 Volumetric Mass Transfer Coefficient Enhancement

The k_La enhancement was investigated over a test matrix that consisted of various ranges of Re and glycerol concentrations that correspond to flibe temperatures of $600°C$, $650°C$, and $700°C$ as shown in Table 4.2 and illustrated in Figure 4.17. Each data point is the average of 3 (or more) identical runs. If the k_La was suspect or the enhancement was negative, the runs were repeated for confirmation. The runs were performed with the single 120 W, two 120 W, and 1 kW transducers. For the

single 120 W configuration, the expanded test matrix, as shown in Table 4.3 was run through to include concentrations of 15 $wt\%$ and 35 $wt\%$ as illustrated in Figure 4.17 to verify the glycerol concentration range was sufficient to capture the mass transfer trend adequately.

Table 4.2: PULST Test Matrix

	Re			
Glycerol Concentration ($wt\%$)	3500	4000	4500	5000
17.4				
24.7				
33.4				

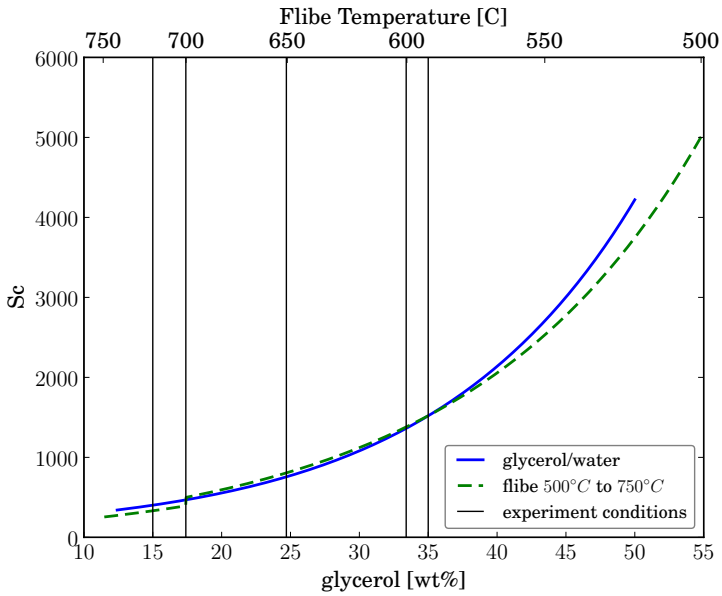

Figure 4.17: Comparison of Sc of flibe and glycerol/water mixtures with the PULST experimental points highlighted.

The k_La enhancement results of the single 120 W transducer is shown in Figure 4.18, the results for the double 120 W transducers are shown in Figure 4.19, and the results of the 1 kW transducer is shown in Figure 4.20. These figures show the enhancement of the k_La. One note about the results from the single 120 W transducer in Figure 4.18 and the 1 kW transducer in Figure 4.18, the point at $Re = 3000$

Table 4.3: PULST Expanded Test Matrix

	Re			
Glycerol Concentration ($wt\%$)	3500	4000	4500	5000
15.0				
17.4				
24.7				
33.4				
35.0				

was taken to determine if a lower Re would result in a noticeable enhancement of performance. It was determined that the bubbles produced were significantly larger than bubbles produced at Re of 3500 and under sonication, were visually unaffected. Because of this finding, no other data at Re of 3000 were taken.

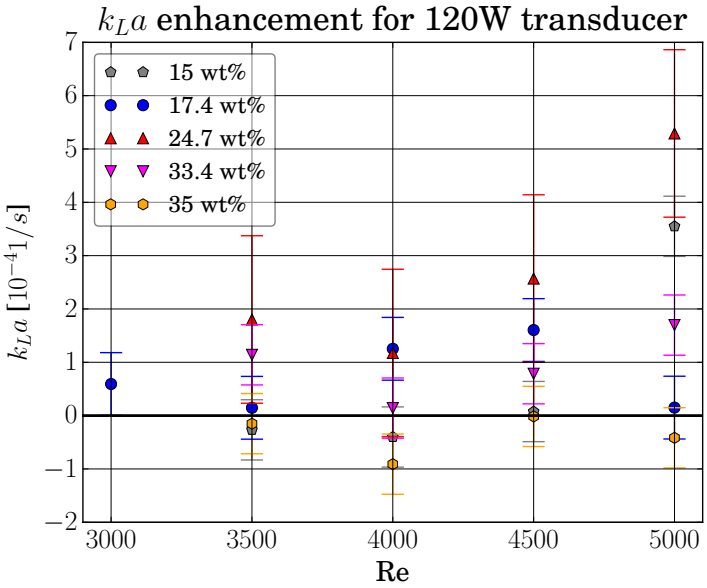

Figure 4.18: k_La enhancement for the single 120 W transducer.

A closer look at these results show the majority of points do show a positive enhancement. The uncertainty in the data comes from a variation in the individual runs, even though the runs were conducted as identically as possible. Some data showed a relatively small increase in efficiency, but others showed a largely negative

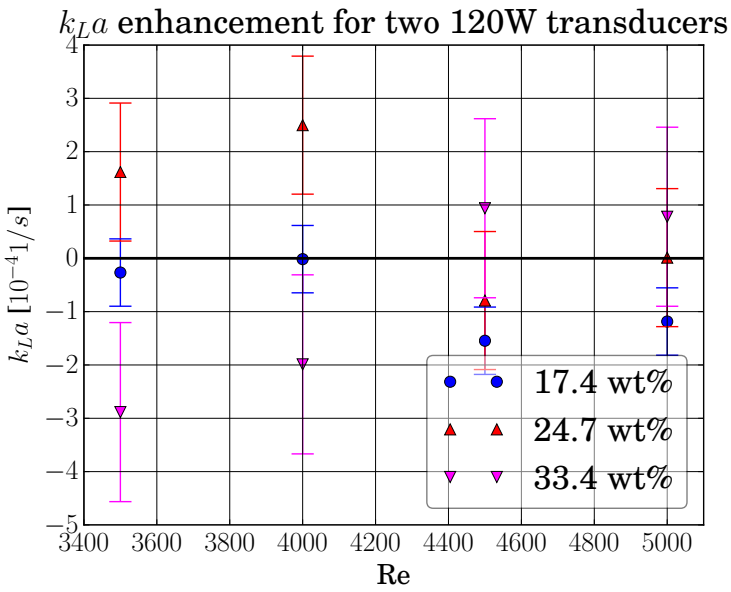

Figure 4.19: k_La enhancement for the two 120 W transducers.

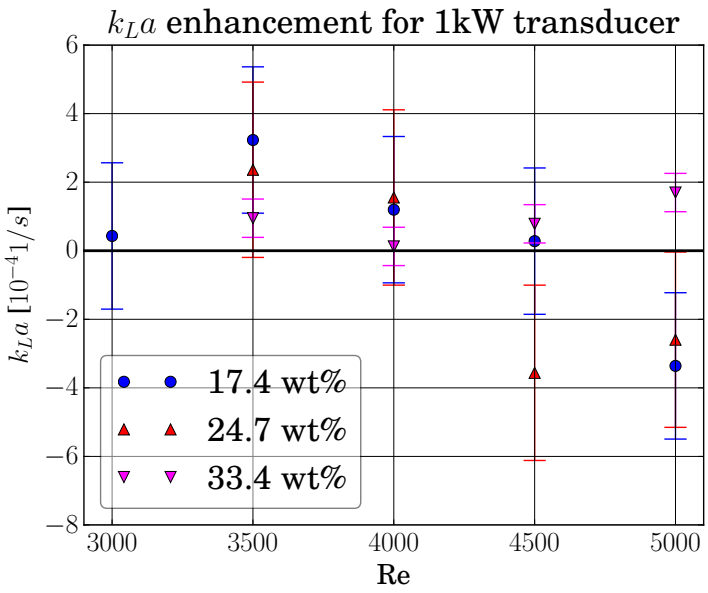

Figure 4.20: k_La enhancement for the 1 kW transducer.

effect of ultrasonics. For the 120 W transducer, extra runs were able to be performed to lower the error of the data points. These extra runs were not performed for the 1 kW transducer because the transducer would degrade and break over time during use. The location where the transducer would fails is along the bolt threads inside of the transducer. The holding bolt is steel, while the horn of the transducer is aluminum, causing any operation to gradually strip the threads and making the mounting unreliable.

4.4.3 Sherwood Number

The Sh is calculated by determining the volumetric mass transfer coefficient $k_L a$ and the interfacial are a. The method of finding the a is similar to the SUMATRA experiment using equation (3.5). The holdup (ε) for the PULST loop was determined by replacing the expansion tank with a calibrated pipe in order to quantify the change in volume. This measurement was difficult to make for the higher glycerol concentrations due to the inability of the bubble separators to remove bubbles. The change in volume that was needed was the change in volume of the bubbles between the injector to the bubble separators. Due to the bubble blow by the separators, the measured change in volume could be due to gas settling in other points in the loop such as local high points and strainers. This local bubble collection is evident when the pump is switched off, and the collected gas becomes liberated from the lower points in the loop and escapes. So, for the higher concentrations, the volumes were taken when the first blow by bubbles were noticed. The measured holdup is shown in Figure 4.21. Last variable to determine for Sh (equation (3.5)) is the number density (N). The determination of the number density is outlined in Appendix D. The results from the analysis are shown in Figure 4.22.

The interfacial area and average bubble diameter can be determined using the

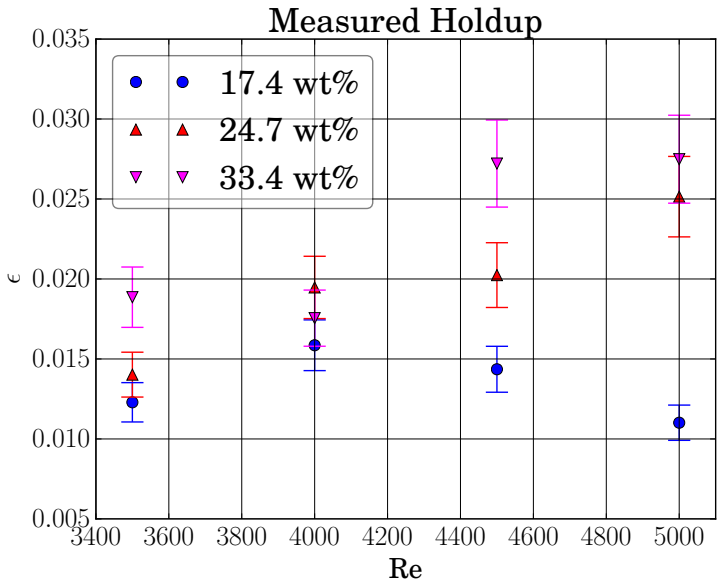

Figure 4.21: Measured holdup for the PULST experiment.

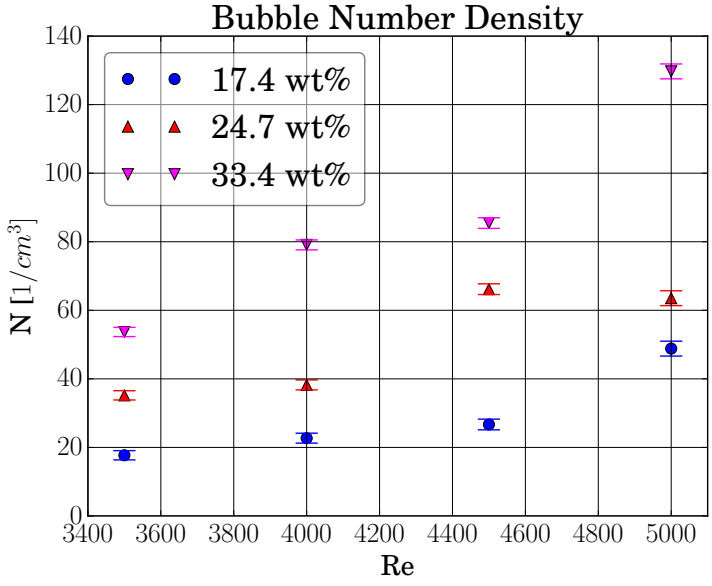

Figure 4.22: Number Density of bubbles in the PULST experiment.

holdup, and the results are shown in Figures 4.23 and 4.24, respectively. In turn, the Sh can be determined using equation (3.3). The Sh results for the 120 W, 2 120 W, and 1 kW tests are shown in Figures 4.25, 4.26, and 4.27, respectively.

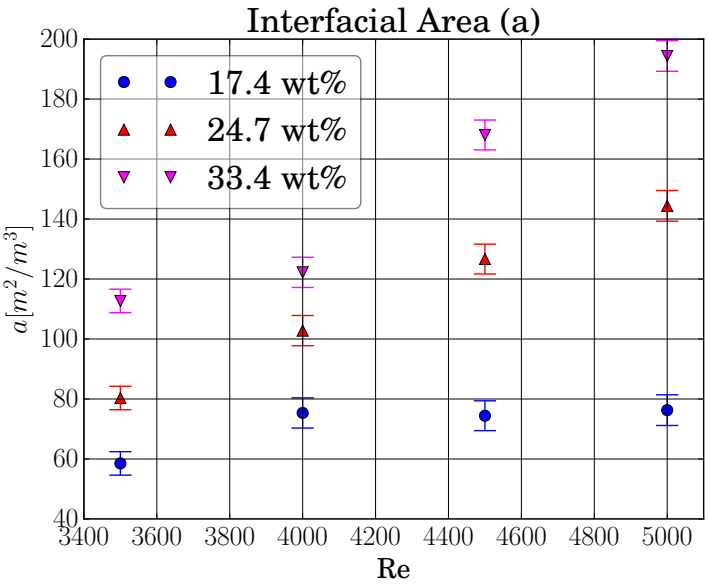

Figure 4.23: Interfacial area in the PULST experiment.

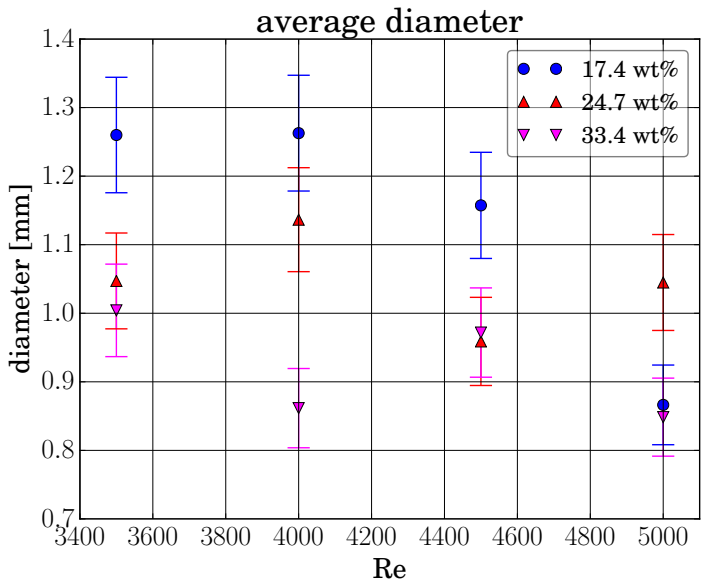

Figure 4.24: Average bubble diameter in the PULST experiment.

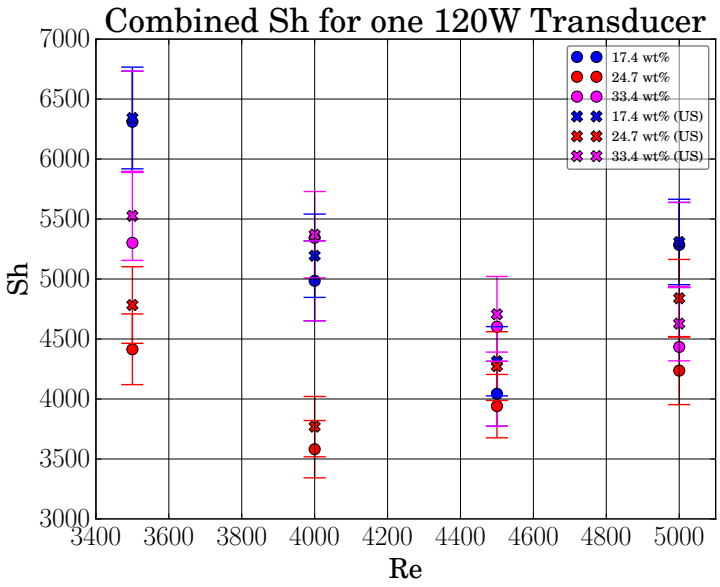

Figure 4.25: Sh comparison for the 120 W case.

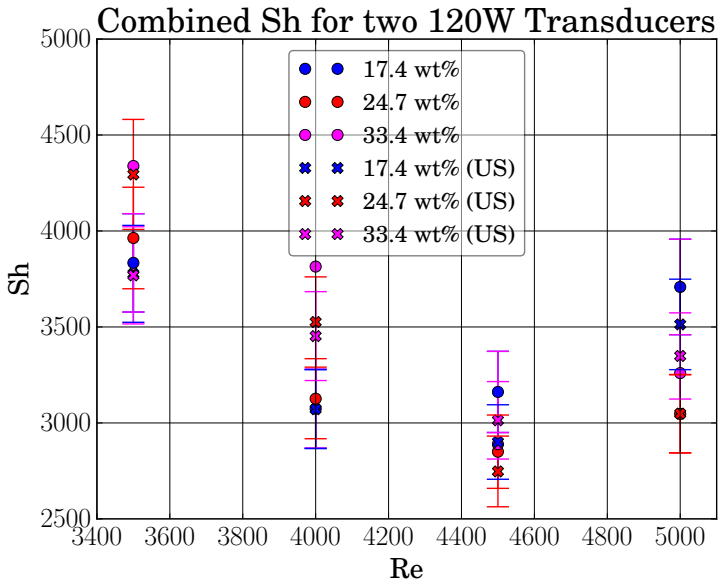

Figure 4.26: Sh comparison for the two 120 W module case.

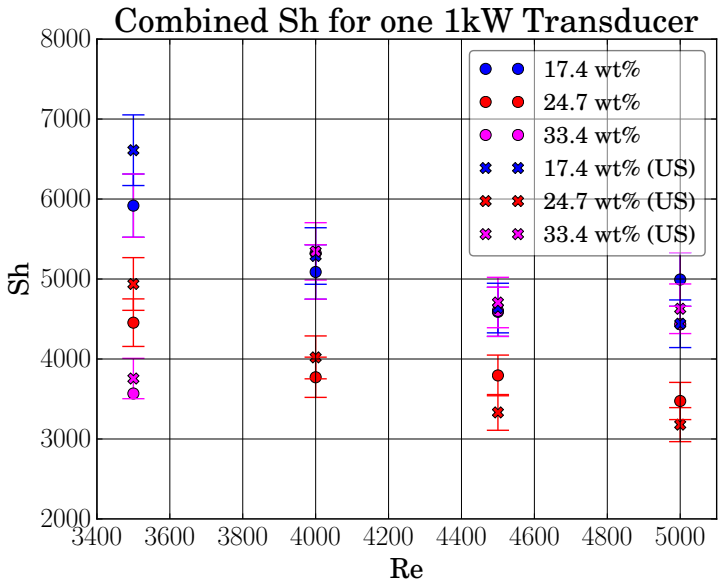

Figure 4.27: Sh comparison for the 1 kW case.

4.4.4 Acoustic Intensity

The measured power delivered by the one 120 W, two 120 W, and 1 kW transducer configurations was roughly the same. This was uniform power reading was unexpected. What seemed to be the major factor in power delivery was the frequency applied to the horn/test section. The highest power seen, and also the most audibly loud, tended to be when the signal generator was tuned into the natural resonance frequency of the horn/test section. The power measured was anywhere between 1.8 kW to 3.4 kW, which is larger that the 1.5 kW rating of the amplifier. Measurements were performed with a clamp-on type ammeter and the V_{rms} measurement on the oscilloscope for each run. Direct acoustic intensity measurements would be the best way to indicate power delivered as well the only option to measure acoustic intensity.

The acoustic intensity was directly measured using the Valpey Fisher VP-3 pinducer read with the Bk Precision oscilloscope. The process of measurement and calculation is detailed in Appendix E. The results are displayed in Tables 4.4, 4.5, and 4.6; and Figures 4.28, 4.29, and 4.30.

Table 4.4: Acoustic Intensity ($\times 10^{-9}$ W/cm^2) for one 120 W Transducer

Re	3500	4000	4500	5000
17.4 $wt\%$	25.12	25.12	8.32	25.12
24.7 $wt\%$	229.09	229.09	478.63	331.13
33.4 $wt\%$	36.31	36.31	3.98	52.48

Table 4.5: Acoustic Intensity ($\times 10^{-9}$ W/cm^2) for two 120 W Transducers

Re	3500	4000	4500	5000
17.4 $wt\%$	25.12	25.12	8.32	25.12
24.7 $wt\%$	229.09	229.09	478.63	331.13
33.4 $wt\%$	36.31	36.31	3.98	52.48

Table 4.6: Acoustic Intensity ($\times 10^{-9}$ W/cm^2) for The 1 kW Transducer

Re	3500	4000	4500	5000
17.4 $wt\%$	8.32	12.02	12.02	10.00
24.7 $wt\%$	10.00	10.00	63.10	63.10
33.4 $wt\%$	109.65	36.31	158.49	17.38

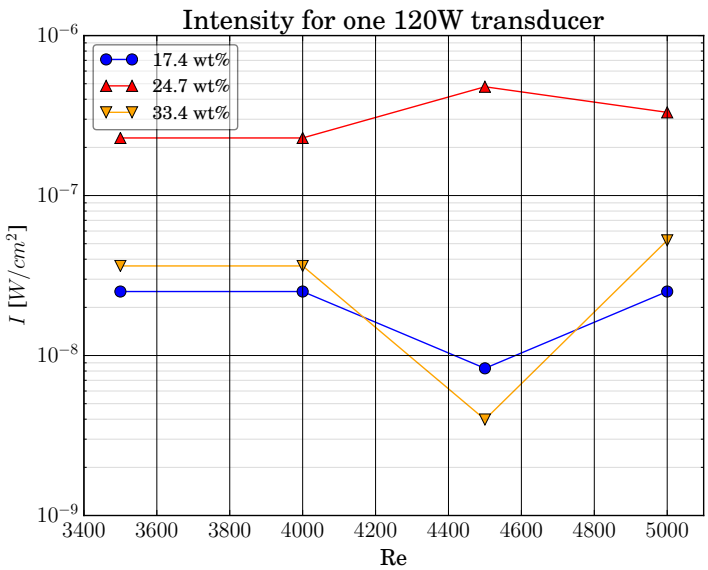

Figure 4.28: Measured acoustic intensity for one 120 W transducer.

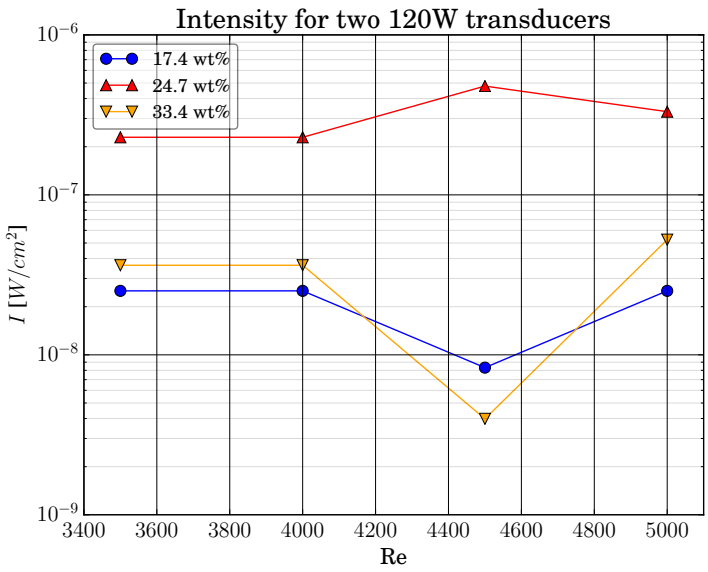

Figure 4.29: Measured acoustic intensity for two 120 W transducer.

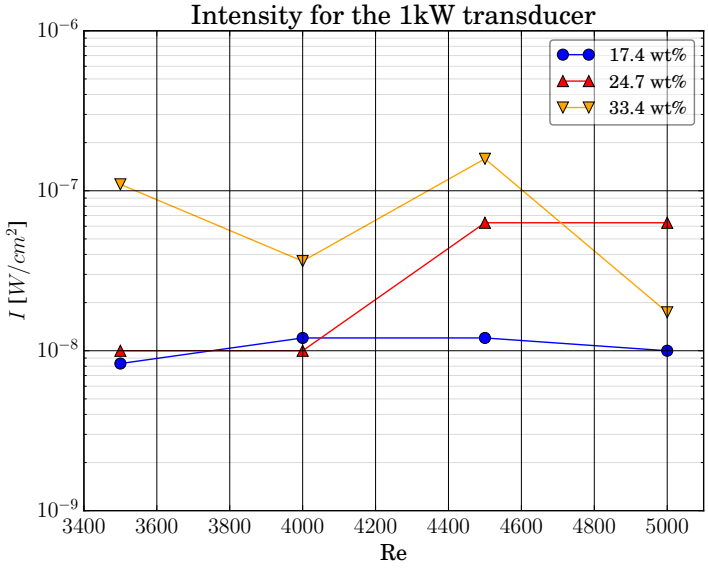

Figure 4.30: Measured acoustic intensity for the 1 kW transducer.

4.5 Discussion

Given the engineering constraints of the experiment, this result was unavoidable. The constraint to use off-the-shelf components was a clear factor. The main factor in this choice was to address the erosion constraint found with the SUMATRA loop. The immediate trade off was that the maximum achievable intensities would be curtailed. Despite the attention to prevent erosion, there appears to be some pitting and surface changes occurred on the test section top plates. This is illustrated in Figures 4.31 and 4.32. This erosion was due to the acoustic intensity on the top plate inducing cavitation. The other effect of using lower intensities was that the bubbles would now tend to avoid the ultrasonic near-field. These effects can be seen in the visual data as shown in Figure 4.33.

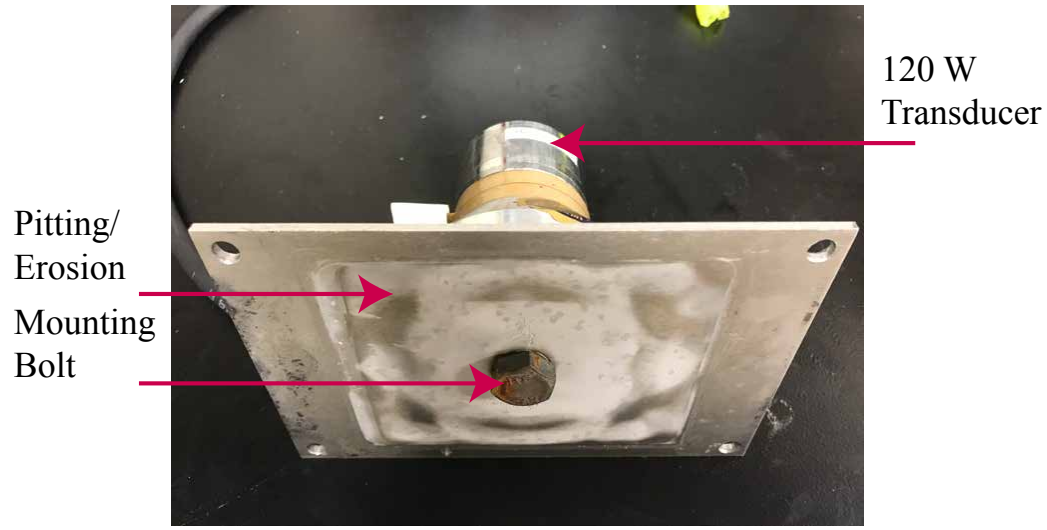

Figure 4.31: Underside of the top plate for 120 W after 60 hrs of testing.

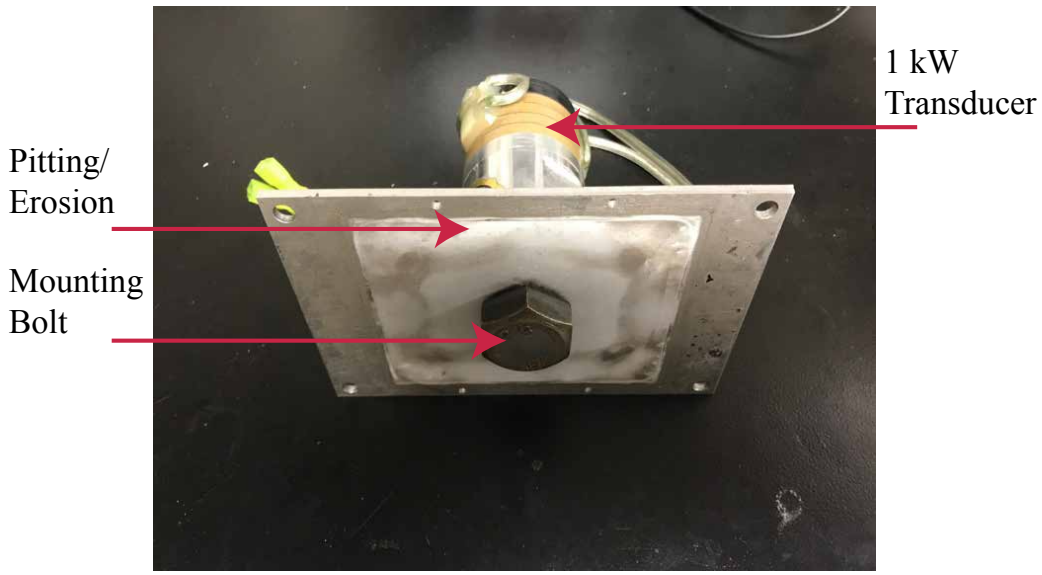

Figure 4.32: Underside of the top plate for 1 kW after after 20 hrs testing.

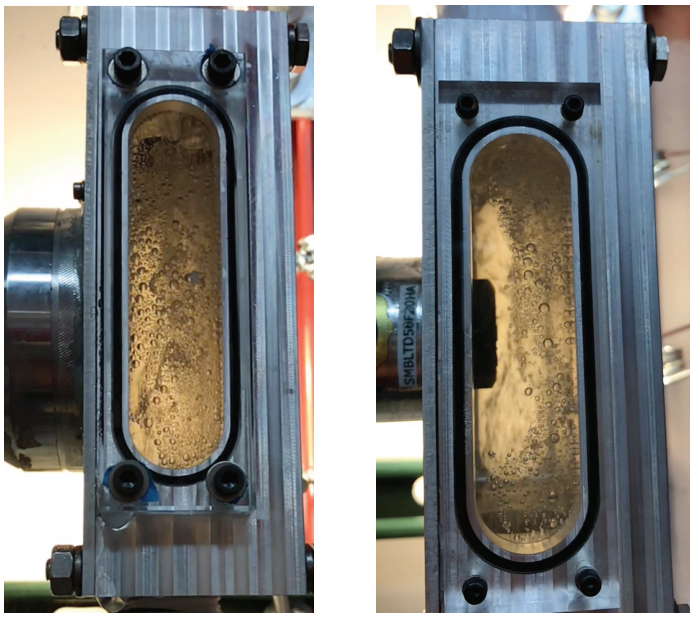

Figure 4.33: PULST test section during ultrasonic runs.

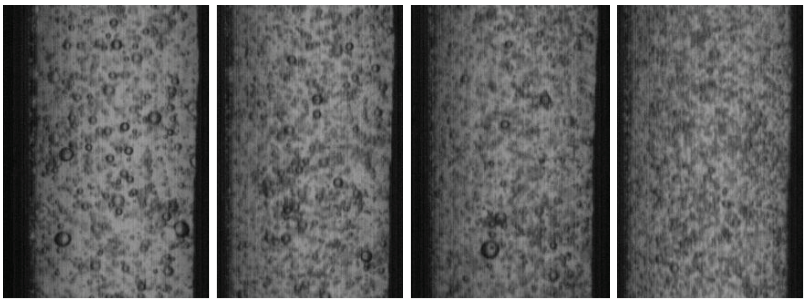

Figure 4.34: Sample PULST visual data for 17.4 $wt\%$.

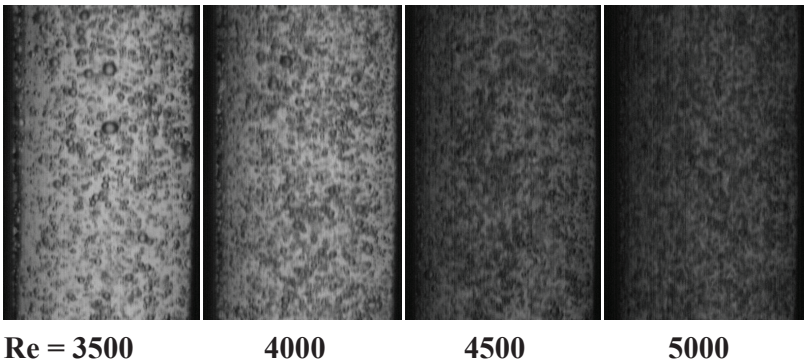

Figure 4.35: Sample PULST visual data for 24.7 $wt\%$.

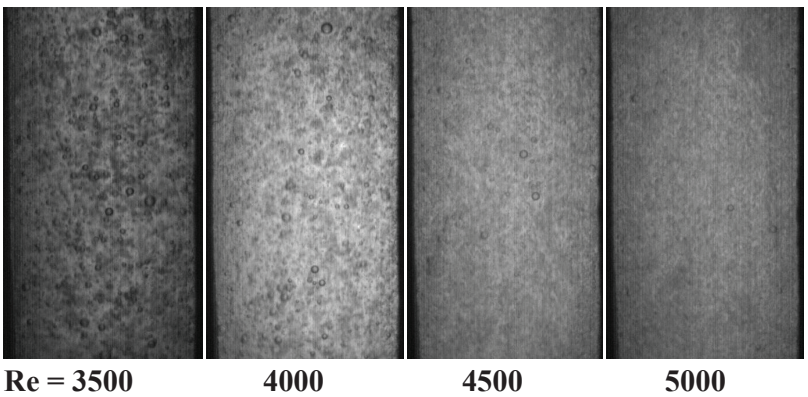

Figure 4.36: Sample PULST visual data for 33.4 $wt\%$.

The visual data was taken using a high speed camera focused on the windows in the test sections. Sample images are shown in Figures 4.34, 4.35, and 4.36. It shows that there is a visable relation between glycerol concentration and bubble size. This consideration is important due to the conclusion from the SUMATRA experiment which noted that the sparging mass transfer mechanism is dominated by the diffusive forces. This suggests that the mass transfer performance is inversely proportional to the average bubble size. It was also seen in the SUMATRA experiment that the increase in glycerol concentration, the smaller the average bubble diameter. Naturally, an increase in glycerol concentration will translate to smaller bubbles and an increase in the k_La, which is supported by the observed k_La. In the higher concentrations of glycerol, the addition of the ultrasonic field, the forces pushed the bubbles to the test section wall and, more importantly, forced the coalescence of small bubbles.

The last factor to consider is the applied acoustic intensity. This would indicate the effectiveness of transmitting acoustic energy from the transducer to the fluid. Simple intensity calculations using the rated power of the transducers show that the 120 W transducer yields an intensity of 2.44 W/cm^2 and the 1 kW transducer yields an intensity of 50.9 W/cm^2 at the horn face. This is significantly smaller than the 275 W/cm^2 from the previous experiment. This calculation cannot be taken as applied intensity because of the indirect sonication design. In order to obtain the applied intensity, it was directly measured. As shown in Section 4.4.4, the intensities measured were orders of magnitude lower. This would suggest that the acoustic energy was not simply transmitted as previously expected, but that the mounting of the horn had turned the entire test section into a horn itself. Also, the number density in this experiment was larger than the SUMATRA experiment, and this would attenuate the acoustic energy similar to a bubble curtain, as noted in Section 2.2. This would explain the acoustic energy being dispersed unpredictably and not transmitted into the fluid.

4.6 Conclusion

The final conclusion of this experiment is that the concept of indirect sonomechanical enhancement of sparging mass transfer is inconclusive when using commercial off-the-shelf components. A more customized prototype designs for the transducers, ultrasonic amplifiers, test sections, and bubble injectors is required to further demonstrate this approach. To determine the design space, a parameter study was performed to compare and contrast the parameters and conditions between the two experiments. This study is detailed in the following chapter.

Chapter 5

Comparison Study

To determine the factors that contributed to the PULST experiment not producing notable enhancements in mass transfer where the SUMATRA experiment produced significant increases in mass transfer will follow these following steps. First, the parameters that are common and have would have any impact on the ultrasonic enhancement will be listed and evaluated. Second, the experimental data will be investigated in that parameter space to contrast the experiment in various parameters spaces. Finally, the variances will be evaluated, and the conditions and parameters could be identified that would make the PULST experiment, or a subsequent experiment successful.

5.1 Tabulation of Parameters

The list of important parameters contrasted between the two experiments in the following Table 5.1. They are broken up between fluid properties and acoustic properties. Naturally some parameters overlap between fluid and acoustic properties, namely bubble density and fluid density (which is manifested in impedance ratio).

It would also be important to mention that the two experiments are different categories of acoustic reactors. The SUMATRA experiment is a probe reactor, and the PULST experiment is a bath reactor. Because of this, commensurate data are not superficially apparent in comparisons, and conclusions must be considered carefully.

Table 5.1: List of Comparison Parameters for the PULST and SUMATRA experiments

SUMATRA	**PULST**
Fluid Properties	
Re	Re
Sc	Sc
Bubble Diameter	Bubble Diameter
Temperature	Temperature
Denisty	Density
Viscosity	Viscosity
Glycerol Concentration	Glycerol Concentration
Flow Velocity	Flow Velocity
Bubble Injection Rate	Bubble Injection Rate
Test Section Volume	Test Section Volume
	Number of Modules
Acoustic Properties	
Probe Reactor	Bath Reactor
Intensity Applied	Intensity Applied
Intensity Transmitted	Intensity Sensed
Impedance Ratio	Impedance Ratio
Frequency	Frequency
Bubble Diameter (Resonance)	Bubble Diameter
Bubble Density	Bubble Density
Ambient Pressure	Ambient Pressure
Acoustic Residence Time	Acoustic Residence Time
Horn Mass	Horn/Test Section Mass
Horn Geometry	Horn/Test Section Geometry

5.1.1 Parameter Space Comparisons

The first look at the experimental data is the comparison of k_La enhancement. As shown in Figure 5.1, the k_La difference over the range of Re shows the enhancement of the SUMATRA experiment to be larger across the range, as discussed earlier. The next comparison is the relation of Re and Sh between the two experiments. As shown in Figure 5.2, the SUMATRA experiment produced significantly lower Sh compared to the PULST experiment in the overlap of Re. A similar look at the relation of Sh to Sc will be similar because Sc was designed to overlap.

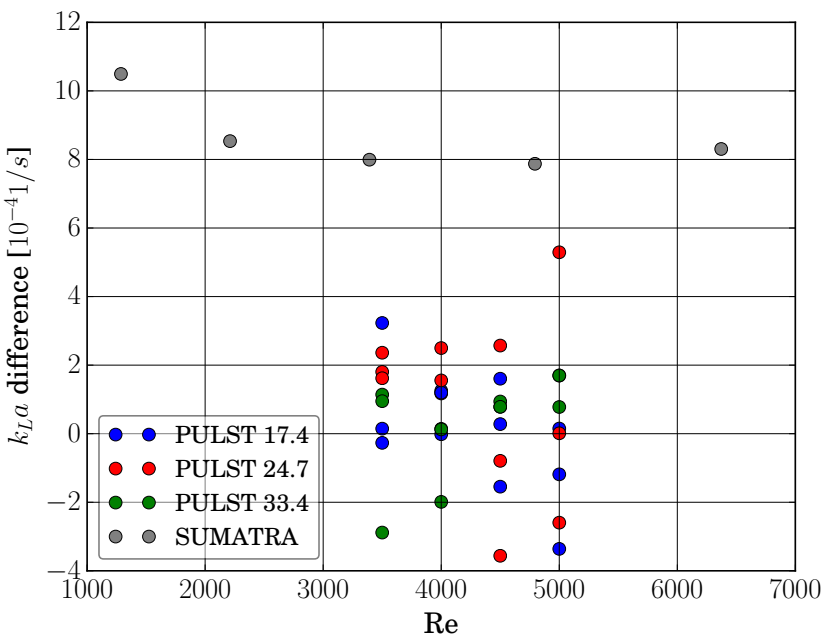

Figure 5.1: Comparison of volumetric mass transfer coefficient and Re.

Focusing on the physical interaction zone of the ultrasonics, the residence time (τ) in the ultrasonic region is compared in Figure 5.3. The ultrasonic volume is defined by as a cylinder below the face of the ultrasonic horn. This shows that the SUMATRA experiment utilized a smaller ultrasonic residence time than all of the

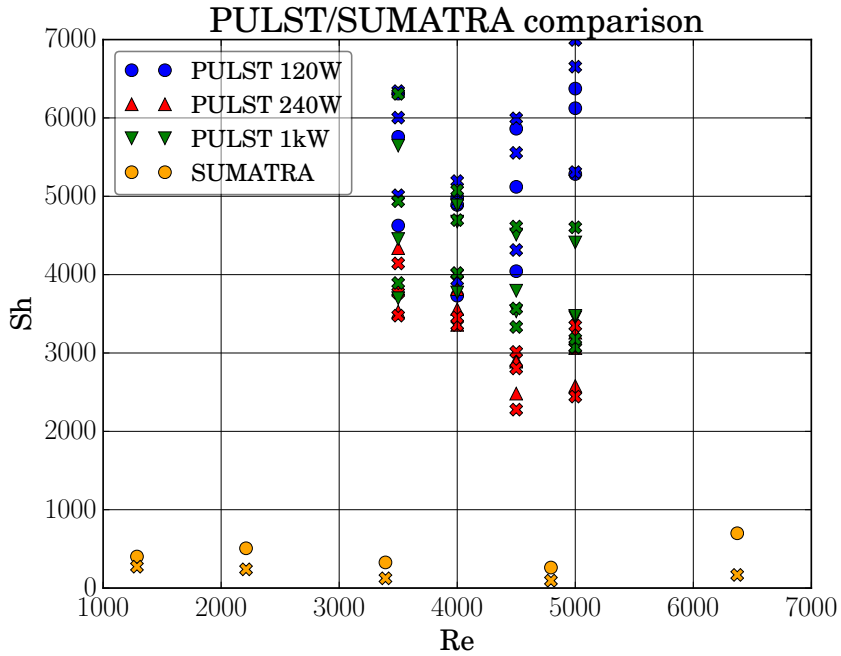

Figure 5.2: Comparison of Sh and Re. (ultrasonic data indicated with 'X')

PULST experiments. Therefore, a small conclusion can be made that the residence time was not a significant comparative factor for the success of the SUMATRA experiment, since the PULST experiments had larger residence times. Although these are superficial residence times, calculated as acoustic volume over volume flow rate. This analysis may overlook any eddy formations in the SUMATRA and PULST test sections where some bubbles may have longer residence times.

Another key factor is the number density (N) between the two experiments. The number density contributes to two important factors. First is the interfacial area. The larger number density should equate to a lower Sh and better mass transfer. Second, the number density will have an effect on the acoustic impedance of the fluid, because it would mimic a bubble curtain. This will in turn have an attenuation effect on the transmitted acoustic energy. As shown in Figure 5.4, the number density for the PULST experiment was larger than the SUMATRA experiment. The SUMATRA

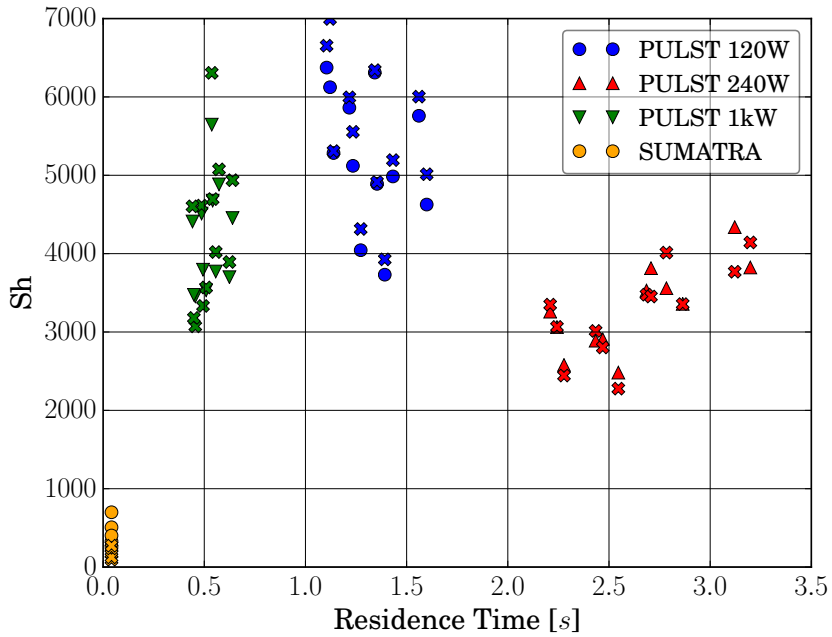

Figure 5.3: Comparison of Sh and residence time. (ultrasonic data indicated with 'X')

data are clustered at low Sh and number density, whereas the PULST data are shown having higher number densities and Sh.

Between Figure 5.1 through 5.4, it can be seen that the experiments have significant differences, which lead to very different mass transfer performances. In order to further investigate the differences, a three-dimensional variable space is used to compare and contrast. What can be taken from this first step is that in the smaller SUMATRA experiment, the conditions were optimal in ultrasonically enhancing mass transfer with a small residence time and number density.

Looking closer at the ultrasonic behavior, the next few figures compare the differences between the applied intensity and the impedance ratio on the ultrasonic Sh in Figure 5.5, 5.6, and 5.7. This shows a representation of the factors involved

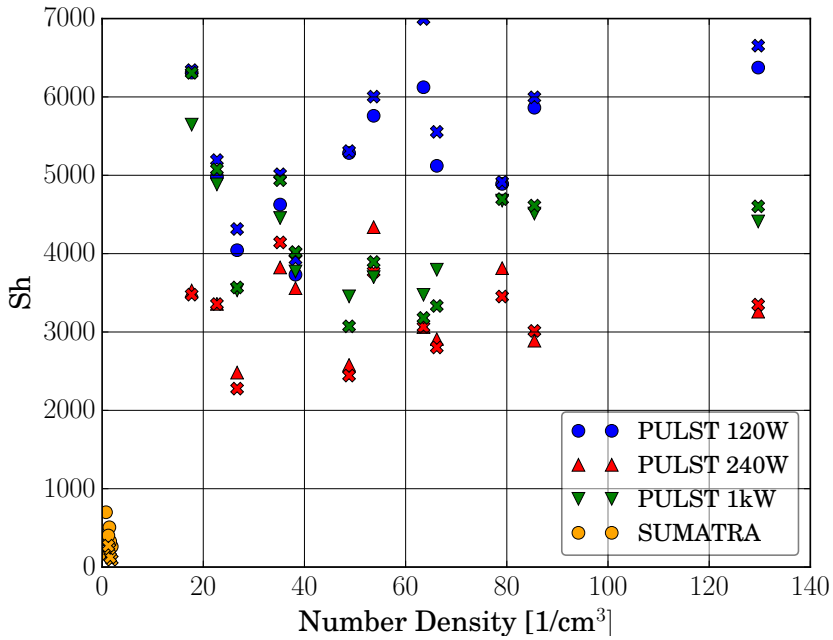

Figure 5.4: Comparison of Sh and number density. (ultrasonic data indicated with 'X')

with the transmission behavior and magnitude of intensity into the fluid. For all three PULST configurations, the impedance ratio and applied intensity places these conditions quite far from the SUMATRA conditions. The impedance ratio for the PULST experiment is below the impedance ratio for the SUMATRA experiment. This impedance ratio contrast is simply due to the different horn materials and glycerol concentrations. The PUSLT experiment used aluminum where horn used in the SUMATRA experiment was a titanium alloy (Ti-6Al-4V). The SUMATRA concentrations were 0, 12.5, 25, 37.5, and 50 $wt\%$ and the PULST concentrations were 17.4, 24.7, and 33.4 $wt\%$.

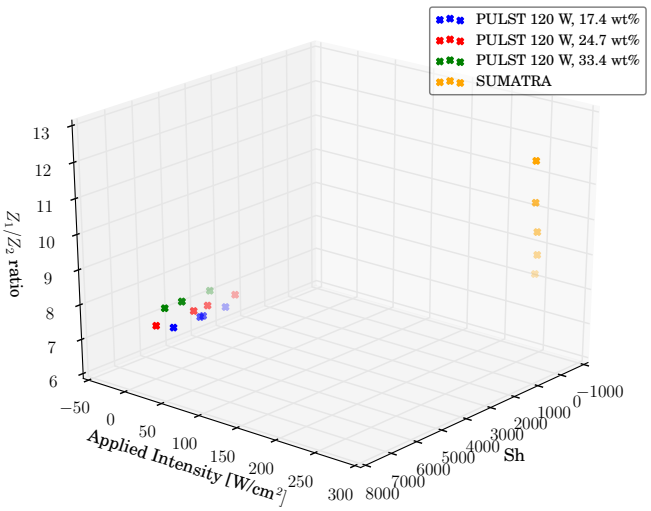

Figure 5.5: Comparison of Sh, applied intensity, and acoustic impedance ratio for 1 120 W transducer.

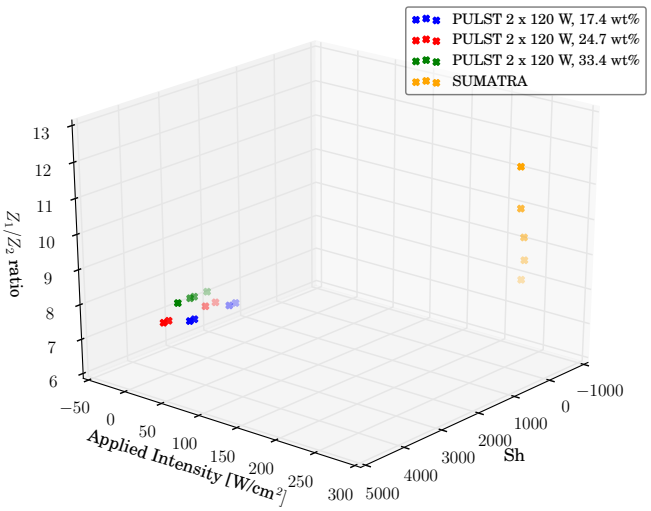

Figure 5.6: Comparison of Sh, applied intensity, and acoustic impedance ratio for 2 120 W transducers

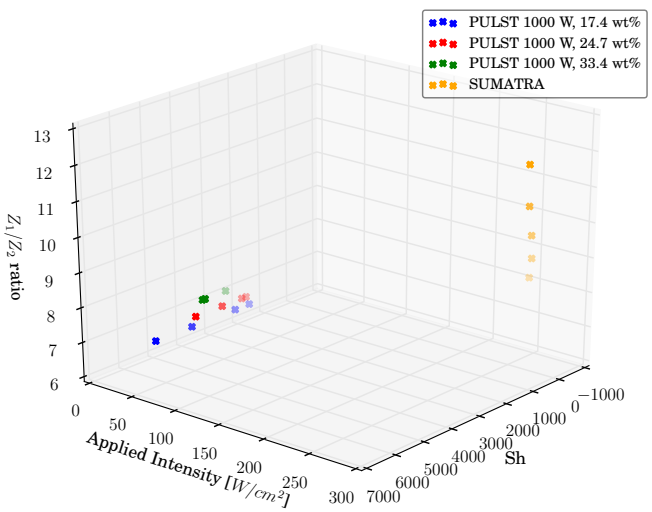

Figure 5.7: Comparison of Sh, applied intensity, and acoustic impedance ratio for the 1000 W transducer.

The data are indicating that intensity transmission is a key factor. To look more closely into this, factors that affect the transmission of intensity was plotted and compared. The Figures 5.8, 5.9, and 5.10 show the relation between applied intensity, horn mass, and Sh. The point of comparing the horn mass is to understand the material difference the two ultrasonic transducers had to vibrate. It is understandable that the more mass that must be moved, the lower the ratio of input power that will be transmitted to the working fluid. The PUSLT horn, from observations, is not just the transducer that was mounted, but the transducer and test section combined. Due to this extra mass, the piezo in the PULST transducer must vibrate more material than designed. This would have a negative effect on the acoustic energy transmitted, as expected. As seen in Figure 5.8, Figure 5.9, and Figure 5.10 the SUMATRA horn was significantly less massive than the PULST test section and horn assembly.

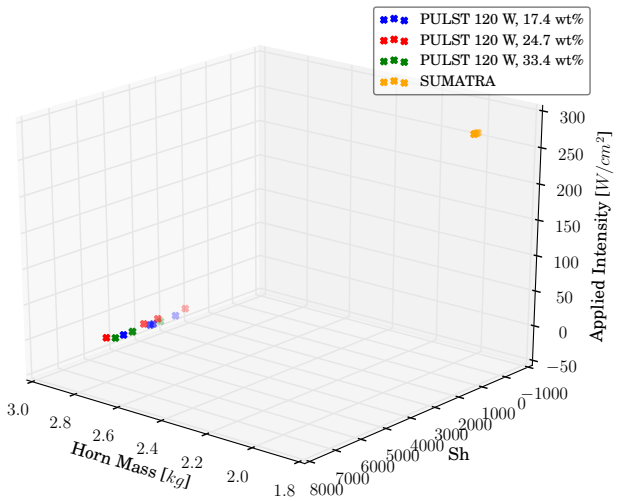

Figure 5.8: Comparison of Sh, applied intensity, and horn/test section mass for 1 120 W transducer.

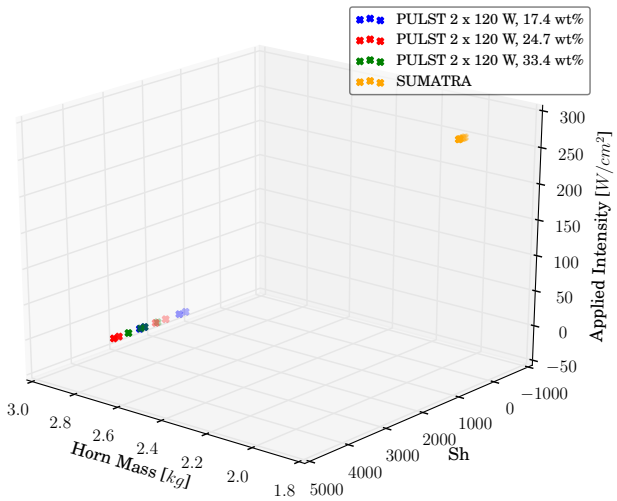

Figure 5.9: Comparison of Sh, applied intensity, and horn/test section mass for 2 120 W transducers.

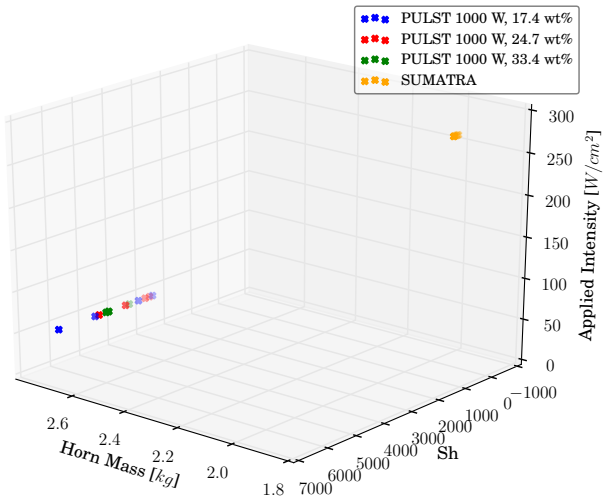

Figure 5.10: Comparison of Sh, applied intensity, and horn/test section mass for the 1000 W transducers.

Continuing to focus on the factors that can lower acoustic intensity, the number density is compared. The number density of bubbles would significantly increase the acoustic impedance of the fluid. This change in impedance is difficult to calculate accurately because the chaotic and dynamic two-phase environment in the test section. Figures 5.11, 5.12, and 5.13 which show the comparisons between number density, impedance ratio, and Sh imply that there is a correlation to high number densities with higher Sh for the PULST runs. This is in contrast to the low number density and low Sh for the SUMATRA experiment.

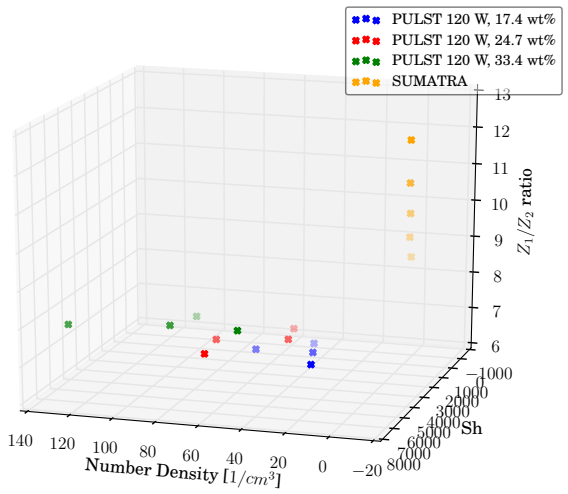

Figure 5.11: Comparison of Sh, number density, and acoustic impedance ratio for 1 120 W transducer.

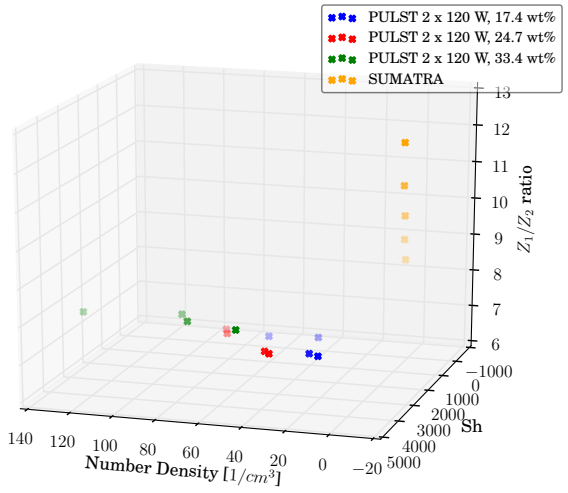

Figure 5.12: Comparison of Sh, number density, and acoustic impedance ratio for 2 120 W transducers.

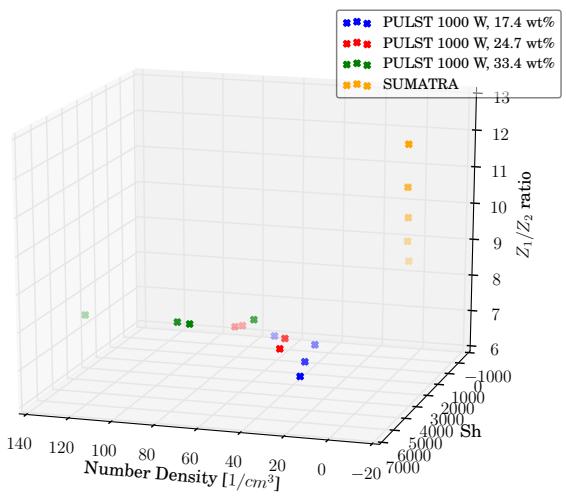

Figure 5.13: Comparison of Sh, number density, and acoustic impedance ratio for the 1000 W transducer.

The data suggest that the difference in mass transfer performance of the SUMATRA and PULST experiments is the difference in the acoustic intensity transfer to the fluids. One way to increase the transfer of acoustic intensity to the fluid inside the PULST test section is to add a matching layer. This layer would maximize the transfer of acoustic energy across two media that have significantly different acoustic impedances. In the case of the PUSLT experiment, the two media are aluminum and water/glycerol. The transfer of intensity across the matching layer is compared to the applied intensity of the SUMATRA experiment. There is significant variance of applied intensity, on the order of 200 W/cm^2, between these two experiments as shown in Figure 5.14. But, comparing the calculated intensity transmitted through a matching layer for the PULST experiment and the intensity transmitted to the fluid in the SUMATRA experiment as shown in Figure 5.15, the difference is much smaller, on the order of 35 W/cm^2. Testing this with the current PULST experi-

ment is beyond its current capabilities. Also, the PULST test section would have to be redesigned in such a way that would be able to accommodate a matching layer (which would include a material search), and minimize transmission losses due to the test section geometry. The other major factor for acoustic energy transmission is the number density of bubbles. As discussed earlier, higher number densities increase the acoustic impedance, and this can be seen in the data by the transmitted intensities dropping with relation to a higher number density as seen in Figure 5.16. The transmitted acoustic intensity was measured with a VP-3 Pinducer for both PULST horns, and the transmitted for the 120 W and 1 kW horn was on the order of 10^{-7} W/cm^2 to 10^{-9} W/cm^2. It is concluded that the number density of bubbles was too high in the PULST experiment contributing to lower intensity transfer, and subsequently lower mass transfer enhancement.

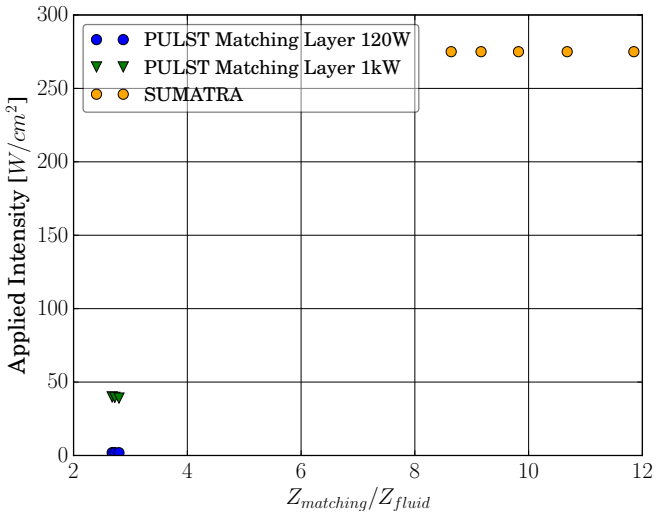

Figure 5.14: Applied intensity plotted on the matching layer impedance ratio for the PUSLT experiment compared to the SUMATRA applied intensity and impedance ratio.

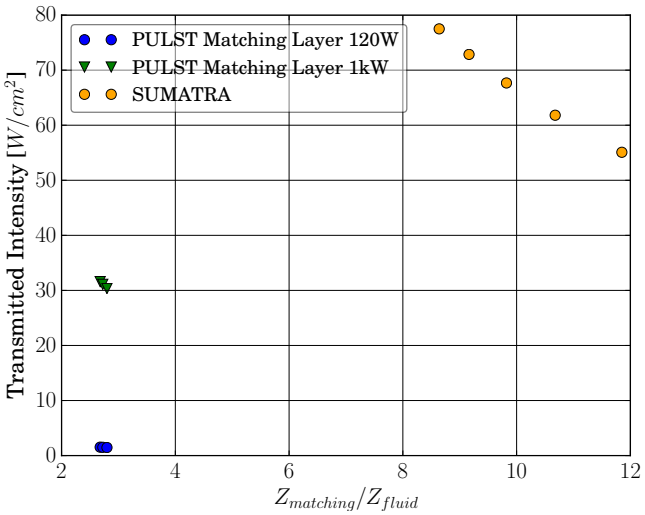

Figure 5.15: Calculated transmitted intensity for PULST assuming a matching layer is introduced compared to the calculated transmission of intensity in the SUMATRA experiment.

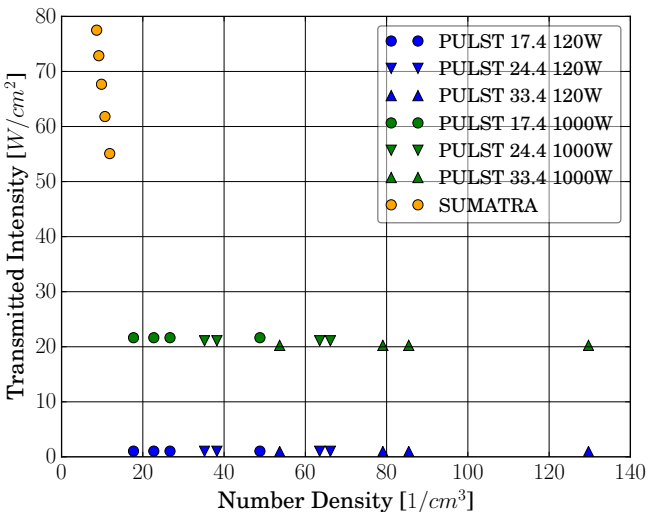

Figure 5.16: Number density and transmitted intensity comparison for the PULST and SMATRA experiments.

5.2 Comparison Study Findings

The parameter comparison study shows the PULST experiment differed from the SUMATRA experiment in significant ways. The differences lead to the inability to transmit high acoustic intensities through lower powered transducers. Acoustic energy was lost through the acoustic impedance ratios of aluminum and glycerol/water mixtures and the higher bubble densities. These were the main factors that prevented the enhancement of the two-phase mass transfer in the PULST experiment.

From this assessment, the modification that is needed with respect to transmitted acoustic intensity, is to add a matching layer and increase the intensity applied to the PULST experiment in order to get closer to the SUMATRA intensity. This should be done in conjunction with lowering the number density of injected bubbles. But, this is not the only factor that has to be addressed. There is one significant factor, which is difficult to quantify, is the horn/test section design. This comparison is ultimately comparing two different chemical reactor types, where SUMATRA is a horn type and the PULST is a bath type. In this comparison the advantages, disadvantages, and properties of both must be addressed when looking to modify the PULST experiment. This would lead to a decision to continue with the bath type reactor or to revert back to the probe type reactor. If the indirect bath type configuration is going to be used, there will be significant mass added to the horn/test section and a suitable matching layer material must be found.

Chapter 6

Conclusions

The two experiments reported in this dissertation investigated the viability and value of on ultrasonic enhancement of sparging mass transfer, in scaled experiments. SUMATRA showed that it is viable on the bench top scale and with direct sonication. PULST showed that the enhancement was inconclusive when the experiment was scaled up with indirect sonication. In order to understand the reasons that the PULST experiment did not show the same results as SUMATRA, a parameter study was performed and the conclusions of which show the boundaries of the design space for an sonomechancially enhanced mass transfer cell.

6.1 Summary of Work

The SUMATRA experiment was the first portion of this dissertation, and it had shown that the addition of high power ultrasonics can enhance the mass transfer performance. This was shown quite conclusively and successfully through a set of mass transfer experiments. Two main factors were essential in the experiments success, employing near-field interaction and acoustic transmission. The path to success

for SUMATRA is illustrated in Figure 6.1. The transmission of acoustic energy was easy and straight forward with the direct sonication. It allowed for the majority of the intensity to be applied to the fluid. Due to the small size of the experiment, the acoustic generation was also relatively simple where the VCX-750 was sufficient. Being able to utilize the near-field interactions was more complicated. The use of high intensities had shown a dramatically better performance. The low intensity with pulsing did show an improvement without erosion. The value of this information was overlooked at the time. Because the improvement was marginal, it was illustrated with a dotted line in Figure 6.1.

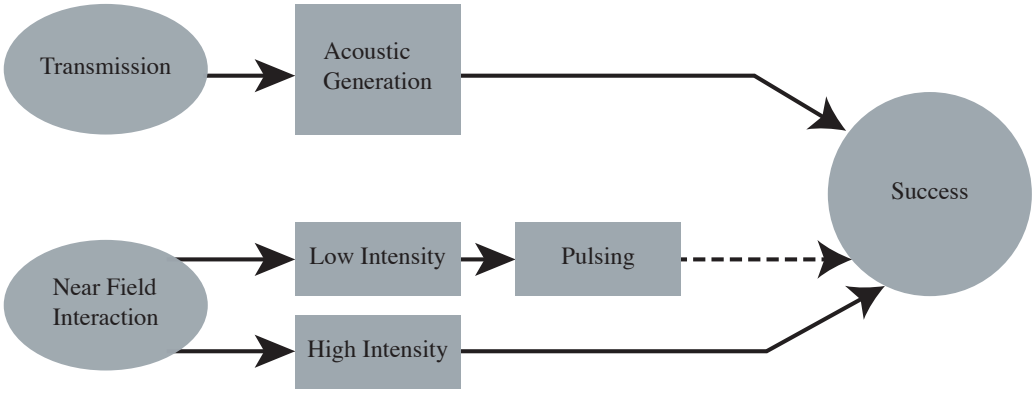

Figure 6.1: SUMATRA flow path for success.

The PULST experiment was a scaled up of the SUMATRA loop based on utilizing commercial-off-the-shelf components. It also varied in design in the manner that it applied ultrasonic power indirectly into the fluid. The intended goal was to demonstrate conclusive indication positive mass transfer enhancement, but the data showed an inconclusive (positive or negative) mass transfer enhancement given the engineering constraints. The path for success is illustrated in Figure 6.2. The dotted lines represent places where the data shows where improvements would be necessary.

The indirect sonication configuration added complexity to the acoustic transmission. The parameter comparison in Chapter 5 showed that the horn geometry, horn

material, and acoustic generation are intimately tied. An optimized horn geometry must incorporate the test section in its design and power considerations. Because of the extra mass to consider, significantly more acoustic power would be needed. Also, to maximize the acoustic energy transfer through the test section should incorporate a quarter wavelength matching layer.

Flow control was a factor that was added. SUMATRA runs were all performed at a fixed flow rate of 15.14 LPM (4 GPM) and therefore, the glycerol concentration controlled Re. In contrast to PUSLT, both flow and concentration was a factor in the Re. This lead to a couple important observations about bubble size and removal efficiency. The average bubble size was proportional to both flow rate and glycerol concentration. This lead to a dependence on Re and d in the Sh correlations. In order to decouple these parameters, a custom bubble injection system which can adjust the average size of the injected bubbles must be utilized. The difficult task of bubble removal was attempted here by implementing the TACO 4900 separators which use pall rings as the key component. They did satisfactorily separate bubbles with the lower flows and larger bubble sizes, but not with the higher flows and smaller bubbles. Finally, there was a significant effect of bubbles on the acoustic intensity inside of the test section. It was noted in the comparison study in Chapter 5, that the SUMATRA bubble densities were much smaller than the PULST bubble densities. Subsequently, the higher bubble densities acted like a bubble curtain, which attenuated much of the acoustic energy. The insights taken from the PULST experiment are to lower the bubble density, devise a bubble injector that can tune bubble diameter, and find a reliable bubble removal solution.

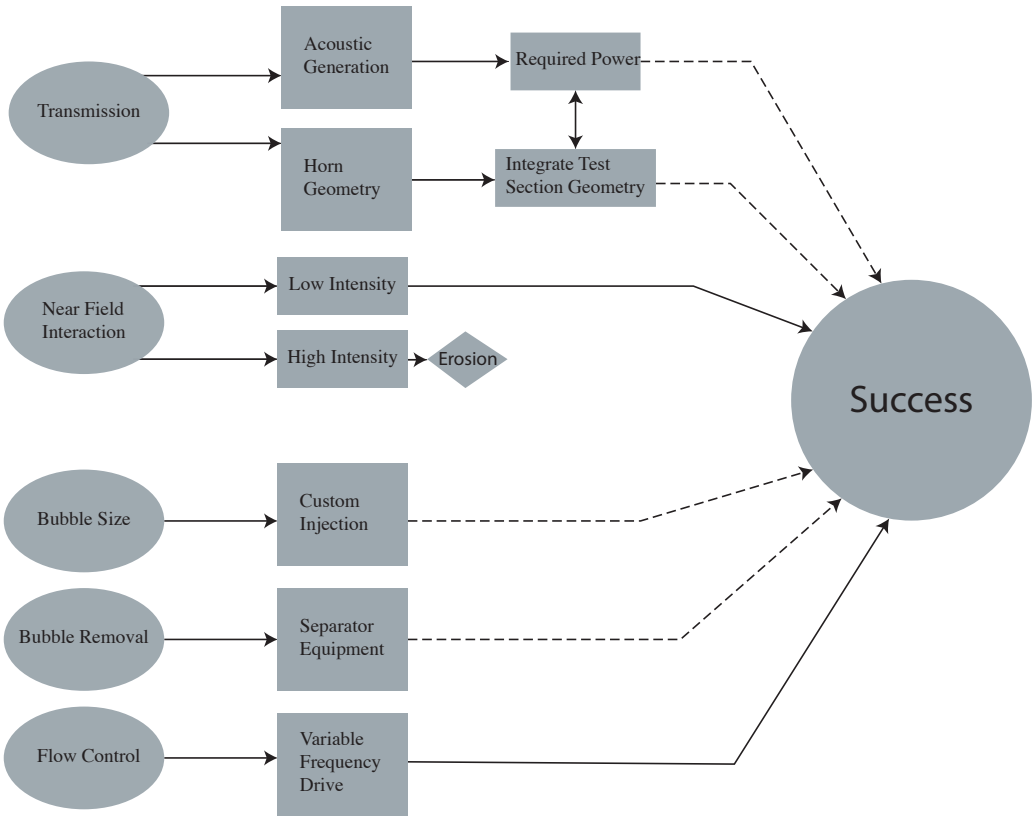

Figure 6.2: PULST flow path for success.

6.2 Future Work

The next steps for this work would branch into two experimental directions. The first direction will be to continue to investigate the low power indirect sonication route. As shown in Figure 6.2, addressing the factors represented by the dotted lines would be the most immediate considerations. The ultrasonic designs would have to be optimized, specifically by utilizing and designing for quarter wavelength impedance matching layers to maximize ultrasonic power transmission. Next parameter to be optimized would be the bubble size, bubble density, and bubble removal. The bubble size was addressed at by Kress [20] with a custom built bubble injector with the ability

to tune bubble size. A design approach can be utilized in a later iteration of this investigation with the added capability to deliver a consistent bubble density similar to the SUMATRA experiment. In addressing the bubble removal challenge, current work at the Chinese Academy of Science addressing the bubble removal problem through air core formation [67] could possible be utilized. In parallel, off-the-shelf bubble removal techniques can be investigated for this purpose. There are many industries where gas removal is important and has been solved, and some of these solutions have the potential to be integrated into the tritium removal solution.

The other direction this investigation can go is the direct sonication configuration. This significantly simplifies the challenge, but due horn tip erosion, high intensities are not worth the trade off. The results shown in Section 3.3 demonstrate a small increase in mass transfer performance with applying pulsed low intensity ultrasonics without significant erosion on the horn tip. The next steps would be to test if this effect were additive and if it could be scaled up past a bench top test.

Future effort should be focused on further developing the acoustic bubble mass transfer models developed in Section 3.4. In conjunction with the theoretical development, fundamental experiments should be performed to investigate, validate, and inform the theoretical efforts.

One design tool that was not leveraged in this dissertation was the use of modeling and simulation. Due to the highly chaotic nature of ultrasonics coupled with two-phase mass transfer, an experimental approach was taken. Simulations using CFD have been done comparing mass transfer enhancements due to ultrasonics [68, 69, 70]. When studies like these can be benchmarked and validated with commensurate experimental data, this can be a powerful design tool for sonoenhanced sparging cells and sonochemical reactors.

This study has identified several major challenges that need to be addressed using

appropriate scaled experiments before any implementation on a larger scale or with tritium. These include how to effectively impart acoustic energy of an appropriate intensity into the process stream without introducing wear and erosion products into the reactor flibe. One key challenge for the ultrasonic component is to find a piezoelectric material in the ultrasonic transducers that can survive a radiation field and high temperature environment. There is ongoing work by other groups that may potentially be leveraged to address the transducer requirements in a radiation environment. [71, 72, 73, 74, 75].

Appendices

Appendix A

Glycerol/Water Viscosity Calculation

The dynamic viscosity (μ) for water/glycerol calculations are taken from Cheng, ref [76]. The viscosity of the two component system is related through a power form shown in (A.1), where α is defined by equations (A.2), (A.3), and (A.4).

$$\mu = \mu_w \mu_g^{(1-\alpha)} \tag{A.1}$$

$$\alpha = 1 - C_m + \frac{abC_m(1-C_m)}{aC_m + b(1-Cm)} \tag{A.2}$$

$$a = 0.705 - 0.0017T \tag{A.3}$$

$$b = (4.9 + 0.036T)a^{2.5} \tag{A.4}$$

The component dynamic viscosities for water (μ_w) and glycerol (μ_g) are shown in the following equations (A.5) and (A.6), respectively.

$$\mu_w = 1.790 \exp\left(\frac{(-1230 - T)T}{36100 + 360T}\right) \tag{A.5}$$

$$\mu_g = 12100 \exp\left(\frac{(-1233 + T)T}{9900 + 70T}\right) \tag{A.6}$$

In order to complete the calculation for kinematic viscosity, the densities for water and glycerol are calculated using equations (A.7) and (A.8), respectively. The combined density would be calculated using a simple weighted average of water and glycerol.

$$\rho_w = 1000\left(1 - \left|\frac{T-4}{622}\right|^{1.7}\right) \tag{A.7}$$

$$\rho_g = 1227 - 0.654T \tag{A.8}$$

Appendix B

PUSLT Test Section Drawings

B.1 First Test Section

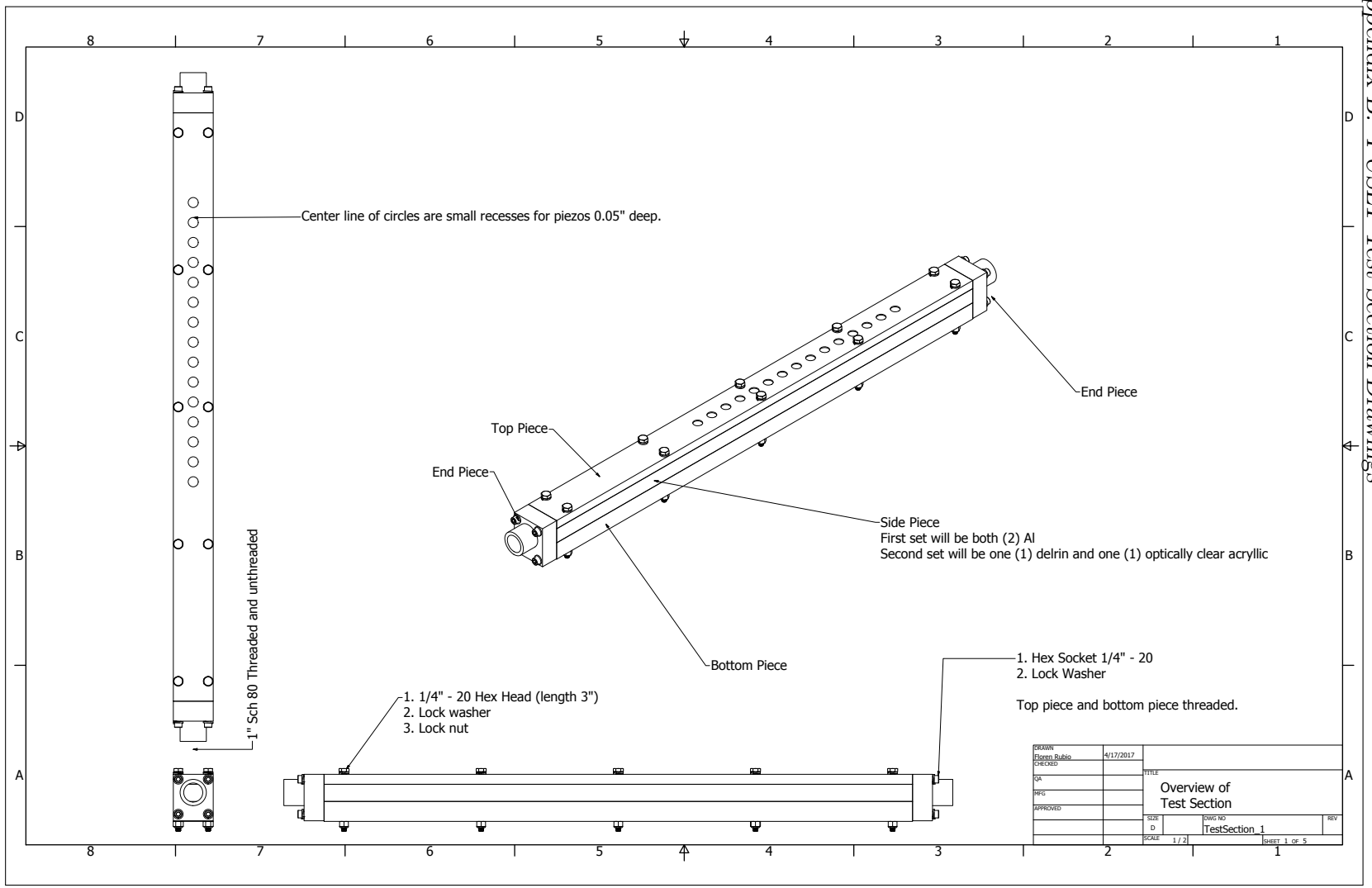

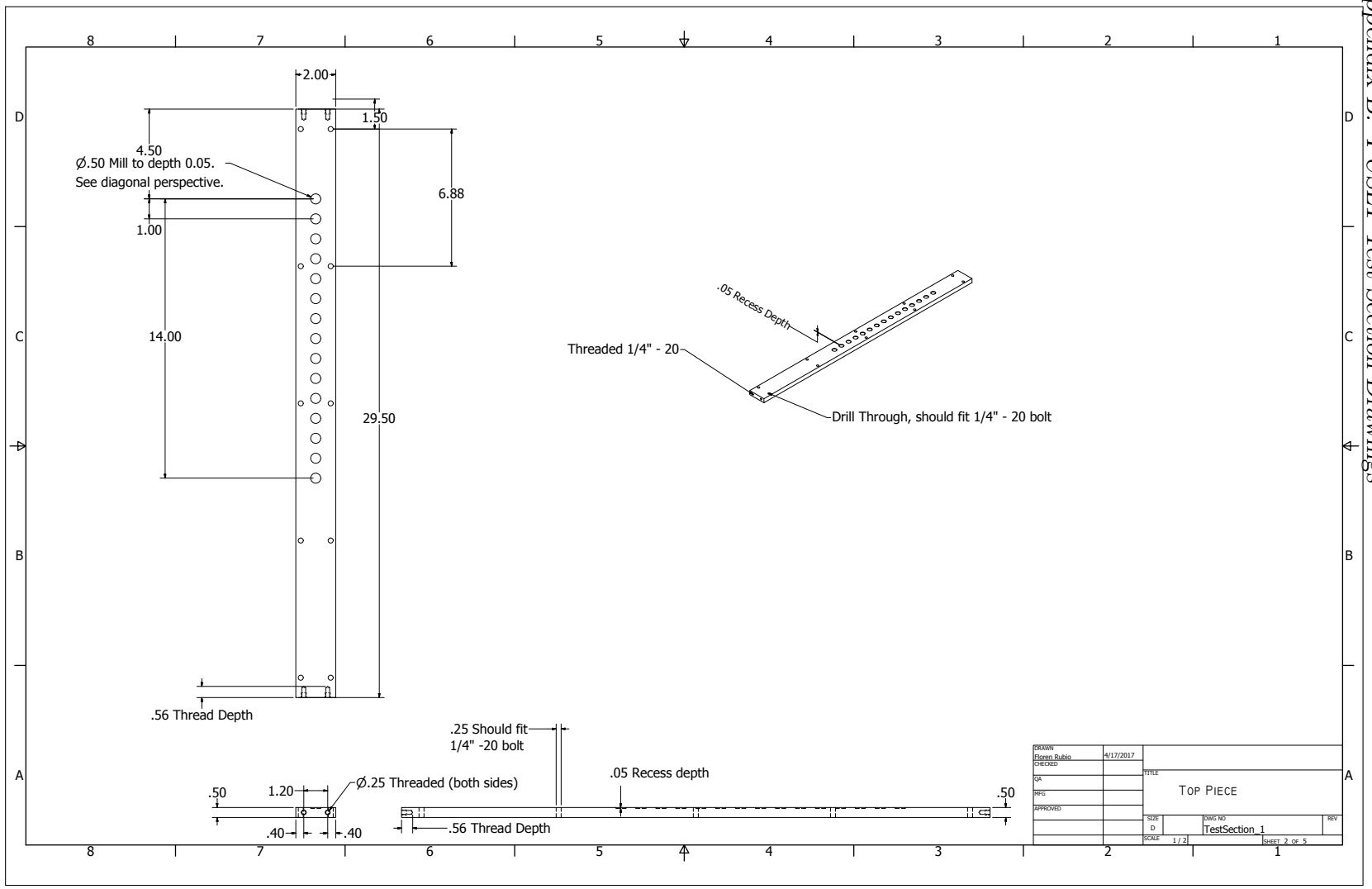

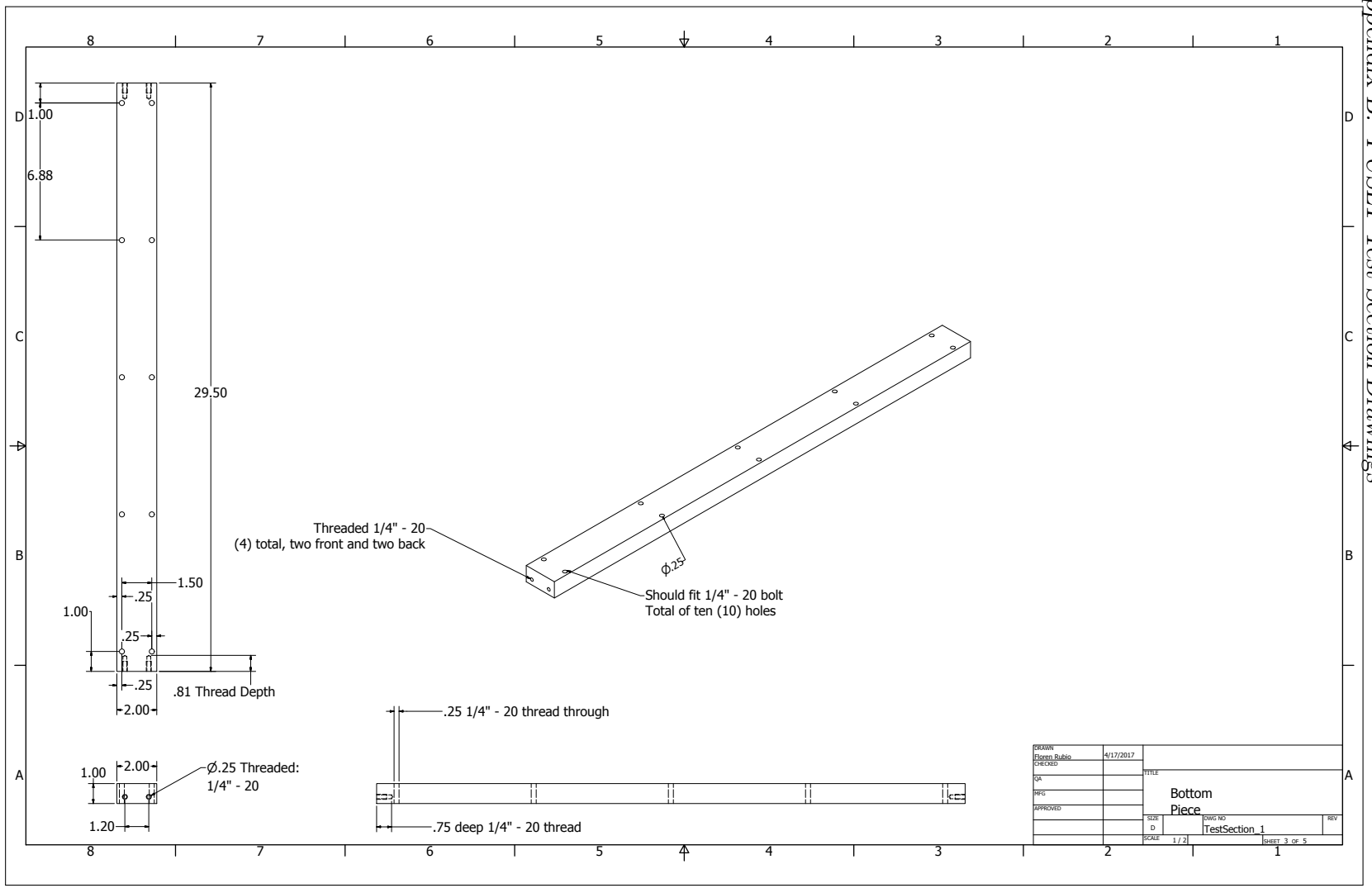

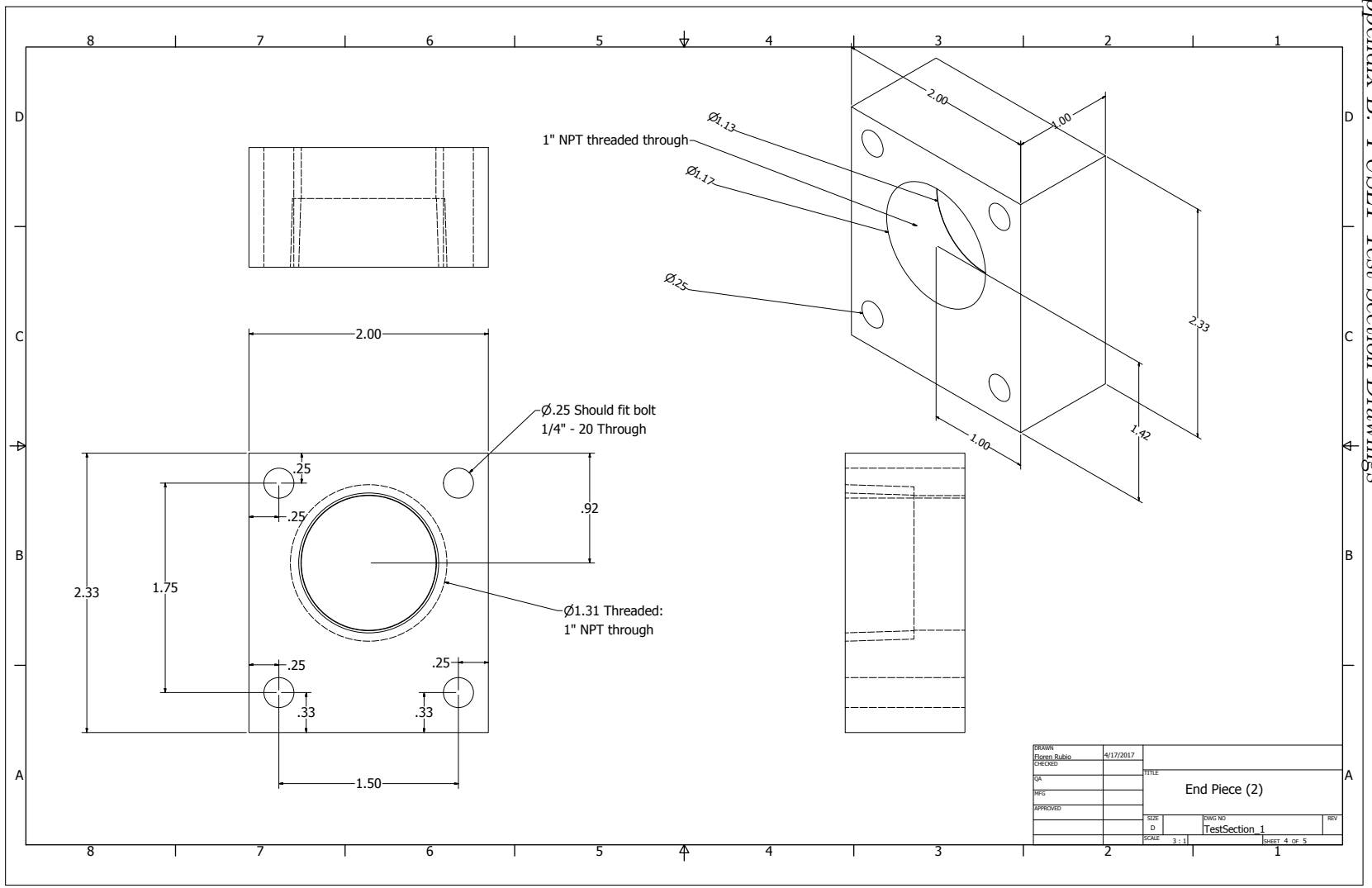

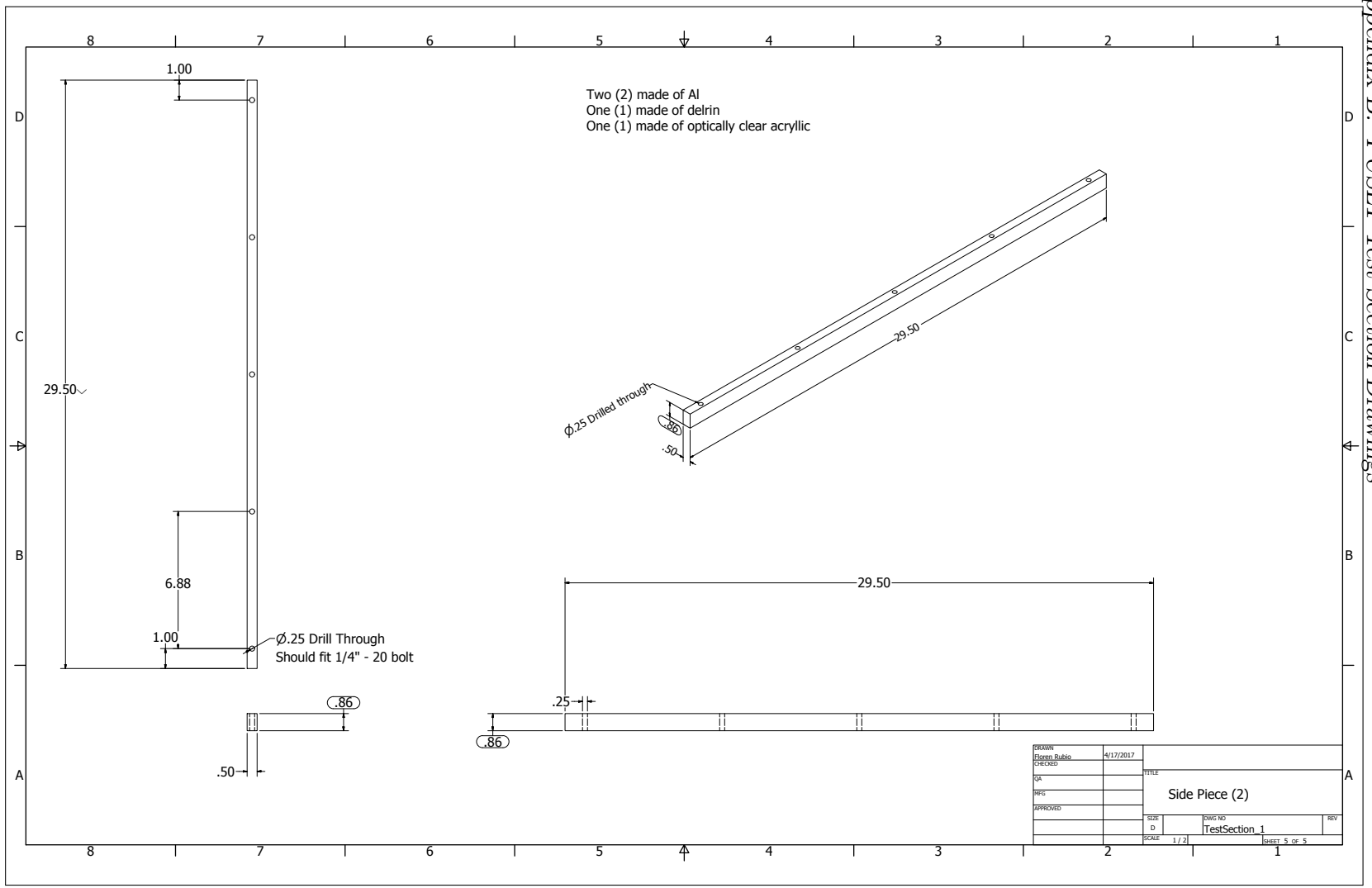

B.2 Second Test Section (Unfabricated)

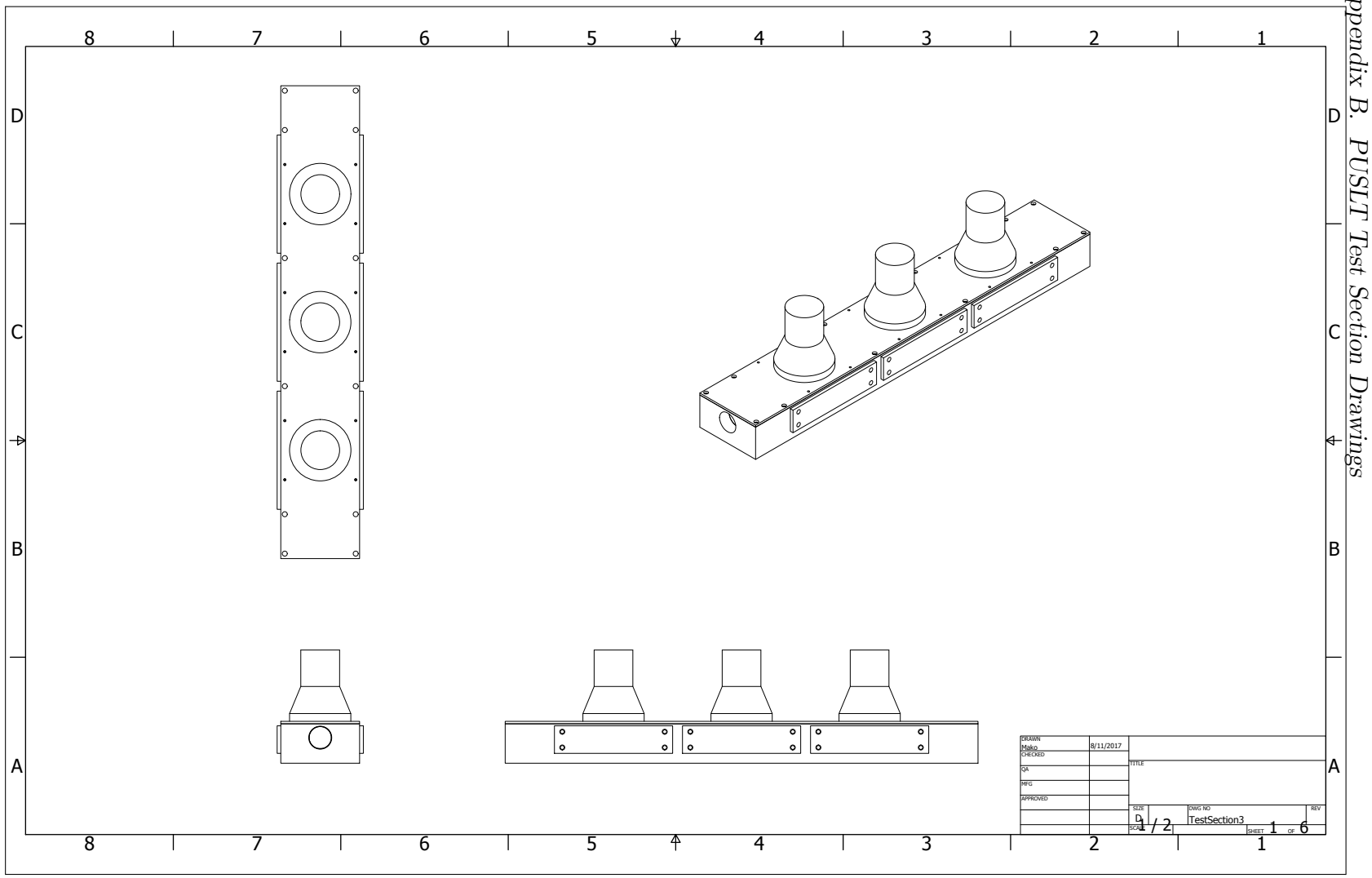

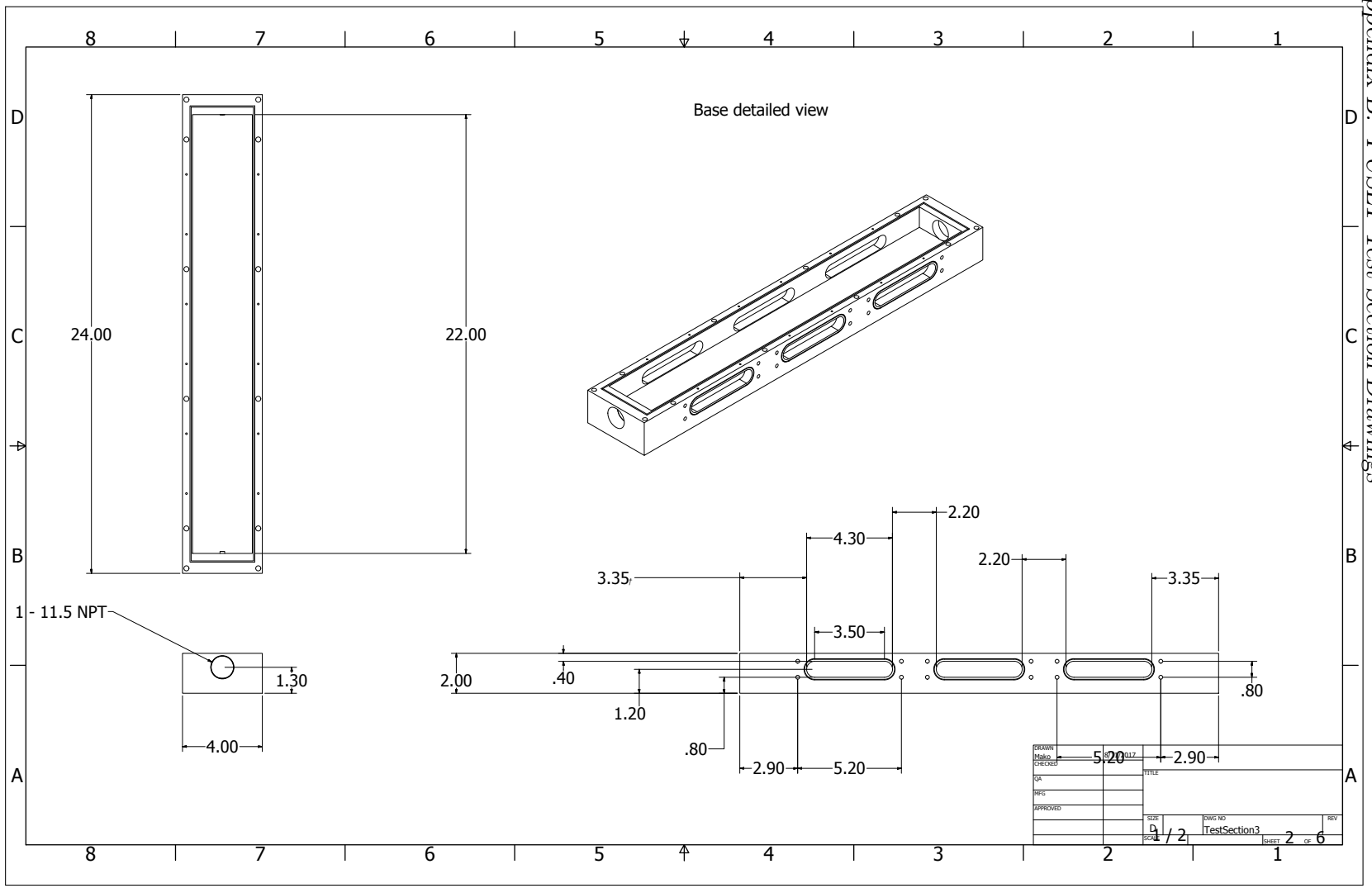

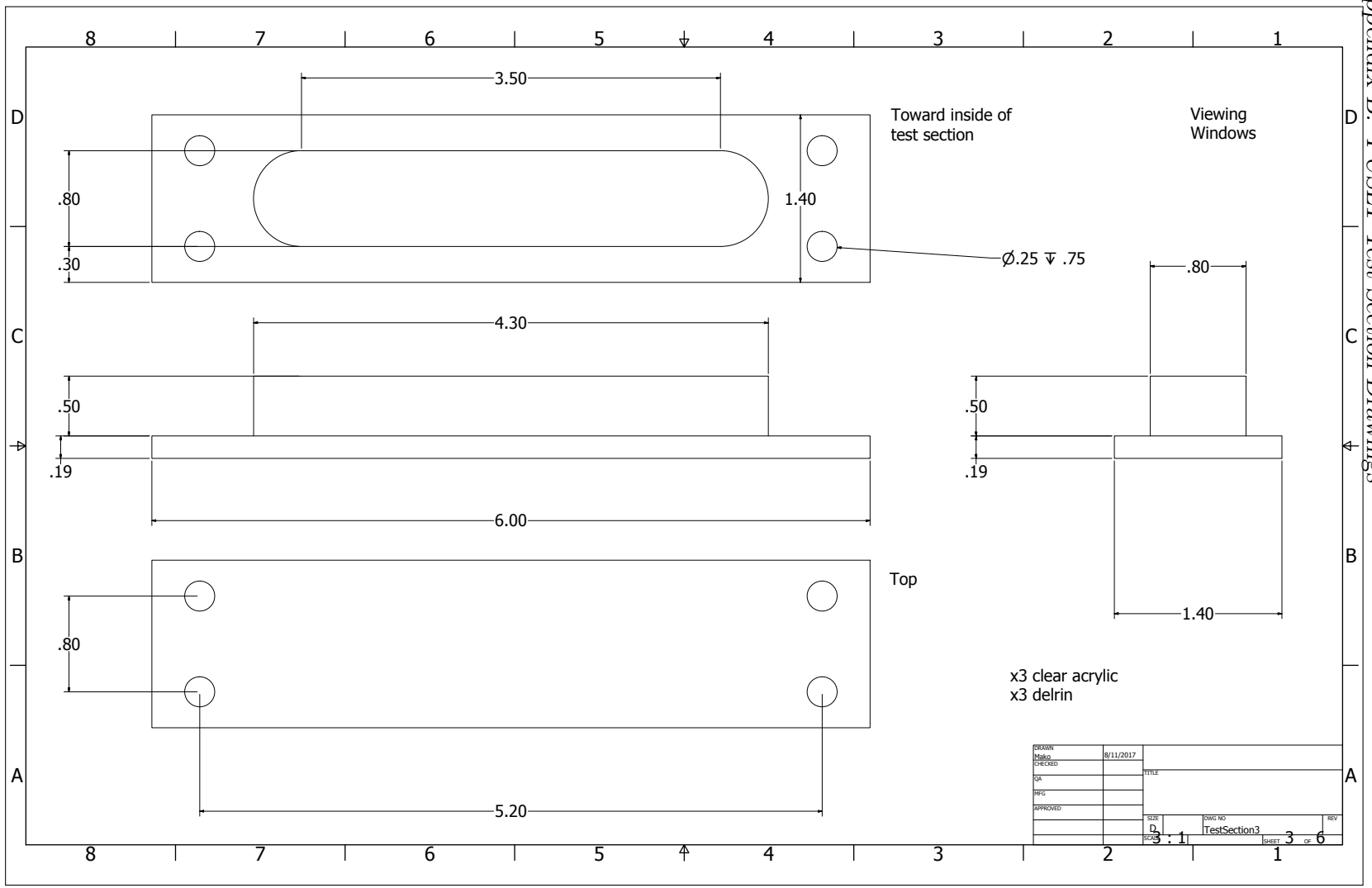

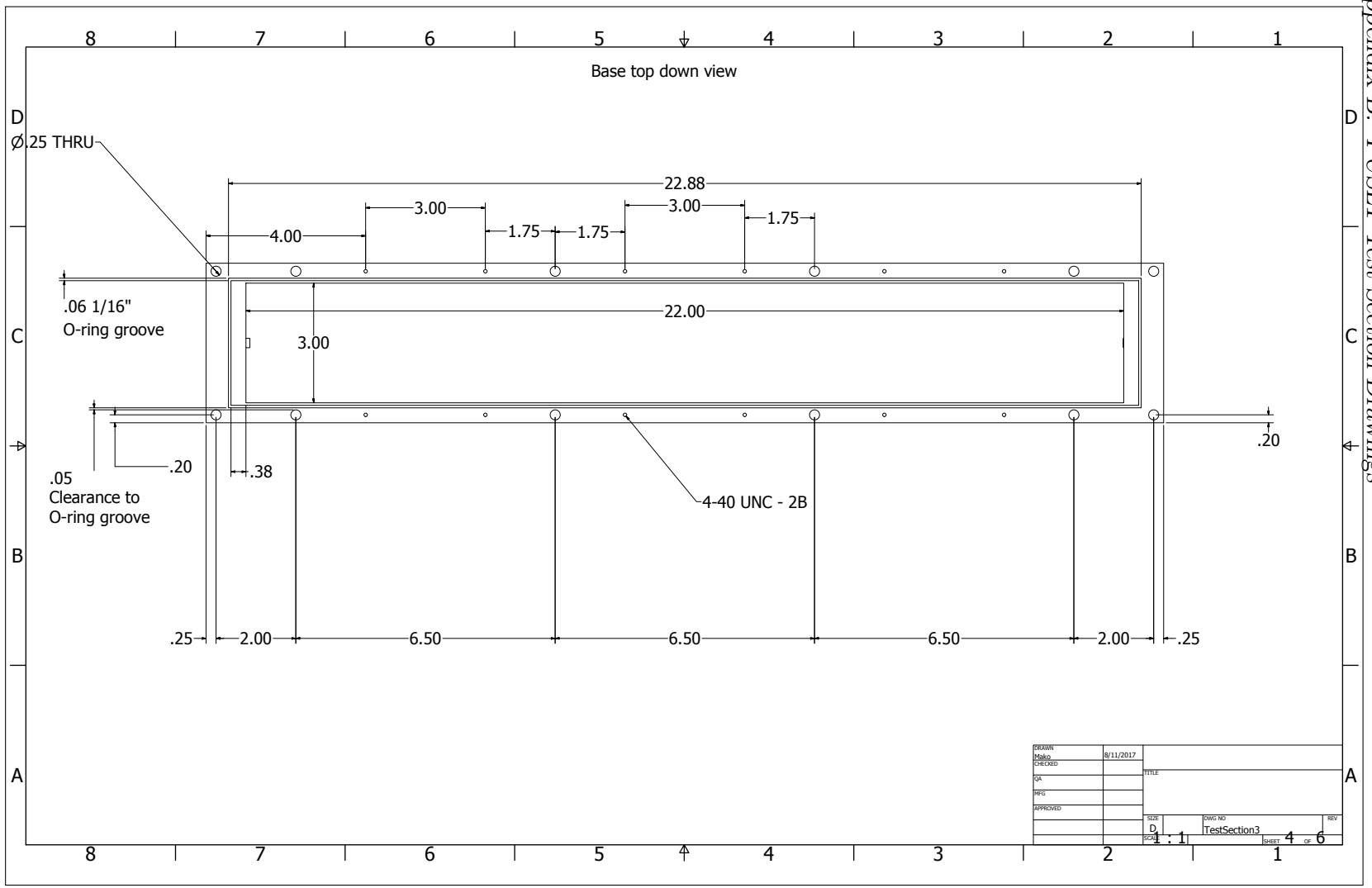

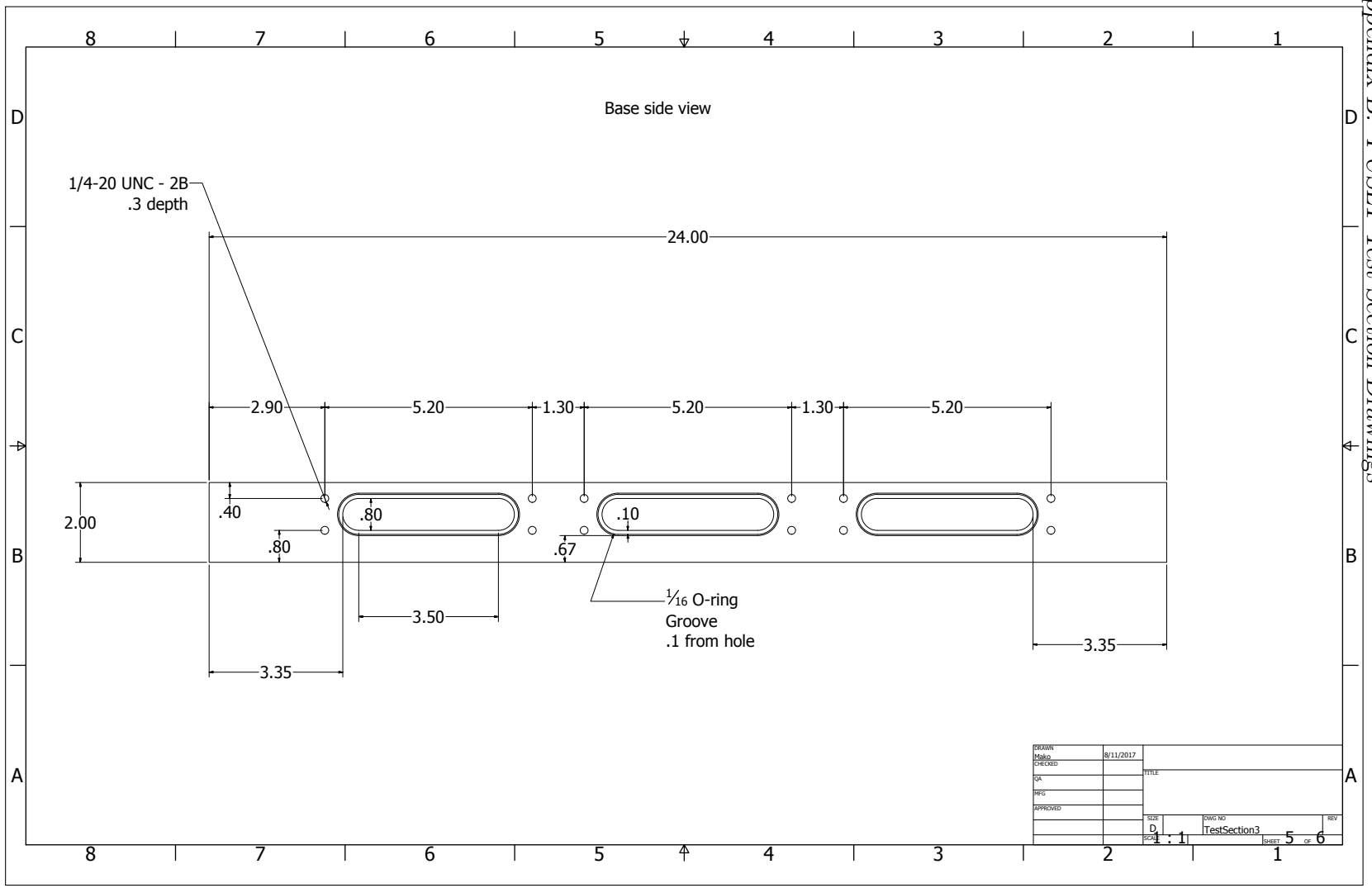

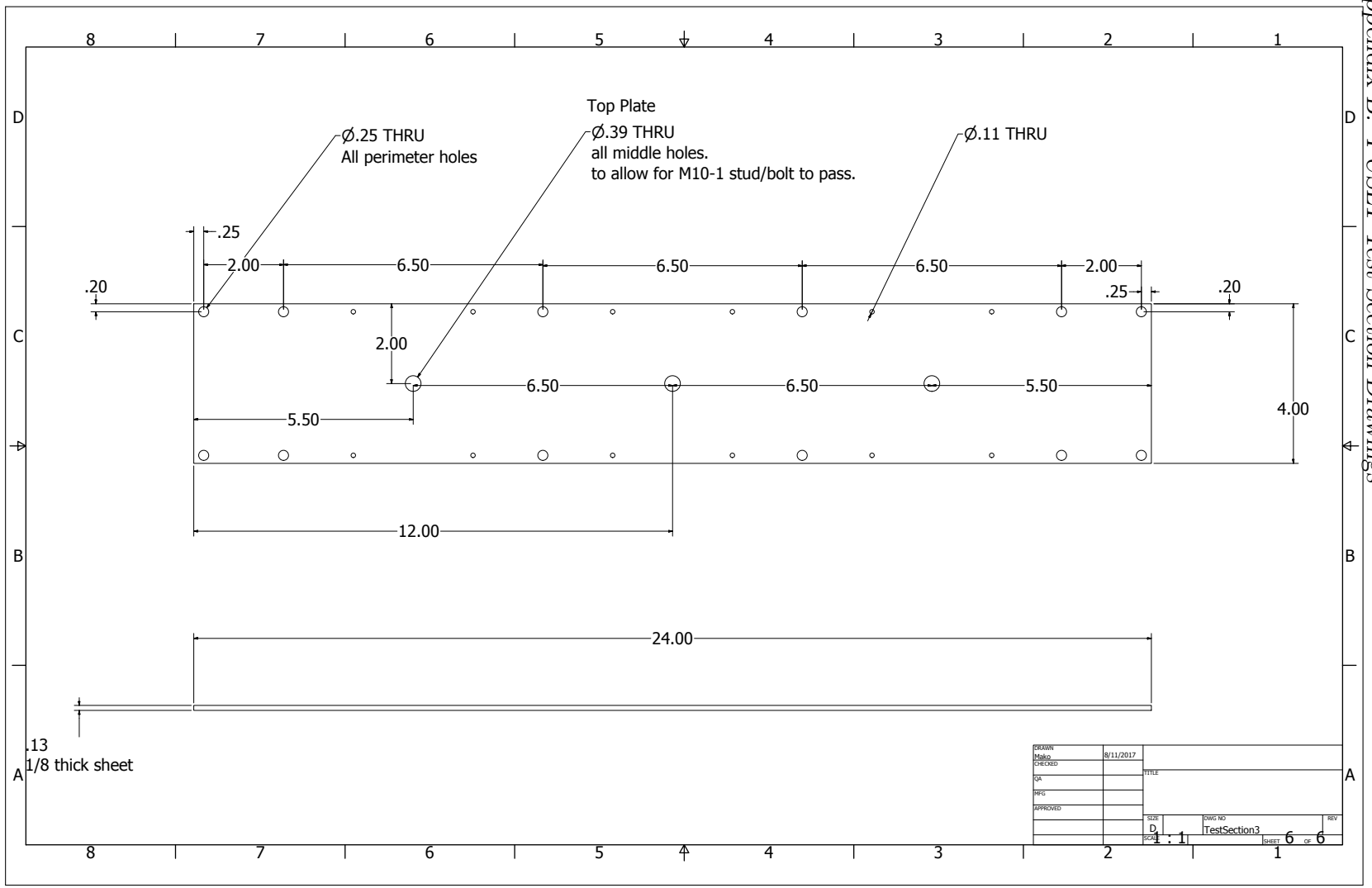

B.3 Third Test Section (Modular)

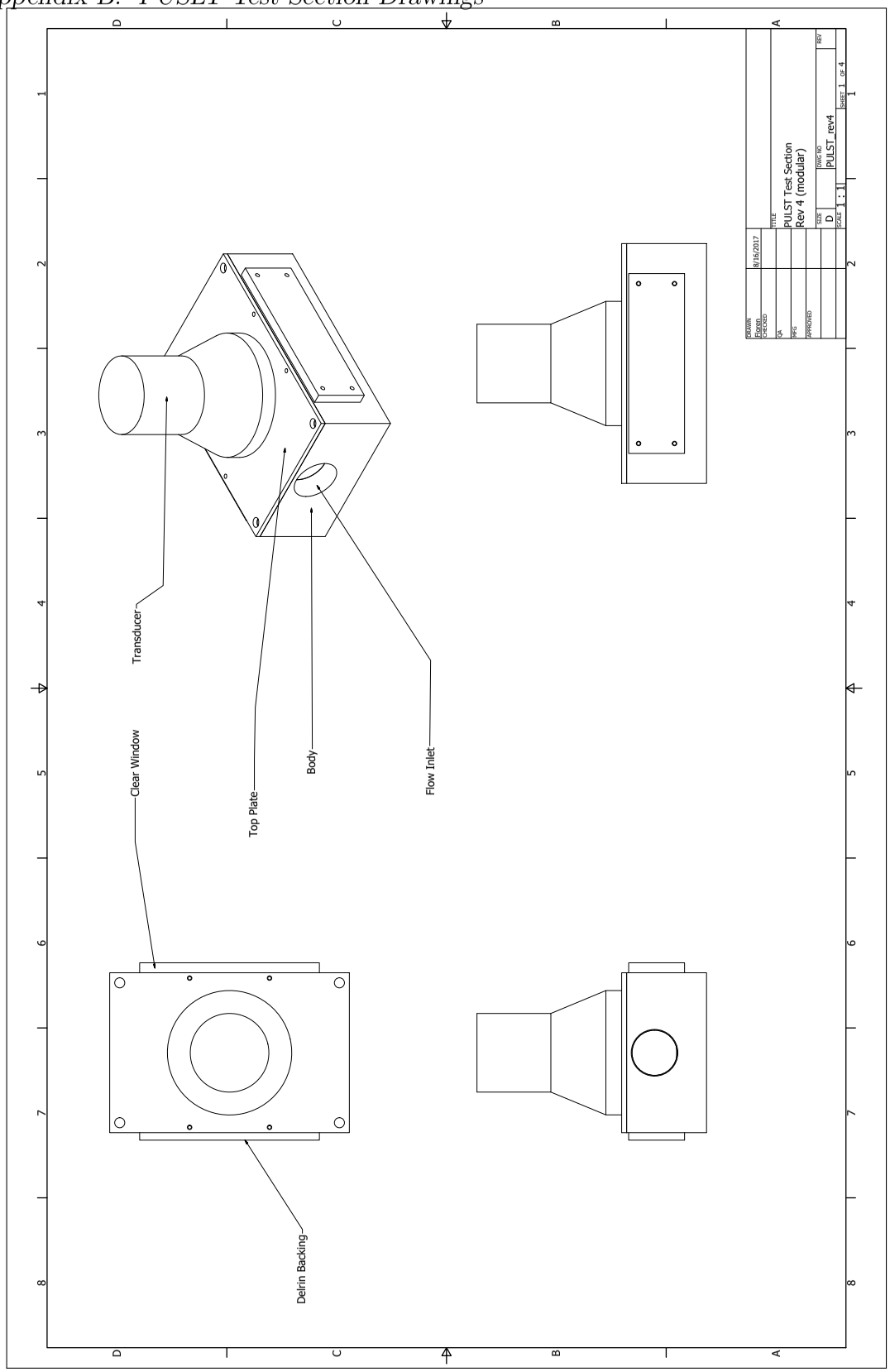

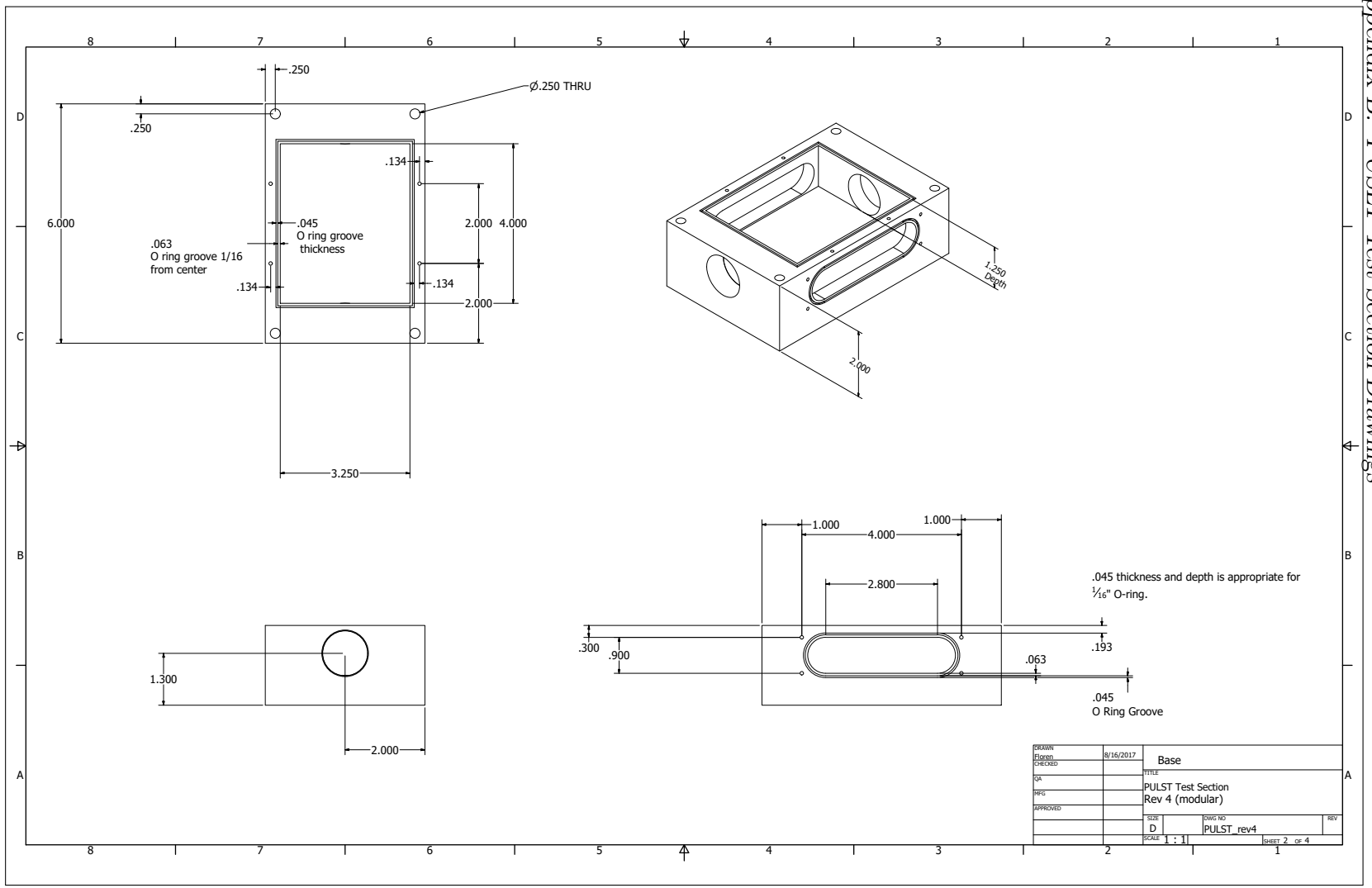

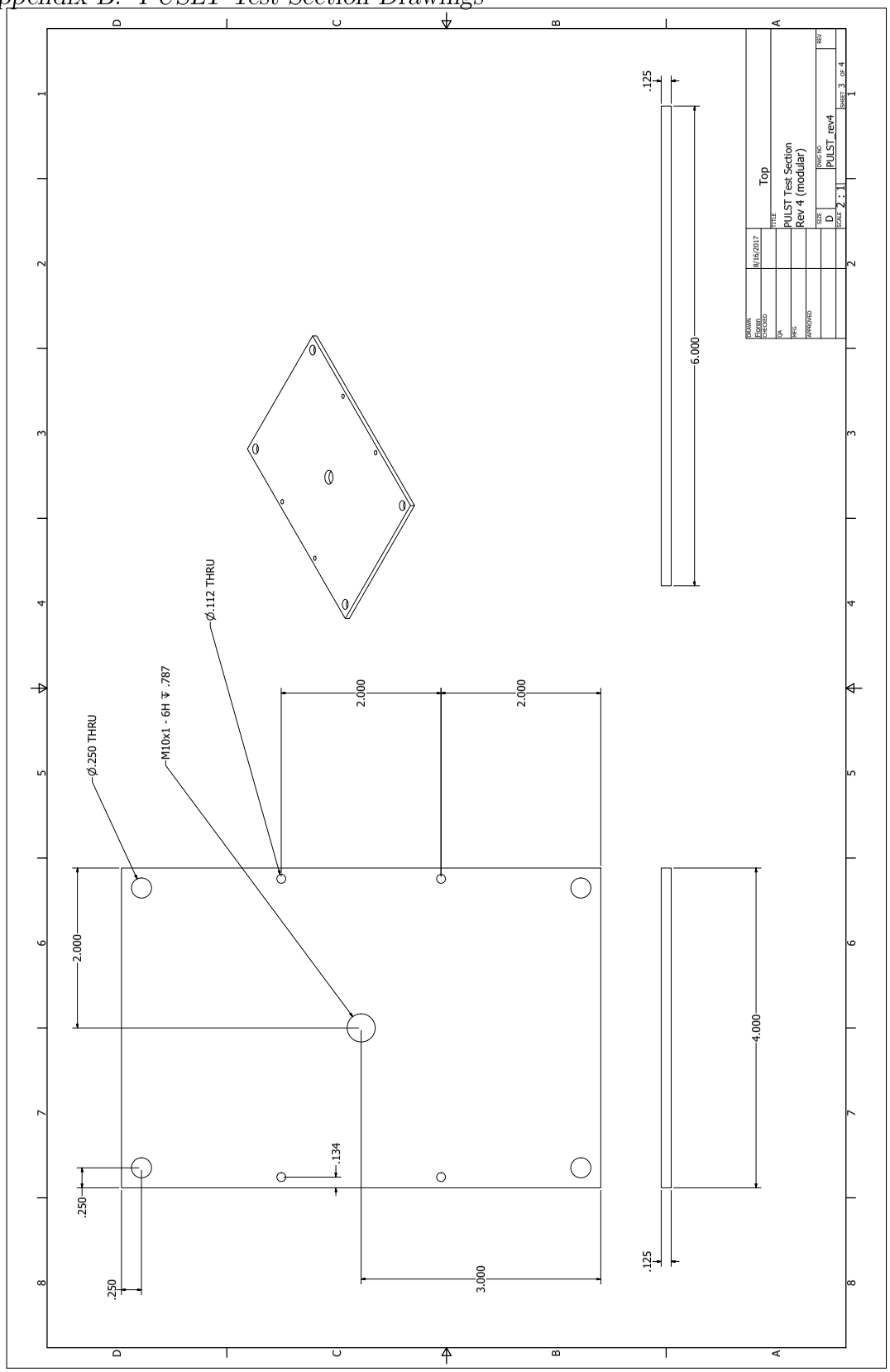

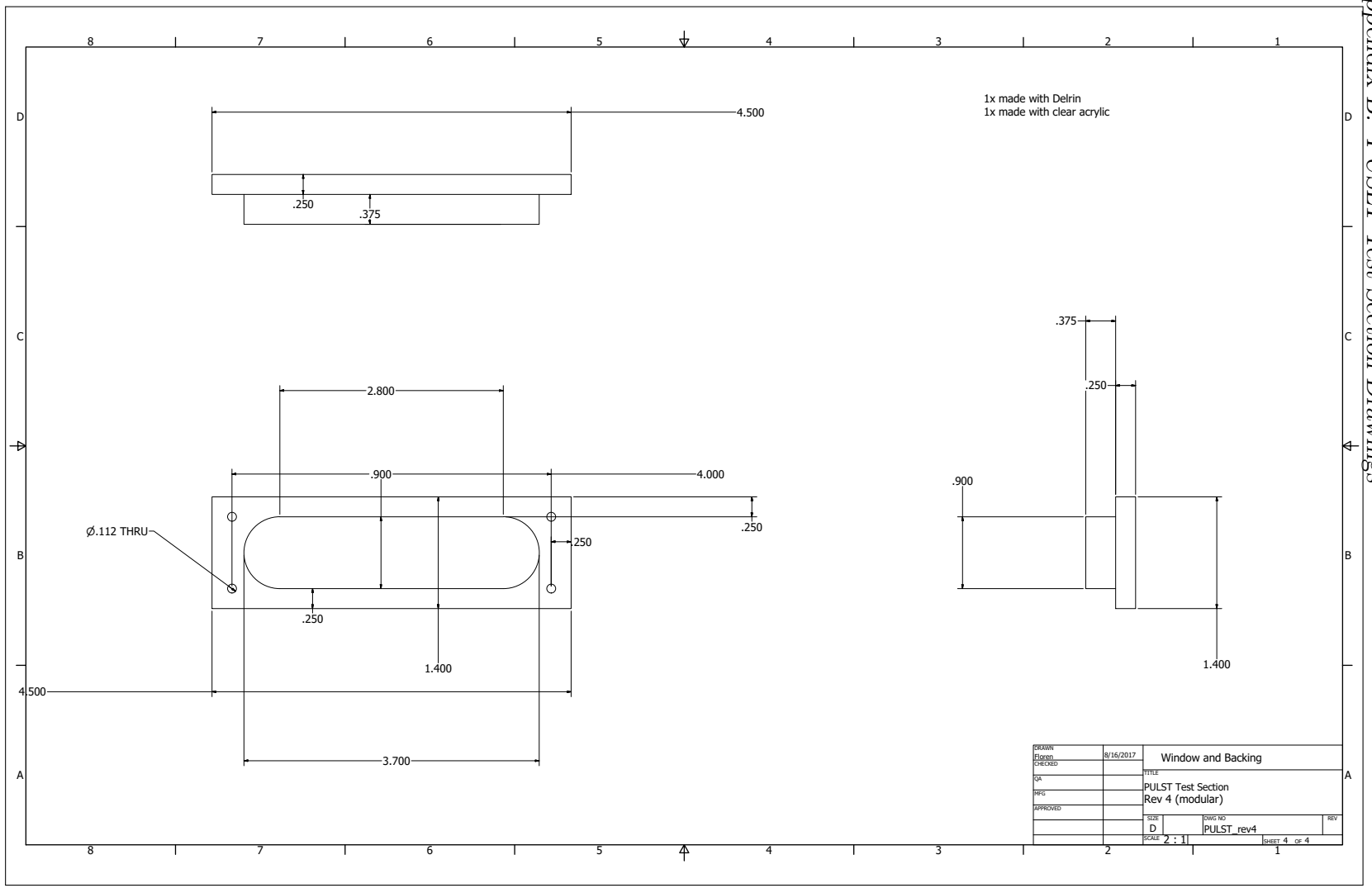

Appendix C

PULST Operational Procedure

PULST Loop Ultrasonic Data Taking
Version 1.21

Test Number _____

Glycerol Concentration _____

Target Re _____

Flow Rate _____

Number of Transducers _____

SAFETY NOTE:
Wear appropriate PPE's - Hearing protection (over ear muffs or ear plugs).
NEVER touch the ultrasonic transducers while they are energized.
Monitor leaks on the test section for leaks that can get onto the transducers. If transducers get wet, shutdown the experiment and address the leak.

Startup Checklist

- ☐ Ensure the Signal Generator, Oscilloscope, and Ultrasoinc Amplifier are connected.
- ☐ Remove the cover from the DO probe and install the top.
- ☐ Bring up the latest LabView vi (PULST_DAQ.vi) and DO meter software on the lab computer.
- ☐ Rinse out Fill Tank
- ☐ Check the initial valve lineup.
  - ☐ V-1 (Fill Suction Valve) SHUT
  - ☐ V-2 (Drain Valve) SHUT
  - ☐ V-3 (Tank Valve) SHUT
- ☐ Rinse out Fill Tank with hose.

Startup Procedure

- ☐ Start the Chiller
- ☐ Mix glycerol/water mixture using the freight scale.
  _____ Note mixture concentration in $wt\%$
- ☐ Put mixture in Fill Tank and ensure it is mixed well.
- ☐ OPEN V-3 (Fill Tank Valve) and wait until level stops moving.
- ☐ Start pump at about $30\ hz$ and begin filling the loop.
- ☐ SHUT V-3 (Fill Tank Valve) and OPEN V-1 (Fill Suction Valve) when Expansion Tank Level is at a visible level.
- ☐ Check system response. It should be flowing well and bubbles are being actively removed.
- ☐ (Turn ON the DO meter if necessary) Start the DO meter software.
- ☐ Begin injecting air with 3-way valve to saturate the fluid with oxygen.
- ☐ Ensure that the DO probe is submerged by venting with V-4
- ☐ Watch temperature on the LabView Program.
- ☐ Set pump to the desired flow rate
  _____ Flow Rate (GPM)
  _____ Re
  _____ Pump Frequency (hz)

- ☐ When loop is at the desired temperature and oxygen saturated, the loop is ready to take data.

1

INITIALS: _____
DATE: _____

Data Taking

☐ START logging data on the LabView Program.
☐ STOP air injection and wait until all (or most) residual bubbles are removed.
☐ START logging DO meter data (DO and temperature).
☐ START injecting Argon.
_____ Gas Flow Rate ($SCFM$)
☐ WAIT until DO concentration reaches target concentration of $2.9\ mg/L$
☐ SWITCH from injection Ar to air and saturate with oxygen.
☐ Stop air injection by putting 3-way valve to SHUT and wait until all bubbles are removed
☐ Switch 3-way valve to Argon.
START ULTRASONIC PORTION

☐ Check the rack power is on.
☐ Set Signal Generator Frequency
☐ With only the Signal Generator ON, set the Frequency to $20.36 \pm .1\ hz$
☐ Turn DC output all the way down.
☐ Turn on DC 600
☐ Turn on KC N15-1 and note that the AC Volts is 0.
☐ Turn on (check on) oscilloscope.
Next step requires hearing protection.
☐ SLOWLY increase the DC output on the Signal Generator note:
☐ Compare voltage between the front panel of the KC N15-1 and oscilloscope.
☐ Set output to as close to BUT NOT OVER $400\ V$.
Also, check to see if TC and Oxygen Meter readings still work. If they are affected, lower power to where they are not affected.
☐ Ensure that the transducers are working by looking at the test section.
☐ DO NOT TOUCH TEST SECTION OR TRANSDUCERS AT THIS POINT.
It can cavitate your tissue and it is a shock hazard.
☐ WAIT until DO concentration reaches target concentration of $2.9\ mg/L$
☐ While waiting, note Current and Voltage.
_____ Vrms (V)
_____ Current (A)
_____ Power (kW)

☐ TURN OFF the Signal Generator and TURN DOWN the output.
☐ TURN OFF KC N15-1 and DC 600 in that order.
☐ STOP recording DO data and SAVE the DO file in the DropBox under the name format:
TEST_NUMBER_DO_##_YY_MM_DD.csv
☐ Save the LabView file in the DropBox under the name format:
TEST_NUMBER_Flow_##_YY_MM_DD.csv
☐ REPEAT data taking procedure or continue to Shutdown section.

NOTES:

INITIALS: _____
DATE: _____

Shutdown

- ☐ **STOP the pump**
- ☐ **OPEN (crack OPEN) V-2 (Loop Drain Valve) and empty loop.**
- ☐ **RINSE the loop 2 or 3 times using the appropriate portions of the Startup Procedure.**
- ☐ **RINSE the Fill Tank**
- ☐ **Cap the DO Probe:**
  - ☐ With the loop drained, Disconnect the probe from the meter.
  - ☐ Uninstall the DO probe
  - ☐ Cap Probe

HAZARDS

1. High acoustic energy hazards when in operation: transducers and test section - DO NOT TOUCH!

2. Shock hazard when in operation: Ultrasonic transducers will have up to $500\ V$ across the leads.

3. Slippery surfaces can exist when spills are present - always be aware of your surroundings.

4. Eye protection with non-removable side shields required at all times within laboratory: fixed objects can hit your face, power tools eject chips, and chemical spills/sprays can all cause damage to your eyes.

5. No food or drink in the lab at any time.

ADDITIONAL NOTES:

INITIALS: _____
DATE: _____

PULST Loop Ultrasonic Data Sheet
Version 3

Test Number(s) _____ _____ _____

Transducer Power _____

Target Re _____

Glycerol Concentration			
Re			
Flow Rate			
Pump Freq			
Gas Flow Rate			
Voltage			
Current			
Power			

NOTES:

INITIALS: _____
DATE: _____

Appendix D

Bubble Number Density Determination

The number density for the calculation of a was performed using the high speed camera and imageJ software. Due to the limitations of high speed camera and lens, direct measurement of the bubbles to establish a sauter mean diameter was not possible. Also, due to the way that bubbles were captured by the camera, software programs were unable to distinguish between bubble and background. As shown in the sample picture, the bubbles in a frame were too blurry, some were eclipsed by other bubbles, and many were just too small to be resolved. To get around this, the following method of analysis was devised.

This method consisted of directly counting each bubble in a given area. This would rely on the human eye being good at picking up patterns as well as movement. A video of 5000 frames was taken and in those frames, a frame was selected where counting would be relatively easy. This means that there were few bubble clusters, eclipsed bubbles, and a majority of bubbles were in good focus. While counting the bubbles on a still frame, the video was played back to confirm the counting of a

bubble.

The counting of the bubbles were done using ImageJ's "Particle Analysis" tool. The "counting" was tallied by making a mark on the frame on each perceived bubble in the area of interest on the frame. Once all the bubbles in the frame were "ticked", the threshold tool was used to wash out the background figure and the particle analysis was used to count all of the tally marks. In order to get the area of the picture, the known measurement length was the width of the channel (0.86 in / 2.18 cm). ImageJ has an area measurement tool to measure area. Since the depth of the channel is known (1 in/2.54 cm), the number density can be calculated. This method is visually described in Figure D.1.

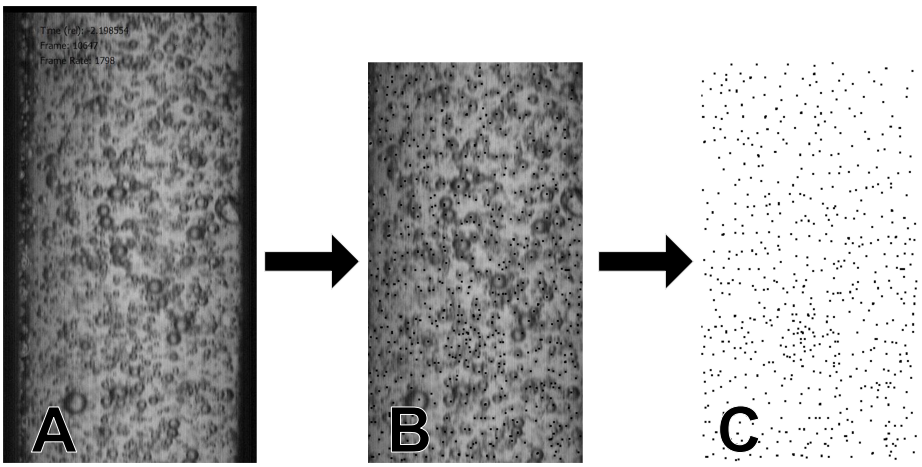

Figure D.1: Example of the bubble counting method. Picture A is the image from the high speed camera. Picture B shows the selection from A where bubbles were tallied with the marking tool. Picture C shows the background removed with only the "tallies" displayed and ready to be counted with ImageJ.

This technique does come with some drawbacks. It is quite time consuming to perform one count, so this can limit the number of total counts. Because each count is a snapshot of flow, multiple counts must be taken. To get a quantifiable measure of the accuracy of the number density, the counts were taken until the standard error was below 2.5 $/cm^2$. Another artifact of this measure is selection bias. Because

the frames were selected for "ease of counting", the total average number density will be biased towards the easy cases and therefore skewed slightly. Lastly, for the cases where bubbles are small, these bubbles will be missed due to the fact that the resolution of the camera and the lens magnification is not powerful enough to resolve very small bubbles. Because of the difficulty to identify small bubbles and bubbles in clusters for the higher and concentrations and Re, smaller volumes were chosen.

Appendix E

Acoustic Intensity Measurement

The readings for were taken with a BK Precision 2553 Oscilloscope. In accordance with the oscilloscope manual, a decibel Vrms ($dBVrms$) was taken. From the pinducer signal, a FFT was taken and by using the cursor measurement, a $\Delta dBVrms$ was taken. A couple of examples are shown in Figures E.1 and E.1. For example, one reading from the 120 W transducer yielded 80 $dBVrms$.

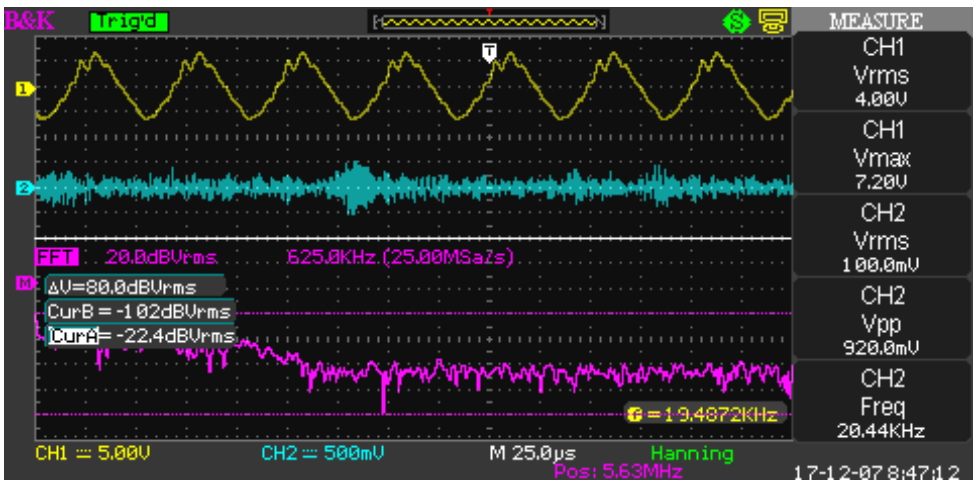

Figure E.1: Example of a dB measurement at 3500 Re, concentration of 17.4 $wt\%$ with the 120 W transducer.

Calculation

The signal voltage is found using the published typical sensitivity of the VP-3 pinducer, $-40\ dB$ to $-50\ dB$. For calculation purposes, $-45\ dB$ was used. In order to get the sensitivity voltage ($V_{sensitivity}$) the reference voltage (V_{ref}) of 1 V/Pa is used. Using equation (E.1), the VP-3 sensitivity voltage value is 5.623 mV/Pa.

$$db_{sensitivity} = 20 \log \left(\frac{V_{sensitivity}}{V_{ref}} \right) \tag{E.1}$$

Next, the signal V_{rms} can be calculated using equation (E.2) with a reference voltage (V_0) of 1 V. A signal of 62 $dBVrms$ yields a voltage of 1258 V

$$dBVrms = 20 \log \left(\frac{V_{sensed}}{V_0} \right) \tag{E.2}$$

The sensed decibel in terms of Pa can be calculated using the sensed voltage and sensitivity voltage and equation (E.3). This yields a db_{sensed} of 35 $dBVrms$

$$dB_{sensed} = 20\ \log \left(\frac{V_{sensed}}{V_{sensitivity}} \right) \tag{E.3}$$

From the literature, 1 Pa is equivalent to 94 dB. The absolute decibel ($dB(SPL)$) can be calculated. Continuing the calculation, the $dB(SPL)$ is 84.

$$-dB_{sensed} + dB_{sensitivity} + dB_{Pa} = dB(SPL) \tag{E.4}$$

Finally, the $dB(SPL)$ can be related to acoustic intensity using equation (E.5).

The reference intensity (I_{ref}) in the literature is $1 \times 10^{-12}\ W/cm^2$. This yields an acoustic intensity of $2.5 \times 10^{-8}\ W/cm^2$.

$$dB(SPL) = 10 \log \left(\frac{I}{I_{ref}} \right) \tag{E.5}$$

References

[1] Pushker A. Kharecha and James E. Hansen. "Prevented Mortality and Greenhouse Gas Emissions from Historical and Projected Nuclear Power". In: *Environmental Science & Technology* 47.9 (May 2013), pp. 4889–4895. ISSN: 0013-936X. DOI: 10.1021/es3051197. URL: http://pubs.acs.org/doi/10.1021/es3051197.

[2] Michaja Pehl et al. "Understanding future emissions from low-carbon power systems by integration of life-cycle assessment and integrated energy modelling". In: *Nature Energy* 2.12 (Dec. 2017), pp. 939–945. ISSN: 2058-7546. DOI: 10.1038/s41560-017-0032-9. URL: http://www.nature.com/articles/s41560-017-0032-9.

[3] *GIF Portal - Home - Public*. URL: https://www.gen-4.org/gif/jcms/c_9260/public (visited on 03/26/2018).

[4] World Nuclear Association. *Generation IV Nuclear Reactors: WNA - World Nuclear Association*. 2017. URL: http://www.world-nuclear.org/information-library/nuclear-fuel-cycle/nuclear-power-reactors/generation-iv-nuclear-reactors.aspx (visited on 02/08/2018).

[5] Murray W. Rosenthal. *An Account of Oak Ridge National Laboratory's Thirteen Nuclear Reactors*. Tech. rep. ORNL/TM-2009/181. Oak Ridge, TN: Oak Ridge National Laboratory, 2009, pp. 1–66.

[6] E. S. Bettis et al. "The Aircraft Reactor Experiment—Design and Construction". In: *Nuclear Science and Engineering* 2.6 (Nov. 1957), pp. 804–825. ISSN: 0029-5639. DOI: 10.13182/NSE57-A35495. URL: https://www.tandfonline.com/doi/full/10.13182/NSE57-A35495.

[7] E. S. Bettis et al. "The Aircraft Reactor Experiment - Operation". In: *Nuclear Science and Engineering* 2.6 (1957), pp. 841–853. ISSN: 0029-5639. DOI: 10.13182/NSE57-A35497.

[8] Thomas J. Dolan. *Molten salt reactors and thorium energy*. Woodhead Publishing is an imprint of Elsevier, 2017. ISBN: 9780081011263.

[9] *GIF Portal - Molten Salt Reactor (MSR)*. URL: https://www.gen-4.org/gif/jcms/c_42150/molten-salt-reactor-msr (visited on 02/08/2018).

[10] Jérôme Serp et al. "The molten salt reactor (MSR) in generation IV: Overview and perspectives". In: *Progress in Nuclear Energy* 77 (Nov. 2014), pp. 308–319. ISSN: 01491970. DOI: 10.1016/j.pnucene.2014.02.014. URL: http://linkinghub.elsevier.com/retrieve/pii/S0149197014000456.

[11] Venugopal Koikal Varma et al. *AHTR Mechanical, Structural, And Neutronic Preconceptual Design, Oak Ridge National Laboratory Report ORNL/TM-2012/320*. Tech. rep. September. Oak Ridge, TN (United States): Oak Ridge National Laboratory (ORNL), Oct. 2012. DOI: 10.2172/1081980. URL: http://www.osti.gov/servlets/purl/1081980/.

[12] *Fluoride-Salt-Cooled High Temperature Reactor (FHR) Materials, Fuels and Components White Paper*. Tech. rep. July. Madison, Wisconsin: Department of Nuclear Engineering and Engineering Physics, University of Wisconsin, Madison, 2013, p. 163. URL: http://fhr.nuc.berkeley.edu/wp-content/uploads/2013/08/12-003-FHR-Workshop-3-Report-Final.pdf.

[13] Charalampos Andreades et al. *Mark-1 PB-FHR Technical Description Technical Description of the "Mark 1" Pebble-Bed Fluoride-Salt-Cooled High-Temperature Reactor (PB-FHR) Power Plant*. Tech. rep. Berkeley: University of California, Berkeley, 2014, pp. 1–153. URL: http://fhr.nuc.berkeley.edu/wp-content/uploads/2014/10/14-002-PB-FHR_Design_Report_Final.pdf.

[14] Enrico Zio, Francesco Di Maio, and Jiejuan Tong. "Safety margins confidence estimation for a passive residual heat removal system". In: *Reliability Engineering & System Safety* 95.8 (Aug. 2010), pp. 828–836. ISSN: 09518320. DOI: 10.1016/j.ress.2010.03.006. URL: http://linkinghub.elsevier.com/retrieve/pii/S0951832010000724.

[15] Per Peterson et al. *Integral and Separate Effects Tests for Thermal Hydraulics Code Validation for Liquid-Salt Cooled Reactors Final Report*. Tech. rep. Project Number: 09-789. Berkeley: University of California, Berkeley, 2012, pp. 1–69. URL: https://neup.inl.gov/SiteAssets/Final%20Reports/09-789%20NEUP%20Final%20Report.pdf.

[16] Raluca O. Scarlat and Per F. Peterson. "The current status of fluoride salt cooled high temperature reactor (FHR) technology and its overlap with HIF target chamber concepts". In: *Nuclear Instruments and Methods in Physics Research Section A: Accelerators, Spectrometers, Detectors and Associated Equipment* 733 (Jan. 2014), pp. 57–64. ISSN: 01689002. DOI: 10.1016/j.nima.2013.05.094. URL: http://linkinghub.elsevier.com/retrieve/pii/S0168900213007055.

[17] D. F. Williams, L. M. Toth, and K. T. Clarno. *Assessment of Candidate Molten Salt Coolants for the Advanced High-Temperature Reactor (AHTR)*. Tech. rep. ORNL/TM-2006/12. Oak Ridge, TN: Oak Ridge National Laboratory, 2006, pp. 1–69. URL: http://www.ntis.gov/support/ordernowabout.htm.

[18] *NRC: Frequently Asked Questions About Liquid Radioactive Releases*. URL: https://www.nrc.gov/reactors/operating/ops-experience/tritium/faqs.html (visited on 12/31/2015).

[19] Charles W. Forsberg et al. *Integrated FHR Technology Development : Tritium Management , Materials Testing , Salt Chemistry Control , Thermal-Hydraulics and Neutronics with Associated Benchmarking*. Tech. rep. NEUP14-7476. 2014.

[20] T. S. Kress. "Mass transfer between small bubbles and liquids in concurrent turbulent pipeline flow". Doctor of Philosophy. University of Tennessee, 1972, p. 170. URL: http://moltensalt.org/references/static/downloads/pdf/ORNL-TM-3718.pdf.

[21] Dale Ensminger and Leonard Bond. *Ultrasonics*. 3rd. Dekker Mechanical Engineering. New York: CRC Press, Sept. 2011, p. 723. ISBN: 978-0-8247-5889-9.

[22] Manickam Sivakumar, Siah Ying Tang, and Khang Wei Tan. "Cavitation technology - a greener processing technique for the generation of pharmaceutical nanoemulsions." In: *Ultrason. Sonochem.* 21.6 (2014), pp. 2069–2083. ISSN: 1873-2828. DOI: 10.1016/j.ultsonch.2014.03.025. URL: http://www.sciencedirect.com/science/article/pii/S1350417714001151.

[23] Tina Harifi and Majid Montazer. "A review on textile sonoprocessing: A special focus on sonosynthesis of nanomaterials on textile substrates". In: *Ultrasonics Sonochemistry* 23 (2015), pp. 1–10. ISSN: 13504177. DOI: 10.1016/j.ultsonch.2014.08.022. URL: http://linkinghub.elsevier.com/retrieve/pii/S1350417714002922.

[24] Farid Chemat, Zill-e-Huma, and Muhammed Kamran Khan. "Applications of ultrasound in food technology: Processing, preservation and extraction". In: *Ultrasonics sonochemistry* 18.4 (July 2011), pp. 813–35. ISSN: 13504177. DOI:

10.1016/j.ultsonch.2010.11.023. URL: http://www.ncbi.nlm.nih.gov/pubmed/21216174.

[25] Floren V. Rubio, Edward D. Blandford, and Leonard J. Bond. "Summary of Sonoprocessing Applications for Nuclear Technologies and Potential Future Applications". In: *2014 ANS Winter Meet. Nucl. Technol. Expo.* Vol. 111. Anaheim, CA, 2014, pp. 1068–1071.

[26] Floren Rubio, Edward D. Blandford, and Leonard J. Bond. "Survey of advanced nuclear technologies for potential applications of sonoprocessing". In: *Ultrasonics* 71 (Sept. 2016), pp. 211–222. ISSN: 0041624X. DOI: 10.1016/j.ultras.2016.06.017. URL: http://linkinghub.elsevier.com/retrieve/pii/S0041624X16301019.

[27] Walter G. Whitman. "The two film theory of gas absorption". In: *International Journal of Heat and Mass Transfer* 5.5 (May 1962), pp. 429–433. ISSN: 00179310. DOI: 10.1016/0017-9310(62)90032-7. URL: http://linkinghub.elsevier.com/retrieve/pii/0017931062900327.

[28] Ralph Higbie. "The rate of absorption of a pure gas into still liquid during short periods of exposure". In: *AIChE 31.* New York, 1935, pp. 365–389.

[29] P. V. Danckwerts. "Significance of Liquid-Film Coefficients in Gas Absorption". In: *Industrial & Engineering Chemistry* 43.6 (June 1951), pp. 1460–1467. ISSN: 0019-7866. DOI: 10.1021/ie50498a055. URL: http://pubs.acs.org/doi/abs/10.1021/ie50498a055.

[30] Thomas K. Sherwood, Robert L. Pigford, and Charles R. Wilke. *Mass transfer.* McGraw-Hill, 1975, p. 677. ISBN: 0070566925.

[31] Felix Garcia-Ochoa and Emilio Gomez. "Prediction of gas-liquid mass transfer coefficient in sparged stirred tank bioreactors". In: *Biotechnology and Bioengineering* 92.6 (Dec. 2005), pp. 761–772. ISSN: 0006-3592. DOI: 10.1002/bit.20638. URL: http://doi.wiley.com/10.1002/bit.20638.

[32] Felix Garcia-Ochoa and Emilio Gomez. "Bioreactor scale-up and oxygen transfer rate in microbial processes: An overview". In: *Biotechnology Advances* 27.2 (Mar. 2009), pp. 153–176. ISSN: 07349750. DOI: 10.1016/j.biotechadv.2008.10.006. URL: http://linkinghub.elsevier.com/retrieve/pii/S0734975008001079.

[33] John C. Lamont and D. S. Scott. "An eddy cell model of mass transfer into the surface of a turbulent liquid". In: *AIChE Journal* 16.4 (July 1970), pp. 513–519. ISSN: 0001-1541. DOI: 10.1002/aic.690160403. URL: http://doi.wiley.com/10.1002/aic.690160403.

[34] Kiyomi Akita and Fumitake Yoshida. "Bubble Size, Interfacial Area, and Liquid-Phase Mass Transfer Coefficient in Bubble Columns". In: *Industrial & Engineering Chemistry Process Design and Development* 13.1 (Jan. 1974), pp. 84–91. ISSN: 0196-4305. DOI: 10.1021/i260049a016. URL: http://pubs.acs.org/doi/abs/10.1021/i260049a016.

[35] Wolf-Dieter Deckwer and Robert W. Field. *Bubble column reactors*. Wiley, 1992, p. 533. ISBN: 9780471918110.

[36] Pisut Painmanakul et al. "Theoretical Prediction of Volumetric Mass Transfer Coefficient (kla) for Designing an Aeration Tank". In: *Engineering Journal* 13.3 (Nov. 2009), pp. 13–28. ISSN: 01258281. DOI: 10.4186/ej.2009.13.3.13. URL: http://www.engj.org/index.php/ej/article/view/64/31.

[37] J. Dudley. "Mass transfer in bubble columns: A comparison of correlations". In: *Water Research* 29.4 (Apr. 1995), pp. 1129–1138. ISSN: 00431354. DOI: 10.1016/0043-1354(94)00253-4. URL: http://www.sciencedirect.com/science/article/pii/0043135494002534.

[38] Gracey and Associates. *Acoustic Glossary, Sound and Vibration Definitions, Terms, Units, Measurements*. URL: http://www.acoustic-glossary.co.uk/ (visited on 01/18/2018).

[39] N. Cheeke and J. David. *Fundamentals and applications of ultrasonic waves*. CRC series in pure and applied physics. Boca Raton : CRC Press, c2002., 2012, p. 462. ISBN: 0849301300.

[40] Timothy G. Leighton. *The Acoustic Bubble*. London: Academica Press, 1994, p. 613. ISBN: 0-12-441920-8.

[41] Gordon S. Kino. *Acoustic waves : devices, imaging, and analog signal processing*. Englewood Cliffs, New Jersey: Prentice-Hall, 1987, p. 601. ISBN: 0130030473.

[42] S. N. Domenico. "Acoustic wave propagation in air-bubble curtains in water-Part I: History and theory". In: *GEOPHYSICS* 47.3 (Mar. 1982), pp. 345–353. ISSN: 0016-8033. DOI: 10.1190/1.1441340. URL: http://library.seg.org/doi/10.1190/1.1441340.

[43] B. Würsig, C. R. Greene, and T. A. Jefferson. "Development of an air bubble curtain to reduce underwater noise of percussive piling". In: *Marine Environmental Research* 49.1 (Feb. 2000), pp. 79–93. ISSN: 01411136. DOI: 10.1016/S0141-1136(99)00050-1. URL: http://linkinghub.elsevier.com/retrieve/pii/S0141113699000501.

[44] Helen Bailey et al. "Assessing underwater noise levels during pile-driving at an offshore windfarm and its potential effects on marine mammals". In: *Marine Pollution Bulletin* 60.6 (June 2010), pp. 888–897. ISSN: 0025326X. DOI: 10.1016/j.marpolbul.2010.01.003. URL: http://linkinghub.elsevier.com/retrieve/pii/S0025326X10000044.

[45] A Tsouvalas and A.V. Metrikine. "Noise reduction by the application of an air-bubble curtain in offshore pile driving". In: *Journal of Sound and Vibration* 371 (June 2016), pp. 150–170. ISSN: 0022460X. DOI: 10.1016/j.jsv.2016.02.025. URL: http://linkinghub.elsevier.com/retrieve/pii/S0022460X16001681.

[46] James A Reyff. "Reducing Underwater Sounds with Air Bubble Curtains Protecting Fish and Marine Mammals from Pile-Driving Noise". In: *TR News* 262 (2009). URL: http://onlinepubs.trb.org/onlinepubs/trnews/trnews262rpo.pdf.

[47] Michael A. Ainslie and Timothy G. Leighton. "Review of scattering and extinction cross-sections, damping factors, and resonance frequencies of a spherical gas bubble". In: *The Journal of the Acoustical Society of America* 130.5 (Nov. 2011), pp. 3184–3208. ISSN: 0001-4966. DOI: 10.1121/1.3628321. URL: http://asa.scitation.org/doi/10.1121/1.3628321.

[48] Gerald Harvey, Anthony Gachagan, and Tapiwa Mutasa. "Review of high-power ultrasound-industrial applications and measurement methods." In: *IEEE transactions on ultrasonics, ferroelectrics, and frequency control* 61.3 (Mar. 2014), pp. 481–95. ISSN: 1525-8955. DOI: 10.1109/TUFFC.2014.2932. URL: http://www.ncbi.nlm.nih.gov/pubmed/24569252.

[49] L. H. Thompson and L. K. Doraiswamy. "Sonochemistry: Science and Engineering". In: *Industrial & Engineering Chemistry Research* 38.4 (Apr. 1999), pp. 1215–1249. ISSN: 0888-5885. DOI: 10.1021/ie9804172. URL: http://pubs.acs.org/doi/abs/10.1021/ie9804172.

[50] R. E. Apfel. "Acoustic cavitation prediction". In: *The Journal of the Acoustical Society of America* 69.6 (June 1981), pp. 1624–1633. ISSN: 00014966. DOI: 10.1121/1.385939. URL: http://scitation.aip.org/content/asa/journal/jasa/69/6/10.1121/1.385939.

[51] Robert T. Beyer. *Nonlinear Acoustics*. Woodbury, NY: Acoustical Society of America, 1997, pp. 207–231. ISBN: 9780123218605.

[52] T. J. Mason and J. P. Lorimer. *Sonochemistry: Theory, Applications and Uses of Ultrasound in Chemistry*. Ellis Horwood series in physical chemistral. New York: John Wiley & Sons, 1988, p. 252. ISBN: 9780470213735.

[53] Robert J. Urick. *Principles Of Underwater Sound*. McGraw-Hill Ryerson, Limited, 1983, p. 423. ISBN: 0070660875.

[54] Peter R. Birkin, Timothy G. Leighton, and Yvonne E. Watson. "The use of acoustoelectrochemistry to investigate rectified diffusion." In: *Ultrasonics sonochemistry* 11.3-4 (May 2004), pp. 217–21. ISSN: 1350-4177. DOI: 10.1016/j.ultsonch.2004.01.023. URL: http://www.sciencedirect.com/science/article/pii/S1350417704000276.

[55] Kenneth Sanders Suslick. *Ultrasound : its chemical, physical, and biological effects / edited by Kenneth S. Suslick*. New York, N.Y. : VCH Publishers, c1988., 1988. ISBN: 0895733285.

[56] Markus Stokmaier. *RP Bubble*. 2018. URL: https://github.com/stromatolith/RP_Bubble (visited on 03/04/2018).

[57] S. J. Kline. *Similitude and approximation theory*. New York: McGraw-Hill, 1965, xiii, 229 pages.

[58] Philippe M. Bardet and Per F. Peterson. "Options for Scaled Experiments for High Temperature Liquid Salt and Helium Fluid Mechanics and Convective Heat Transfer". In: *Nuclear Technology* 163.3 (Sept. 2008), pp. 344–357. ISSN: 0029-5450. DOI: 10.13182/NT163-344. URL: https://www.tandfonline.com/doi/full/10.13182/NT163-344.

[59] Floren Rubio, Leonard Bond, and Edward Blandford. "Scaled experiment investigating sonomechanically enhanced inert gas sparging mass transfer". In: *Nuclear Engineering and Design* 324 (Dec. 2017), pp. 171–180. ISSN: 00295493. DOI: 10.1016/j.nucengdes.2017.08.016. URL: http://www.sciencedirect.com/science/article/pii/S0029549317303904.

[60] Bruce Roy Munson. *Fundamentals of fluid mechanics*. Wiley, 2009. ISBN: 9780470926536.

[61] M. Minnaert. "XVI. On musical air-bubbles and the sounds of running water". In: *The London, Edinburgh, and Dublin Philosophical Magazine and Journal of Science* 16.104 (Aug. 1933), pp. 235–248. ISSN: 1941-5982. DOI: 10.1080/14786443309462277. URL: http://www.tandfonline.com/doi/abs/10.1080/14786443309462277.

[62] Kenneth S. Suslick and Gareth J. Price. "Applications of Ultrasound to Materials Chemistry". en. In: *Annual Review of Materials Science* 29.1 (Aug. 1999), pp. 295–326. ISSN: 0084-6600. DOI: 10.1146/annurev.matsci.29.1.295. URL: http://www.annualreviews.org/doi/10.1146/annurev.matsci.29.1.295.

[63] *TRACE V5.0 THEORY MANUAL Field Equations, Solution Methods, and Physical Models*. Tech. rep. United States Nuclear Regulatory Commission. URL: https://www.nrc.gov/docs/ML0710/ML071000097.pdf.

[64] T. K. Jagannathan, R. Nagarajan, and K. Ramamurthi. "Effect of ultrasound on bubble breakup within the mixing chamber of an effervescent atomizer". In: *Chemical Engineering and Processing: Process Intensification* 50.3 (Mar. 2011), pp. 305–315. ISSN: 02552701. DOI: 10.1016/j.cep.2011.01.006. URL: http://www.sciencedirect.com/science/article/pii/S0255270111000213.

[65] Johannes Schindelin et al. "The ImageJ ecosystem: An open platform for biomedical image analysis". In: *Molecular Reproduction and Development* 82.7-8 (July 2015), pp. 518–529. ISSN: 1040452X. DOI: 10.1002/mrd.22489. URL: http://www.ncbi.nlm.nih.gov/pubmed/26153368.

[66] Robert H. Perry and Don W. Green. *Perry's chemical engineers' handbook*. McGraw-Hill, 2008. ISBN: 0071422943.

[67] Junlian Yin et al. "Study on the Air Core Formation of a Gas–Liquid Separator". In: *Journal of Fluids Engineering* 137.9 (Apr. 2015), p. 091301. ISSN: 0098-2202. DOI: 10.1115/1.4030198.

[68] Baharak Sajjadi et al. "Investigation of mass transfer intensification under power ultrasound irradiation using 3D computational simulation: A comparative analysis". In: *Ultrasonics Sonochemistry* 34 (2017), pp. 504–518. ISSN: 18732828. DOI: 10.1016/j.ultsonch.2016.06.026. URL: http://dx.doi.org/10.1016/j.ultsonch.2016.06.026.

[69] Baharak Sajjadi, Abdul Aziz Abdul Raman, and Shaliza Ibrahim. "Influence of ultrasound power on acoustic streaming and micro-bubbles formations in a low frequency sono-reactor: Mathematical and 3D computational simulation". In: *Ultrasonics Sonochemistry* 24 (2015), pp. 193–203. ISSN: 18732828. DOI: 10.1016/j.ultsonch.2014.11.013. URL: http://dx.doi.org/10.1016/j.ultsonch.2014.11.013.

[70] Baharak Sajjadi, Abdul Aziz Abdul Raman, and Shaliza Ibrahim. "A comparative fluid flow characterisation in a low frequency/high power sonoreactor and mechanical stirred vessel". In: *Ultrasonics Sonochemistry* 27 (Nov. 2015), pp. 359–373. ISSN: 13504177. DOI: 10.1016/j.ultsonch.2015.04.034. URL: http://linkinghub.elsevier.com/retrieve/pii/S1350417715001273.

[71] R Kažys, Algirdas Voleišis, and B Voleišienė. "High temperature ultrasonic transducers: review". In: *Ultragarsas (Ultrasound)* 63.2 (2008), pp. 7–17. URL: http://www.ultragarsas.ktu.lt/index.php/USnd/article/view/17063.

[72] J. W. Griffin et al. "High temperature ultrasonic transducers for in-service inspection of liquid metal fast reactors". In: *2011 IEEE International Ultrasonics Symposium*. IEEE, Oct. 2011, pp. 1924–1927. ISBN: 978-1-4577-1252-4. DOI: 10.1109/ULTSYM.2011.0479. URL: http://ieeexplore.ieee.org/document/6293627/.

[73] J. L. Rempe et al. "Advanced In-Pile Instrumentation for Materials Testing Reactors". In: *IEEE Trans. Nucl. Sci.* 61.4 (Aug. 2014), pp. 1984–1994. ISSN:

0018-9499. DOI: 10.1109/TNS.2014.2335616. URL: http://ieeexplore.ieee.org/lpdocs/epic03/wrapper.htm?arnumber=6869028.

[74] Prathamesh N. Bilgunde and Leonard J. Bond. "Effect of Thermal Degradation on High Temperature Ultrasonic Transducer Performance in Small Modular Reactors". In: *Physics Procedia* 70 (2015), pp. 433–436. ISSN: 18753892. DOI: 10.1016/j.phpro.2015.08.137. URL: http://www.sciencedirect.com/science/article/pii/S1875389215008780.

[75] A.N. Sinclair and A.M. Chertov. "Radiation endurance of piezoelectric ultrasonic transducers – A review". In: *Ultrasonics* 57.July (Mar. 2015), pp. 1–10. ISSN: 0041624X. DOI: 10.1016/j.ultras.2014.10.024. URL: http://www.sciencedirect.com/science/article/pii/S0041624X14003096.

[76] Nian-Sheng Cheng. "Formula for the Viscosity of a Glycerol-Water Mixture". In: *Industrial & Engineering Chemistry Research* 47.9 (May 2008), pp. 3285–3288. ISSN: 0888-5885. DOI: 10.1021/ie071349z. URL: http://pubs.acs.org/doi/abs/10.1021/ie071349z.